BRUGGE '25

BELNUC

SYMPOSIUM

ABSTRACT BOOK

TABLE OF CONTENTS

Oral Presentations

MEDICAL TRACK

68GA]FAPI-46 PET/CT FOR PREOPERATIVE ASSESSMENT OF PERITONEAL CARCINOMATOSIS-INTERIM ANALYSIS OF PROSPECTIVE FAPECA TRIAL

Ayça Arçay Öztürk,[1], Gabriel Liberale,[2], Laura Polastro,[3], Ana Veron Sanchez,[4], Anne-Leen Deleu,[1], Paulus Kristanto,[5], Zena Wimana,[1], Sigrid Vercauteren,[1], Loubna Taraji Schiltz,[1], Patrick Flamen,[1]

[1] Institut Jules Bordet, Hôpital Universitaire de Bruxelles (H.U.B), Université Libre de Bruxelles (Ulb); Department of Nuclear Medicine, [2] Institut Jules Bordet, Hôpital Universitaire de Bruxelles (H.U.B), Université Libre de Bruxelles (Ulb); Department of Surgery, [3] Institut Jules Bordet, Hôpital Universitaire de Bruxelles (H.U.B), Université Libre de Bruxelles (Ulb); Department of Medical Oncology, [4] Institut Jules Bordet, Hôpital Universitaire de Bruxelles (H.U.B), Université Libre de Bruxelles (Ulb); Department of Radiology, [5] Institut Jules Bordet, Hôpital Universitaire de Bruxelles (H.U.B), Université Libre de Bruxelles (Ulb); Data Center

Aims

Peritoneal metastases (PM) from gastrointestinal and ovarian cancers pose significant challenges in accurate preoperative staging. Current standard imaging modalities like CT, MRI and FDG PET/CT often underestimate PM extent, leading to unexpected non-resectable disease during surgery (1). FAPI (fibroblast activation protein inhibitor), a novel PET tracer targeting the fibroblast activation protein, has demonstrated significant potential as pan-cancer tracer due to its high tumour specificity and low background activity (2). Preliminary data suggest that [^{68}Ga]FAPI PET/CT may offer superior sensitivity for PM detection (3). This study aims to evaluate the potential of [^{68}Ga]FAPI-46 PET/CT as a preoperative imaging tool for peritoneal carcinomatosis by correlating [^{68}Ga]FAPI-46 PET findings with surgical outcomes and comparing its diagnostic performance with MRI, [^{18}F]FDG PET/CT in colorectal and ovarian cancer patients.

Methods

In this prospective study (NCT06061874), eligible patients with confirmed or suspected PM undergo [^{68}Ga]FAPI-46 PET/CT, [^{18}F]FDG PET/CT, and abdominopelvic diffusion-weighted MRI within four weeks prior to scheduled cytoreductive surgery (CRS) and/or diagnostic laparoscopy (DL). Patients indicated for neoadjuvant chemotherapy (NAC) undergo scans before and after NAC. The study targets the enrollment of eighty patients.

The extent of PM was determined using the peritoneal cancer index (PCI) scoring system, which segments the abdomen into distinct regions and assigns scores according to the tumor size in each region (4). Intraclass correlation coefficient (ICC) was used to assess the concordance between PCI scores determined based on [^{68}Ga]FAPI-46 PET/CT (FAPI-PCI), [^{18}F]FDG PET/CT (FDG-PCI), MRI (MRI-PCI) and the PCI found during surgery (S-PCI).

Quantitative parameters (maximum standardized uptake value (SUVmax), target-to-background ratio (TBR) and total peritoneal tumour volumes (PTV)) of peritoneal metastases detected on [^{68}Ga]FAPI-46 PET/CT and [^{18}F]FDG PET/CT scans were compared using the Wilcoxon signed-rank test.

Results

Fourty-one patients (9 male, 32 female, mean age of 61.7) were analyzed, including 30 ovarian and 11 colorectal cancer patients. The mean interval between scans and surgery was 10.8 days for [^{68}Ga]FAPI-46 PET/CT, 13.8 days for MRI and 15.4 days for [^{18}F]FDG PET/CT.

The mean PCI score at surgery (n=48; 38 based on CRS, 10 based on DL) was 15.6±9.4. The mean FAPI-PCI score (n=48, 13.4±9) was significantly higher than the mean MRI-PCI (n=45, 9±7.3, p<0.001) and FDG-PCI (n=46, 7.2±8.8, p<0.001). FAPI-PCI correlated very well with surgical PCI (ICC 0.83, 95%

CI: 0.68-0.91). The ICC between S-PCI and FAPI-PCI was substantially higher than that between S-PCI and MRI-PCI (ICC 0.49, 95% CI: 0.02-0.75) and S-PCI and FDG-PCI (ICC 0.41, 95% CI: -0.03-0.69) (Figure 1).
The quantitative parameters SUVmax, TBR and PTV of [^{68}Ga]FAPI-46 PET/CT for the PM lesions were significantly higher than those of [^{18}F]FDG PET/CT (mean SUVmax: 11.5±6.7 vs. 7.4±8,$p<0.001$; mean TBR: 9±5.7 vs. 3.7±4.1,$p<0.001$; mean PTV: 129.1±271.4 ml vs. 80.5±248.3 ml, $p<0.001$).
A case-by-case review of nine patients who received NAC demonstrated that [^{68}Ga]FAPI-46 PET/CT effectively monitored chemotherapy response by showing decreased tracer uptake in all patients. More importantly, [^{68}Ga]FAPI-46 PET/CT provided a more accurate post-NAC disease assessment than [^{18}F]FDG PET/CT and MRI when correlated with surgical findings (Figure 2).

Conclusions
Based on interim analysis, [^{68}Ga]FAPI-46 PET-based PCI score evaluation demonstrated a strong correlation with PCI scores assessed during surgery in colorectal and ovarian cancer patients. [^{68}Ga]FAPI-46 PET outperforms the current standard imaging modalities, MRI and [^{18}F]FDG PET, making it a significant advancement for preoperative peritoneal disease assessment.

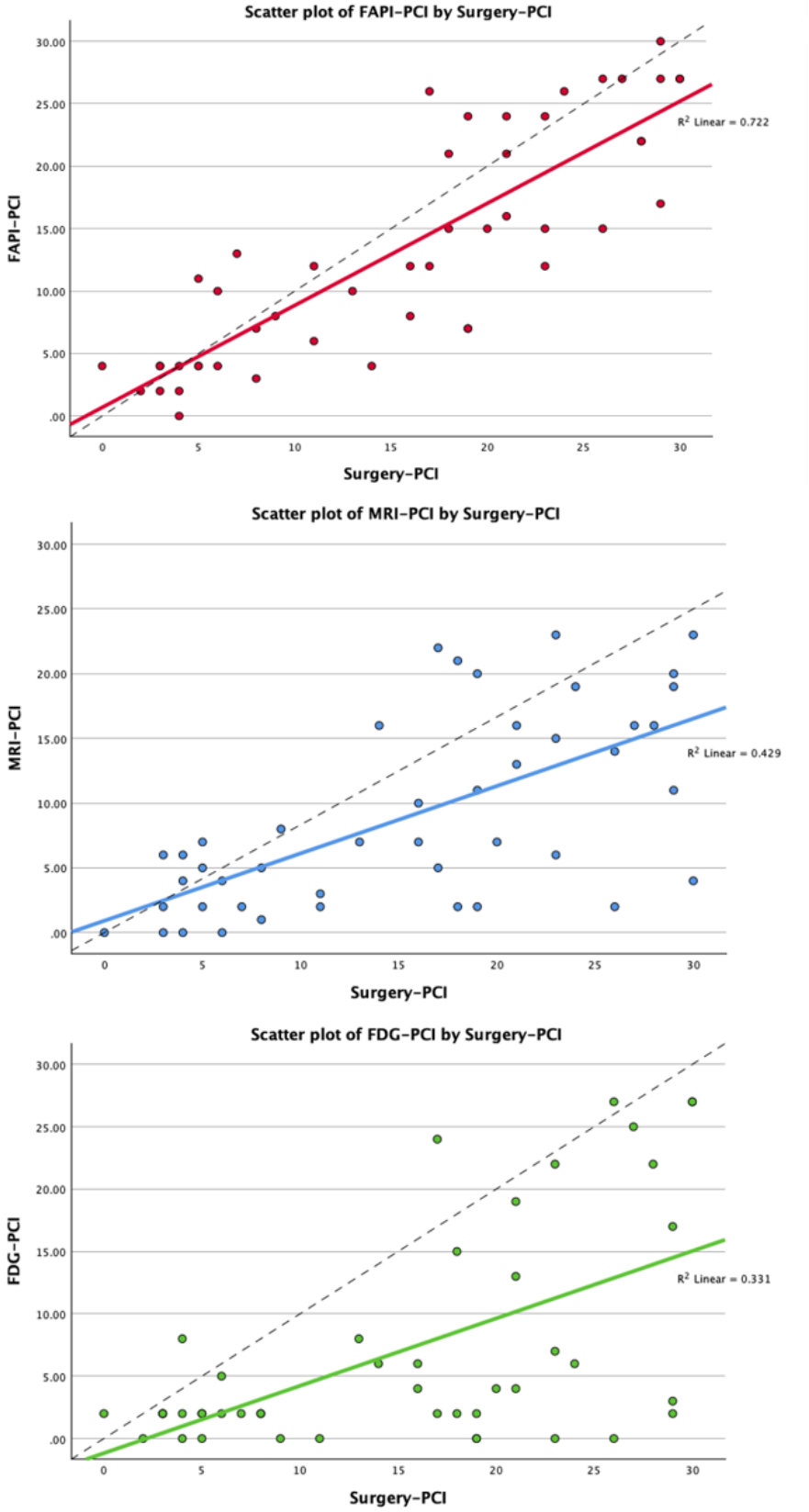

Figure 1. **Scatter plots illustrating the correlation between Surgery-PCI and different imaging-derived PCI scores.**

The top panel represents the correlation between Surgery-PCI and FAPI-PCI, the middle panel shows the correlation between Surgery-PCI and MRI-PCI, and the bottom panel depicts the correlation between Surgery-PCI and FDG-PCI. Each plot includes a fitted regression line (solid line) and a reference line (dashed line) for comparison.

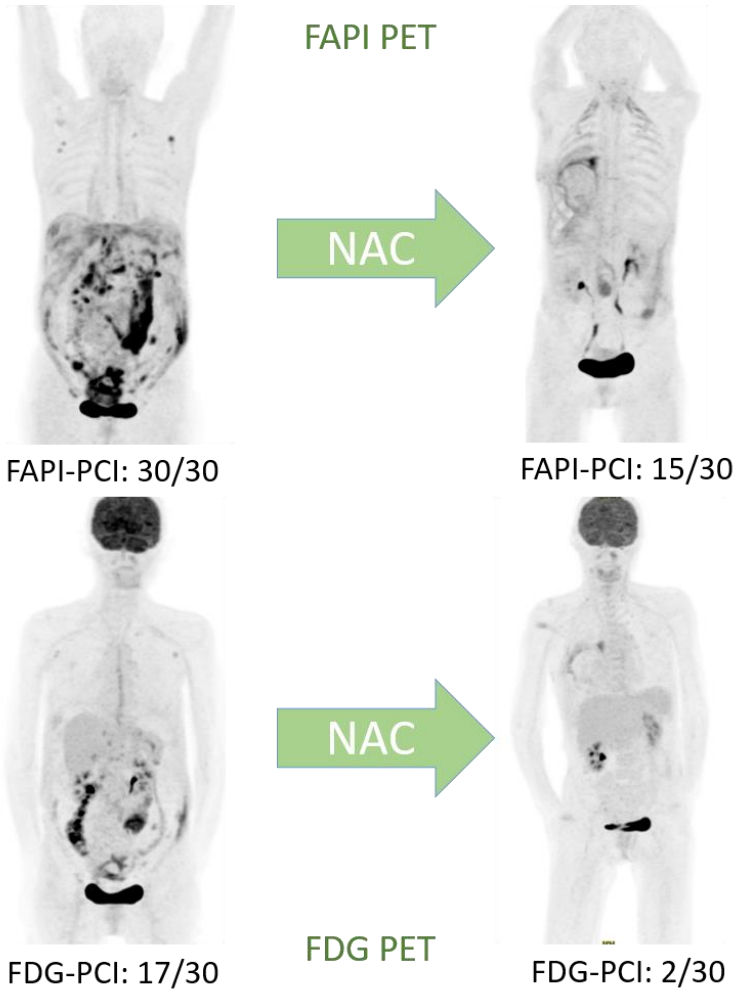

Figure 2. **Impact of NAC on [^{68}Ga]FAPI-46 PET vs. [^{18}F]FDG PET in ovarian cancer.**

Maximum intensity projection (MIP) images of [^{68}Ga]FAPI-46 PET/CT and [^{18}F]FDG PET/CT in a 67-year-old ovarian cancer patient who received four cycles of neoadjuvant chemotherapy (NAC). *Top row:* MIP images of [^{68}Ga]FAPI-46 PET/CT before and after NAC. *Bottom row:* MIP images of [^{18}F]FDG PET/CT before and after NAC. The peritoneal cancer index (PCI) score at baseline was 30/30 on FAPI PET, 17/30 on FDG PET, and 20/30 on MRI. Diagnostic laparoscopy, performed before NAC and within four weeks of the scans, determined a PCI of 29/30, highlighting the superior accuracy of FAPI PET in assessing disease extent compared to FDG PET and MRI. After NAC, PCI scores were 15/30 on FAPI PET, 2/30 on FDG PET, and 2/30 on MRI, reflecting treatment response. The patient subsequently underwent cytoreductive surgery, where the intraoperative PCI score was determined to be 19/30. FAPI PET continued to demonstrate post-NAC disease extent more accurately than FDG PET and MRI.

References:

1) Power JW, Dempsey PJ, Yates A, Fenlon H, Mulsow J, Shields C, Cronin CG. Peritoneal malignancy: anatomy, pathophysiology and an update on modern day imaging. Br J Radiol. 2022 Apr 1;95(1132):20210217.
2) Kratochwil C, Flechsig P, Lindner T, Abderrahim L, Altmann A, Mier W, et al. (68)Ga-FAPI PET/CT: Tracer Uptake in 28 Different Kinds of Cancer. J Nucl Med. 2019;60(6):801-5.
3) Gege Z, Xueju W, Bin J. Head-To-Head Comparison of 68Ga-FAPI PET/CT and FDG PET/CT for the Detection of Peritoneal Metastases: Systematic Review and Meta-Analysis. AJR Am J Roentgenol. 2023 Apr;220(4):490-498. doi: 10.2214/AJR.22.28402.
4) Harmon RL, Sugarbaker PH. Prognostic indicators in peritoneal carcinomatosis from gastrointestinal cancer. Int Semin Surg Oncol. 2005 Feb 8;2(1):3.

177LU-PSMA SPECT/CT EARLY RESPONSE ASSESSMENT WITH RECIP 1.0

Mutaz Kassas,[1], Louise Devriendt,[2], Thomas Guiot,[3], Clementine Marin,[3], Rachele Danieli,[3], Loubna Taraji,[1], Ioannis Karfis,[1], Erwin Woff,[1], Patrick Flamen,[1], Carlos Artigas,[1]

[1] Institut Jules Bordet, Hopital Universitaire de Bruxelles, Université Libre de Bruxelles; Nuclear Medicine Department, [2] Faculté de Médecine, Université Libre de Bruxelles, [3] Institut Jules Bordet, Hopital Universitaire de Bruxelles, Université Libre de Bruxelles; Medical Physics Department

Aims: Lutetium-177 prostate-specific membrane antigen radioligand therapy (^{177}Lu-PSMA RLT) has revolutionized the treatment of metastatic castration resistant prostate cancer (mCRPC). While post-therapy SPECT/CT scans are routinely performed to confirm ^{177}Lu-PSMA targeting, their potential for treatment response assessment remains largely underutilized. The Response Evaluation Criteria in PSMA PET/CT (RECIP 1.0) is a widely studied response assessment framework for PSMA PET/CT in mCRPC patients receiving ^{177}Lu-PSMA RLT. However, its application on post-therapy SPECT/CT has not been explored. This study evaluates the prognostic value of early response assessment using RECIP 1.0 criteria on 24hr post-therapy SPECT/CT images at the first 2 cycles of ^{177}Lu-PSMA RLT.

Methods: From a database of all mCRPC patients treated with ^{177}Lu-PSMA-I&T at our institution, patients having evaluable 24hr SPECT/CT images at cycle 1 (C1) and cycle 2 (C2) were included. Automated lesion segmentation was performed using Lesion ID Pro (MIM software) for both time-points. Relative changes in total tumor burden (TTB) and detection of new lesions between C1 and C2 post-therapy SPECT/CT scans were used to classify patients into two categories according to RECIP1.0 criteria: a) RECIP progressive disease (RECIP PD), with an increase in TTB by ≥20% and the appearance of new lesions; and b) RECIP non-progressive disease (RECIP non-PD), which encompassed partial responders (PR), complete responders (CR) and stable disease (SD). PSA values were measured before treatment initiation, at day of treatment, and between cycles. Progression free survival (PFS) was defined as the time since treatment initiation until PSA progression using the Prostate Cancer Working Group 3 criteria or death from any cause. Overall survival (OS) was defined as the time from treatment initiation until death from any cause. The association between RECIP 1.0 classification and patient outcomes (PFS and OS) was evaluated using univariate and multivariate Cox regression, and by Kaplan-Meier curves with log-rank testing.

Results: Among 205 mCRPC patients treated with ^{177}Lu-PSMA-I&T, 136 patients fulfilled the inclusion criteria. Response assessment using RECIP 1.0 criteria on 24hr post-therapy SPECT/CT imaging at C2 categorized 16/136 (12%) patients as RECIP PD, while the remaining 120/136 (88%) patients were classified as RECIP non-PD (1 CR, 54 PR, and 65 SD). After a median follow-up of 23 months (IQR 15.8-30.1), 123 of 136 patients (90%) experienced disease progression, and 90 (66%) passed away.

Median PFS was 6.4 months (95%CI 5.7-7.2), with significantly shorter PFS in RECIP PD compared to RECIP non-PD patients (median PFS 3.6 vs 7.0 months respectively; HR=2.9 [95%CI 1.6-5.3], p=0.001). Among RECIP non-PD patients, there was no significant difference in PFS between RECIP Responders (CR + PR) vs RECIP SD patients (median PFS 10.2 vs 6.2 months respectively, p=0.9).

Median OS was 16.6 months (95%CI 12.7-20.5), with significantly shorter OS in RECIP PD compared to RECIP non-PD patients (median OS 7.4 vs 17.5 months respectively; HR=3.8 [95%CI 2.0-7.1], p<0.001).

Among RECIP non-PD patients, there was no significant difference in OS between RECIP Responders (CR + PR) vs RECIP SD patients (median OS 20.1 vs 16.6 months respectively, p=0.5).

Conclusions: Our study demonstrates that early detection of disease progression using RECIP 1.0 on 24hr post-therapy SPECT/CT scans independently predicts both PFS and OS in patients receiving ^{177}Lu-PSMA RLT. This method uses routinely acquired imaging data, which reduces patient burden during response assessment. Early identification of patients unlikely to benefit from continued ^{177}Lu-PSMA RLT could enable clinicians to redirect therapeutic strategies at an earlier stage. Future studies could explore whether patients who show progressive disease on early post-therapy SPECT/CT may benefit from switching to alternative therapies, such as chemotherapy or alpha-emitting RLT.

Figure 1. Kaplan-Meier Curves Demonstrating Progression Free Survival by RECIP 1.0 criteria on 24hr ^{177}Lu-PSMA SPECT/CT at C2. *RECIP PD vs RECIP non-PD.*

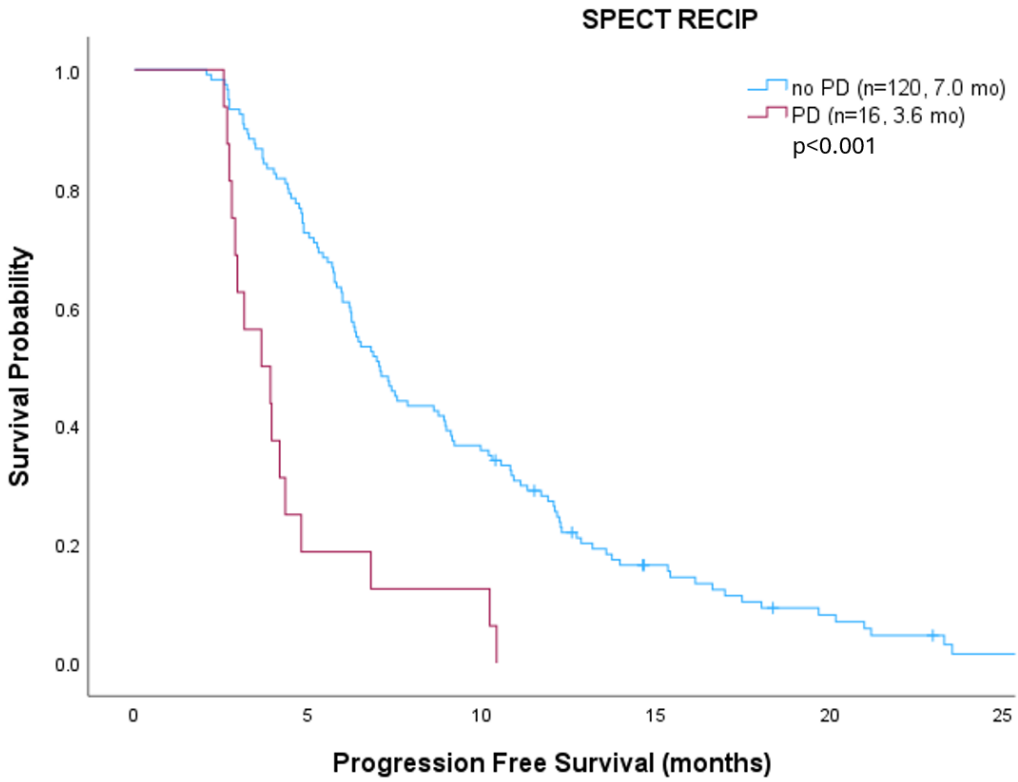

Figure 2. Kaplan-Meier Curves Demonstrating Overall Survival by RECIP 1.0 criteria on 24hr ^{177}Lu-PSMA SPECT/CT at C2. *RECIP PD vs RECIP non-PD.*

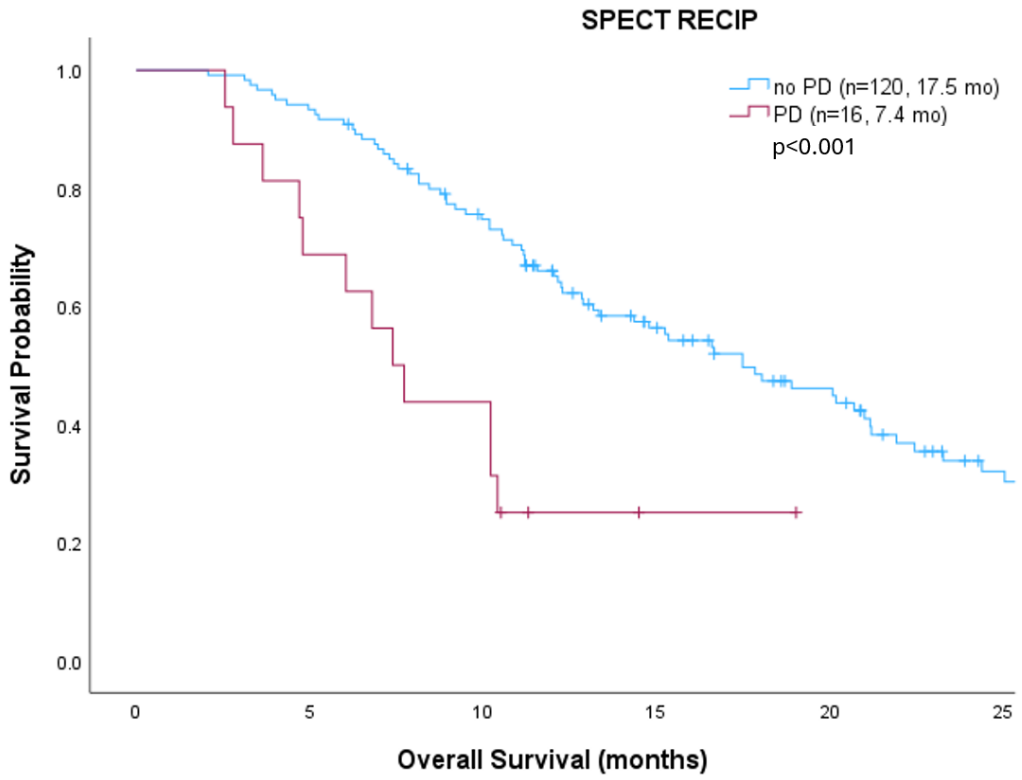
SPECT RECIP
no PD (n=120, 17.5 mo)
PD (n=16, 7.4 mo)
p<0.001
Survival Probability
1.0
0.8
0.6
0.4
0.2
0.0
0
5
10
15
20
25
Overall Survival (months)

FAPI PET/CT RESPONSE ASSESSMENT IN NON-SMALL CELL LUNG CANCER (NSCLC) PATIENTS TREATED WITH (CHEMO)IMMUNOTHERAPY: INTERIM RESULTS OF A PROSPECTIVE EXPLORATORY IMAGING STUDY

Anne-Leen Deleu,[1], Thierry Berghmans,[2], Mariana Brandão,[2], Anouk Goudsmit,[2], Konstantinos Stathopoulos,[3], Ayça Arçay Öztürk,[4], Clémentine Marin,[5], Loubna Taraji,[6], Salma Nisar,[4], Zéna Wimana,[7], Sigrid Vercauteren,[8], Bruno Vanderlinden,[9], Patrick Flamen,[1]

[1] Hub; Institut Jules Bordet; Nuclear Medicine Imaging and Radionuclide Therapy, [2] Hôpital Universitaire de Bruxelles; Institut Jules Bordet; Thoracic Oncology Department, [3] Hôpital Universitaire de Bruxelles; Institut Jules Bordet; Radiology Department, [4] Hôpital Universitaire de Bruxelles; Institut Jules Bordet; Nuclear Medicine, [5] Institut Jules Bordet; Hôpital Universitaire de Bruxelles; Institut Jules Bordet, [6] Institut Jules Bordet; Institut Jules Bordet; Clinical Trial Deparment, [7] Institut Jules Bordet; Institut Jules Bordet; Nuclear Medicine, [8] Be0257981101; Nuclear Medicine; Nuclear Medicine, [9] Hôpital Universitaire de Bruxelles; Institut Jules Bordet; Medical Physics

Aims

Fibroblast activation protein (FAP), selectively expressed on activated fibroblasts in proliferating tissues, is emerging as a promising target in oncology and molecular imaging. The development of small molecule FAP inhibitors (FAPIs), enabling molecular imaging techniques such as FAPI PET/CT, has accelerated research. FAPI has demonstrated significant potential as a pan-cancer tracer due to its high tumor specificity, rapid uptake, and low background activity. In lung cancer, the leading cause of cancer-related mortality worldwide, FAPI outperforms [^{18}F]FDG PET/CT in certain clinical scenarios, particularly in mediastinal lymph node staging and in the detection of brain, pleural, and bone metastases of NSCLC. However, [^{18}F]FDG PET/CT has set a high standard, and current evidence remains insufficient for clinical implementation of FAPI PET/CT, particularly regarding its potential for evaluating treatment response. To date, no studies have been published on response evaluation using FAPI PET/CT in NSCLC. Therefore, the aim of this interim analysis is to evaluate if tumor response assessed with FAPI PET/CT correlates to established response evaluation criteria such as the Response Evaluation Criteria in Solid Tumors (RECIST), as a secondary objective of a prospective exploratory study evaluating the prognostic value of FAPI PET/CT in NSCLC patients (ClinicalTrials.gov; NCT06107608). Moreover, we aimed to validate the immune PET response criteria in solid tumors (iPERCIST) using [^{18}F]FDG PET/CT in this cohort of NSCLC patients treated with (chemo)immunotherapy.

Methods

In this prospective study, stage III/IV NSCLC patients with an indication for immunotherapy (IO) (+/- chemotherapy) were included. Both [^{68}Ga]Ga-FAPI-46 PET/CT and [^{18}F]FDG PET/CT were performed at baseline and after the first 2 cycles of (chemo)IO. The injected activity of [^{68}Ga]Ga-FAPI-46 was 1,5 – 2 MBq/kg and the time per bed position 2 - 2.5 minutes on a GE Discovery MI 4 Ring PET/CT. Patients were actively followed and underwent [^{18}F]FDG PET/CT every 2 to 4 treatment cycles during a period of 24 weeks. Response was evaluated by an experienced radiologist using RECIST1.1 criteria on contrast-enhanced CT (ceCT) or MRI. PET parameters were assessed quantitatively (standardized uptake values (SUVs) and volume-based PET parameters) on both [^{18}F]FDG and FAPI PET/CT, based on the 1-hour post injection attenuation-corrected (AC) PET reconstructions. A correlation analysis of the relative change in quantitative [^{18}F]FDG and FAPI PET parameters in the primary tumor after 2 cycles of (chemo)IO was performed. The difference in the kinetics of FAPI PET imaging biomarkers between the iRECIST1.1 response categories was analyzed using an unpaired T-test.

Results

To date, 30 patients have undergone baseline FAPI PET/CT, however, 5 were deemed screen failures due to a change in the treatment plan or a rapid decline in their condition. Of the 25 patients included, 20 (80%) were diagnosed with an adenocarcinoma, 3 (12%) with a squamous cell carcinoma, and 2 (8%) with a carcinoma not otherwise specified (NOS). 22 patients have started treatment, which was immunotherapy monotherapy in 11 patients (50%), and combined chemo-IO in the other half of the patients. In all 25 patients, a high FAPI uptake in the neoplastic lesions was observed, with a mean SUVmax of 14.8 in the primary lung tumor on the baseline FAPI PET/CT (range 5.9 – 23.4). After two cycles of (chemo)IO, both iRECIST and iPERCIST evaluations were available for 17 patients, revealing a near-complete concordance in response categories (Table 1). Regarding the SUVmax changes of the primary tumor after 2 cycles of (chemo)IO, a significant and strong correlation was found between [^{18}F]FDG and FAPI PET/CT in the 14 patients evaluable (Pearson correlation coefficient = 0.74; p=0.002) (Figure 1). There was a significant difference in FAPI ΔSUVmax between the partial response (iPR; mean ΔSUVmax -0.49; range -0.67 to -0.22) and stable disease (iSD; mean ΔSUVmax -0.03; range -0.2 to 0.29) iRECIST1.1 response categories (p = 0.001) (Figure 2).

Conclusions

FAPI PET/CT demonstrates significant potential as a sensitive and reliable imaging modality for assessing treatment response in patients with NSCLC, as evidenced by this interim analysis showing a strong correlation with established response evaluation criteria. Additionally, the analysis highlights the validation of the immunotherapy-modified [^{18}F]FDG PET response criteria (iPERCIST) in this small cohort of NSCLC patients. Further inclusion is needed to confirm these findings in a larger cohort of patients.

Figures

iRECIST / iPERCIST	iSD	iPR	iUPD
iSMD	6	0	0
iPMR	1	8	0
iUPMD	0	0	2

Table 1 iRECIST versus iPERCIST (on [^{18}F]FDG PET/CT) response categorization after 2 cycles of (chemo)IO. iSD = Stable Disease according to iRECIST, iPR = Partial Response according to iRECIST, iUPD = Unconfirmed Progressive Disease according to iRECIST; iSMD = Stable Metabolic Disease according to iPERCIST, iPMR = Partial Metabolic Response according to iPERCIST, iUPMD = Unconfirmed Progressive Metabolic Disease according to iPERCIST.

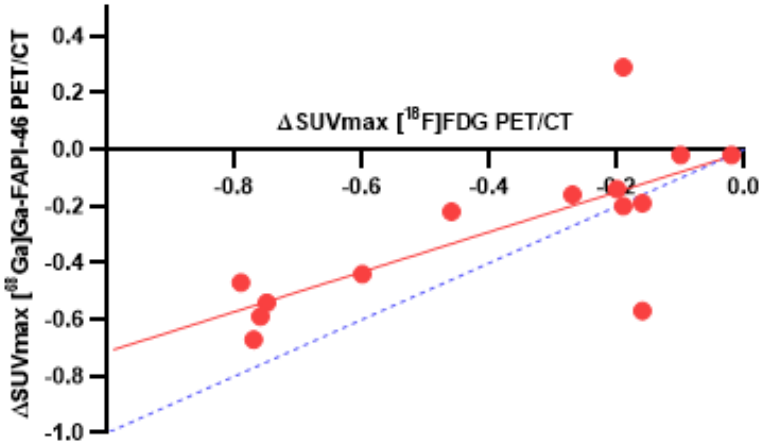

Figure 1 *Correlation of ΔSUVmax in the primary tumor on [^{18}F]FDG versus [^{68}Ga]Ga-FAPI-46 PET/CT after 2 cycles of (chemo)IO, showing a significant strong correlation (r = 0.74; p = 0.002). Red line: linear regression line; Blue dashed line: line of identity.*

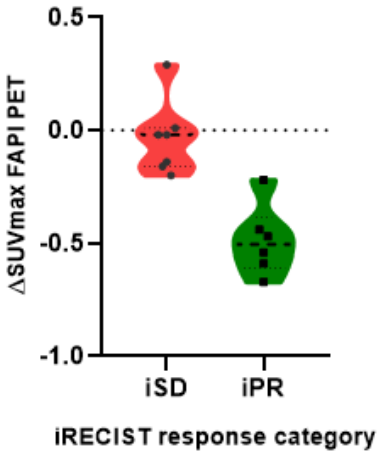

Figure 2 Violin plot of FAPI ΔSUVmax of the primary tumor per iRECIST1.1 response category, with a significant difference in mean ΔSUVmax between the iRECIST Stable Disease (iSD; mean ΔSUVmax of -0,03) and the iRECIST Partial Response (iPR; mean ΔSUVmax of -0,49) categories (p = 0,001).

PROSTATE-SPECIFIC MEMBRANE ANTIGEN (PSMA) EXPRESSION IN PATIENTS WITH METASTATIC TRIPLE NEGATIVE BREAST CANCER: FINAL RESULTS OF THE PRISMA STUDY

Martin Manley,[1], Guilherme Nader Marta,[2], Ayca Arcay Ozturk,[1], Loubna Taraji,[1], Philippe Aftimos,[3], Zena Wimana,[4], Roberto Salgado,[5], Patrick Flamen,[1], Geraldine Gebhart,[1]

[1] Institute Jules Bordet; Nuclear Medicine, [2] Harvard Medical School; Dana-Farber Cancer Institute; Medical Oncology, [3] Institute Jules Bordet; Medical Oncology, [4] Institute Jules Bordet; Radiopharmacy; Nuclear Medicine, [5] Institute Jules Bordet; Breast Cancer Translational Research Laboratory; Pathology

Aims
Radioligand therapy (RLT) targeting prostate-specific membrane antigen (PSMA) prolongs survival in patients with prostate cancer. Immunohistochemistry-based studies suggest that PSMA is highly expressed in the tumor-associated neovasculature of triple-negative breast cancer (TNBC). In this study, we assesed PSMA expression in patients with metastatic TNBC (mTNBC) via [^{68}Ga]Ga-PSMA-11 positron-emission tomography/computed tomography (PSMA PET/CT) to evaluate the feasibility of PSMA-targeted RLT for mTNBC.

Methods
PRISMA is a prospective, single-center study that enrolled 20 patients with progressive mTNBC. Patients undergoing FDG PET/CT with PET Response Criteria in Solid Tumors (PERCIST)-evaluable disease underwent PSMA PET/CT. For qualitative analysis, healthy liver uptake was used as a patient-specific reference. Patients were classified as PSMA-positive if PSMA uptake in the majority of lesions was higher than healthy liver uptake. For semi-quantitative analysis, target-lesions (TLs) were defined and segmented as ≥1.5 cm in diameter and PERCIST measurable on FDG PET/CT. TL volumes were propagated to the PSMA PET/CT and anatomically matched to measure maximum standard uptake value corrected for body weight (SUVmax) for each TL. Mann-Whitney U test was used to compare mean SUVmax between subgroups based on age, prior therapy and androgen receptor status.

Results
Twenty patients were evaluable for analysis. On qualitative analysis**,** 10 (50%) patients were classified as PSMA positive. Semi-quantitatively, the mean SUVmax on PSMA PET/CT of all TLs (total 106) was 6.5 (range 1.4 – 28.0). Overall, 71 (67%) TLs had PSMA SUVmax greater than their respective healthy liver. In 7 (35%) patients, all TLs showed PSMA uptake higher than healthy liver. In 13 (65%) patients, the majority of TLs demonstrated PSMA SUVmax higher than healthy liver. All TLs exhibited an SUVmax above the patient specific blood pool. Ongoing tumor histopathology is available for 11/20 patients, of which 10/11 expressed PSMA in endothelial cells. Mean PSMA SUVmax was higher in patients who received < 3 lines of prior therapy, underwent immunotherapy, and who had negative androgen receptor status.

Conclusions
This study represents the largest prospective imaging evaluation of PSMA expression in a homogeneous cohort of patients with pretreated metastatic TNBC using [^{68}Ga]Ga-PSMA-11 PET/CT, demonstrating that the majority of TLs exhibited PSMA uptake exceeding that of healthy liver tissue. Although there is inter- and intra-patient heterogeneity, these findings reinforce the potential of PSMA as a therapeutic target in mTNBC. Further investigation of PSMA-targeted RLT as a treatment approach in select TNBC patients is warranted.

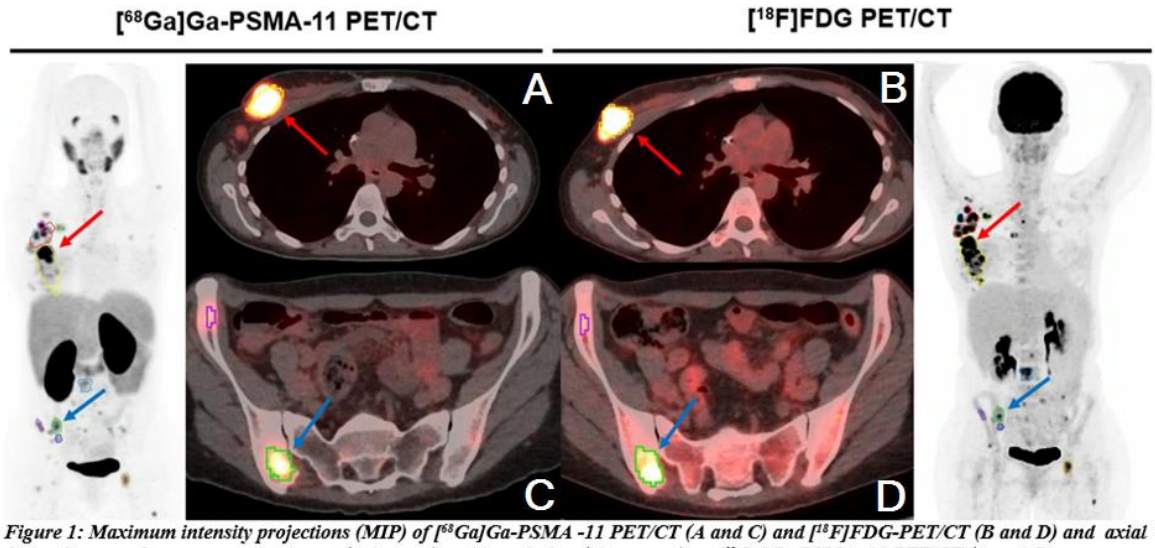

Figure 1: Maximum intensity projections (MIP) of [^{68}Ga]Ga-PSMA -11 PET/CT (A and C) and [^{18}F]FDG-PET/CT (B and D) and axial fusion images of a representative breast (red arrow) and bone lesion (blue arrow) on [^{68}Ga]Ga-PSMA -11 PET/CT (A and C, respectively) [^{18}F]FDG-PET/CT (B and D, respectively). The PSMA SUVmax for the pictured breast and bone lesion are 19.6 and 11, respectively.

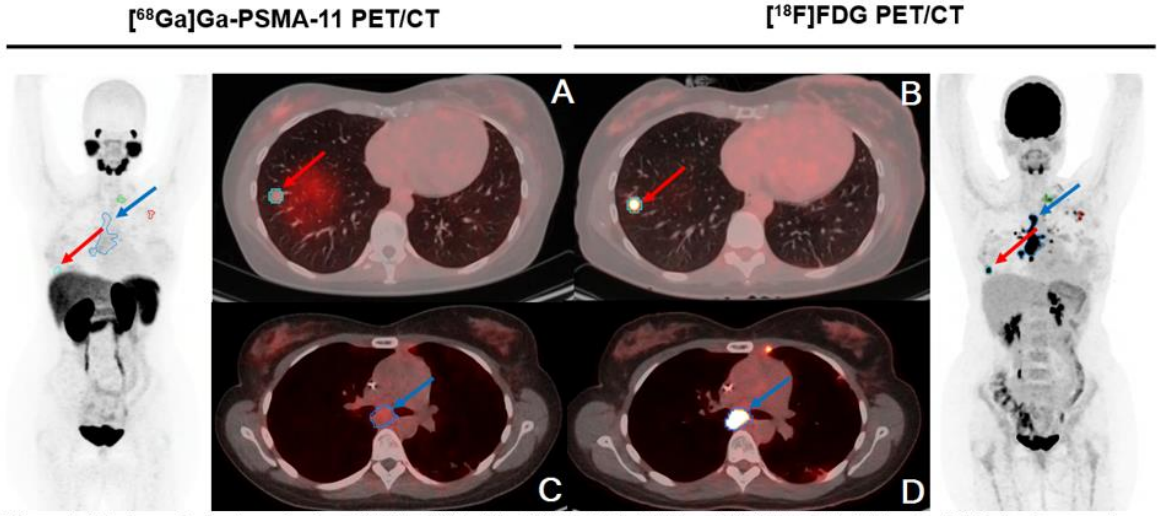

Figure 2: Maximum intensity projections (MIP) of [^{68}Ga]Ga-PSMA -11 PET/CT and [^{18}F]FDG-PET/CT and axial fusion images of a representative lung (red arrow) and a mediastinal lymph node metastasis (blue arrow) on [^{68}Ga]Ga-PSMA -11 PET/CT (A and C, respectively) and [^{18}F]FDG-PET/CT (B and D, respectively). The PSMA SUVmax for the lung and lymph node lesion are 4.6 and 4.7, respectively.

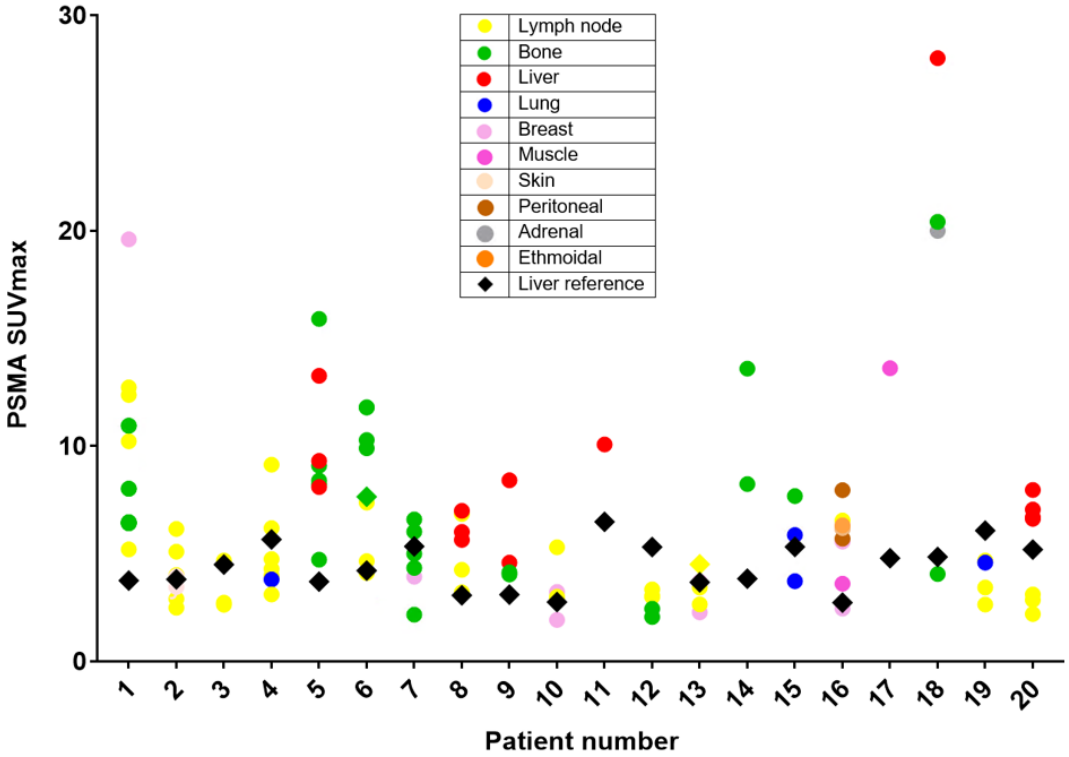

Figure 3: Graph of all 106 target lesions grouped per patient plotted against their respective PSMA SUV*max values. Black diamonds represent the SUVmean of healthy liver in each of the 20 included patients. Lesions are colored based on anatomical location. Color legend: LNM (yellow), Bone (green), Liver (red), Lung (blue), Breast (pink), Skin (tan), Ethmoidal (orange), Peritoneal (brown), Muscle (violet), Adrenal (grey).*

Characteristic	N (%)	Mean SUVmax (IQR)	p-value
Age			
< 50 years	11 (55%)	6.09 (3.72 – 8.28)	0.088
≥ 50 years	9 (45%)	4.22 (3.18 – 6.68)	
Prior Lines of Therapy			
< 3 lines	7 (35%)	6.47 (4.06 – 10.2)	0.038*
≥ 3 lines	13 (65%)	4.66 (3.44 – 7.38)	
Immunotherapy Received			
Yes	12 (60%)	6.2 (4.1 – 8.33)	0.009*
No	8 (40%)	4.02 (3.09 – 6.79)	
Androgen Receptor Expression	**13/20 available**		
0-9%	6 (30%)	6.44 (4.47 – 8.76)	0.004*
≥10%	7 (35%)	4.07 (3.01 – 6.38)	

*Table 1: Association Between Clinicopathologic Characteristics and Mean PSMA SUVmax in Patients with Metastatic TNBC. Abbreviations: SUVmax, maximum standardized uptake value; TNBC, triple-negative breast cancer; HER2, human epidermal growth factor receptor 2; AR, androgen receptor; IQR, interquartile range; * statistically significant*

EVALUATION OF [^{18}F]ALF-NOTA-OCTREOTIDE PET/CT IN ROUTINE CLINICAL USE: A RETROSPECTIVE ANALYSIS IN 288 NEUROENDOCRINE TUMOR PATIENTS

Hannes Leupe,[1], Frederik Cleeren,[2], Jeroen Dekervel,[3], Karolien Goffin,[4], Lennert Boeckxstaens,[5], Sander Jentjens,[6], Chris Verslype,[3], Christophe Dooms,[7], Filip Van Herpe,[8], Paul Clement,[9], Eric Van Cutsem,[10], Koenraad Van Laere,[11], Gertjan Rasschaert,[8], Guy Bormans,[12], Christophe Deroose,[13]

[1] Uz Leuven; Nuclear Medicine, [2] Ku Leuven; University of Leuven; Department of Pharmacy and Pharmacology, [3] Uz Leuven; University Hospitals Leuven; Digestive Oncology, [4] Uz Leuven; Uz Leuven; Nuclear Medicine, [5] Uz Leuven; Uz Leuven; Ku Leuven, [6] Maastricht University Medical Center; Uz Leuven; Beeldvorming, [7] Uzleuven; University Hospitals Leuven; Pulmonology, [8] University Hospitals Leuven; University Hospitals Leuven; Digestive Oncology, [9] Uz Leuven; University Hospitals Leuven; Oncology, [10] Uz Leuven; Head of the Digestive Oncology Unit, University Hospital Gasthuisberg; Digestive Oncology, [11] Uz/Ku Leuven; University Hospital Leuven; Department of Nuclear Medicine, [12] K.U. Leuven; University of Leuven; Lab Radiopharmacy, [13] Uz Leuven; Campus Gasthuisberg; Nuclear Medicine (Be 0419 052 173)

Aims [^{18}F]AlF-NOTA-octreotide has emerged as a reliable tracer for somatostatin receptor (SSTR) PET/CT in patients with neuroendocrine neoplasms (NENs). Although effective and logistically advantageous, there remains limited data on its routine clinical application, particularly for specific NEN subtypes less represented in the prospective trials that evaluated its diagnostic accuracy (e.g. NET G3). This study aims to assess the real-world clinical use of [^{18}F]AlF-NOTA-octreotide PET/CT, with an emphasis on uptake characteristics and referral patterns at our institution.

Methods A retrospective analysis was conducted on all patients referred for SSTR PET/CT at University Hospitals Leuven between March 1, 2023, and January 18, 2024. Relevant clinical and demographic data, along with procedural details, were collected. PET/CT imaging data was analyzed to quantify uptake parameters. Image analysis was performed using MIM version 7.3.4 (MIM Software Inc., Cleveland, Ohio). SST-positive lesions were delineated semi-automatically using a relative threshold based on SUV_{mean} of the liver (1.5 x SUV_{mean} + 2 SD).

Results A total of 322 [^{18}F]AlF-NOTA-octreotide PET/CT scans from 288 patients were evaluated, with 15 patients presenting with G3 NET, 15 with PPGL, 5 with NEC and 40 with lung NETs (table 1). In total, 4677 lesions were analyzed. Average injected activity was 208.5 ± 73.6 MBq, and the mean uptake time before imaging was 121 ± 14 minutes. Analysis of the referral patterns by SNMMI appropriate use criteria (AUC) showed that the majority of patients were referred for 'Monitoring of NETs seen predominantly on SSTR PET' , followed by 'Initial staging after histologic diagnosis' (figure 1). Mean SUV_{max} (and 95% CI) per WHO tumor grade is shown in figure 2. Mean SUV_{max} (and 95% CI) per lesion organ site is shown in figure 3. The values in the bars indicate the sample size. Mean values are depicted above the bars. Ongoing quantitative analysis aims to evaluate diagnostic accuracy compared with other diagnostic modalities available for specific NEN subtypes (NET G3, NEC, lung NET, …).

Conclusions This study provides essential real-world data supporting the use of [^{18}F]AlF-NOTA-octreotide PET/CT in NET patient management. Quantitative analysis shows sufficient tracer uptake in NET lesions irrespective of tumor grade or lesion organ. These findings further validate [^{18}F]AlF-NOTA-octreotide for routine clinical use.

Table 1.

	Patients (n)

Total	288
Primary tumor origin	
- **Small intestine**	107
- **Pancreas**	54
- **Lung**	40
- **CUP**	27
- **Rectum**	9
- **Sigmoid**	5
- **PPGL**	15
- **Meningioma**	8
- **Negative scan in patient without NEN diagnosis**	16
- **Other**	7
NEN WHO grade	
- **G1**	93
- **G2**	84
- **G3**	15
- **NEC**	5
- **Negative scan in patient without NEN diagnosis**	16
- **Unknown or N/A (e.g. lungNET, PPGL, …)**	75

Figure 1.

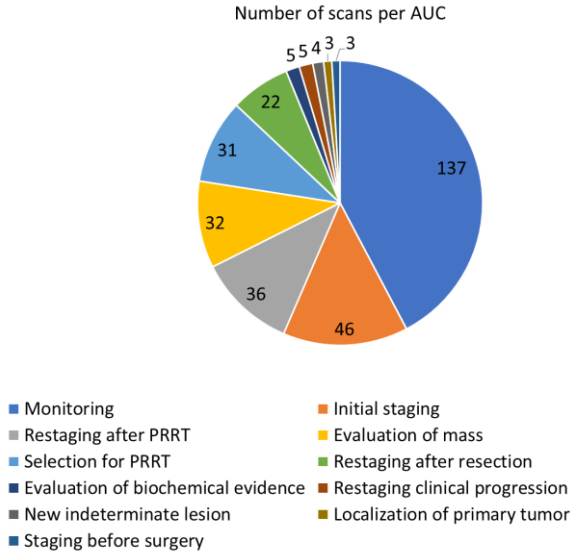

Figure 2.

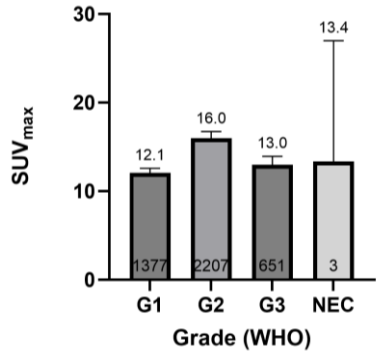
30
20
10
0
SUVmax
12.1
16.0
13.0
13.4
1377
2207
651
3
G1
G2
G3
NEC
Grade (WHO)

Figure 3.

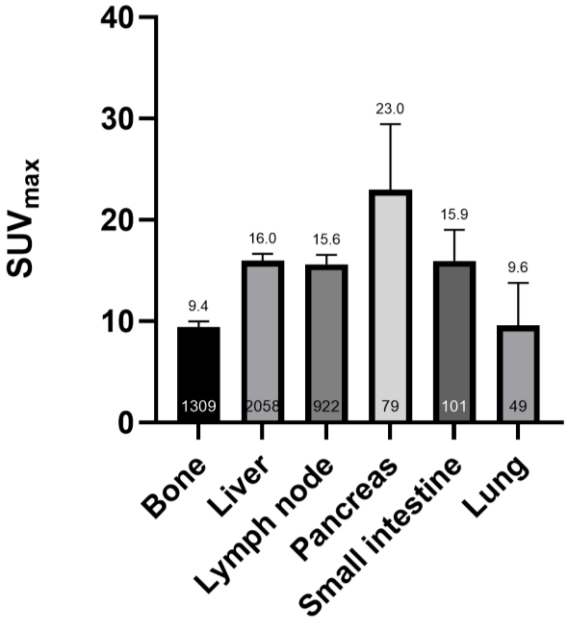
40
30
20
10
0
SUVmax
9.4
16.0
15.6
23.0
15.9
9.6
1309
2058
922
79
101
49
Bone
Liver
Lymph node
Pancreas
Small intestine
Lung

BRUGGE '25 BELNUC SYMPOSIUM
May 16-19 2025
23rd Symposium of the Belgian Society of Nuclear Medicine
www.belnuc.be | tel: +43 1 890 44 27 | office@belnuc.be

ADDITIONAL VALUE OF WHOLE-BODY MRI COMPARED TO PSMA PET IN BIOCHEMICALLY RECURRING PROSTATE CANCER

Anika Nys,[1], Niloefar Ahmadi Bidakhvidi,[2], Sander Jentjens,[3], Annouschka Laenen,[4], Gaëtan Devos,[5], Christophe Deroose,[6], Wouter Everaerts,[7], Steven Joniau,[8], Karolien Goffin,[9]

[1] Uz Leuven, [2] Uz/Ku Leuven; Nuclear Medicine and Molecular Imaging, Department of Imaging and Pathology, [3] Maastricht University Medical Center; Uz Leuven; Beeldvorming, [4] Ku Leuven; Interuniversity Institute for Biostatistics and Statistical Bioinformatics, [5] Uz Leuven; Urology, [6] Uz Leuven; Campus Gasthuisberg; Nuclear Medicine (Be 0419 052 173), [7] University Hospitals Leuven; Uz Leuven; Urology, [8] Urology, University Hospitals Leuven, Leuven, Belgium; Uz Leuven; Urology, [9] Uz Leuven; Uz Leuven; Nuclear Medicine

Background Prostate-specific membrane antigen (PSMA) positron emission tomography (PET) is the standard imaging modality for biochemical recurrence (BCR) of prostate cancer (PCa). However, the role of whole-body magnetic resonance imaging (wb-MRI) in this context remains unclear. This study evaluates the value of wb-MRI in addition to PSMA PET in patients with BCR PCa.
Methods This prospective, single-center trial included patients with BCR PCa, who underwent hybrid [^{68}Ga]Ga-PSMA-11 or [^{18}F]PSMA-1007 PET/MRI. Inclusion criteria required at least two years of follow-up data after the PET/MRI, including histopathological results, imaging, and post-treatment serum PSA response. PSMA PET and wb-MRI scans were independently assessed for suspicious malignant lesions at patient and region level. Lesion verification was based on follow-up data to classify true positive (TP) and false positive findings. We compared the TP detection rate, positive predictive value (PPV), and number of TP malignant lesions between PSMA PET and wb-MRI.
Results A total of 82 patients were included. At patient level, PSMA PET had a significantly higher TP detection rate than wb-MRI (100% vs. 66%, p=0.0005) and detected more TP lesions (mean 2.2 vs. 1.3, p=0.0021). At overall region level, PSMA PET outperformed wb-MRI in TP detection rate (90% vs. 60%, p=0.0042) and number of TP lesions (mean 2.0 vs. 1.0, p=<0.0001). Organ-specific analysis revealed a significantly higher number of TP lesions on PSMA PET for pelvic lymph nodes (mean 2.0 vs. 1.2, p=0.016) and all lymph nodes (mean 2.9 vs. 1.2, p=0.028). For all distant regions, PSMA PET showed a higher TP detection rate (95% vs. 60%, p=0.039). No significant differences were observed in PPV between PSMA PET and wb-MRI at patient level and all region levels.
Conclusions In patients with BCR PCa, wb-MRI (i) does not offer additional value over PSMA PET in terms of the TP detection rate, (ii) is equivalent to PSMA PET for PPV and (iii) detects significantly less TP lesions. Therefore, this study could not demonstrate the additional benefit of performing a standalone wb-MRI alongside PSMA PET in this setting.

YOUNG NUCLEARIST CHALLENGE

LIGHTING UP THE PATH TO RLT: A REMARKABLE PSMA-PET/CT CASE

Aster Marin,[1], Tim Van den Wyngaert,[2], Taco Cappenberg,[3], Sigrid Stroobants,[4]

[1] U Antwerpen, [2] Antwerp University Hospital; Nuclear Medicine, [3] Uz Antwerpen, [4] University Hospital Antwerp; University of Antwerp; Department of Nuclear Medicine

Case Presentation:
A 77-year-old man with a diagnosis of adenocarcinoma of the prostate 14.5 years ago (cT1cN0M0; Gleason 4+3; baseline PSA 9.8 µg/L) treated with brachytherapy developed biochemical recurrence (treated with goserelin and bicalutamide) and metastatic castration-resistant prostate cancer (mCRPC) (treated with abiraterone and prednisone), 5 years and 9 years after diagnosis, respectively. Docetaxel chemotherapy was started approximately 1.5 years ago due to disease progression. Despite a 50% PSA response after 6 cycles, a rapid increase was observed after 6 months, and the patient was referred for a workup for possible Lutetium-177 PSMA-targeted radioligand therapy (^{177}Lu-PSMA RLT).

PSMA-PET/CT revealed a highly heterogeneous PSMA expression across different lymph node metastases, with some retroperitoneal nodes demonstrating moderate uptake. In contrast, pathologically enlarged axillary and cervical nodes exhibited low to absent PSMA expression (whole-body SUV_{mean} 4.9). Additional FDG-PET/CT imaging confirmed discordant FDG-avid disease in the axillary and cervical metastases. Consequently, the patient was deemed ineligible for ^{177}Lu-PSMA RLT (Figure 1A and 1B). Subsequent treatments consisted of cabazitaxel (8 cycles), followed by enzalutamide due to rapid PSA progression, but no PSA response was observed. A follow-up PSMA-PET/CT for treatment guidance demonstrated significant disease progression, with an increase in the number and intensity of lymph node metastases with a striking upregulation of PSMA expression in previously low-uptake thoracic, axillary, and cervical nodes (whole-body SUV_{mean} 8.96) (Figure 1C). As a result, the patient was deemed eligible for ^{177}Lu-PSMA RLT. We hypothesize that this patient's intercurrent use of enzalutamide resulted in a long-term upregulation of PSMA expression.

Discussion:
^{177}Lu-PSMA RLT is the standard of care in treating mCRPC patients with disease progression after androgen receptor pathway inhibitors (ARPI) and taxane-based chemotherapy. It has been shown to improve overall survival and quality of life (1). However, low PSMA expression and discordant FDG-avid disease serve as exclusion criteria and are independently associated with poor prognosis (2). Of currently available therapies for mCRPC, only androgen receptor blockade has been demonstrated to upregulate PSMA expression (3,4). This phenomenon has been clinically confirmed by increased PSMA uptake on PSMA-PET/CT imaging following short-term induction therapy with enzalutamide (5). However, no reports are available describing the upregulation of PSMA in patients refractory to enzalutamide and with a sustained effect after stopping the treatment (6). The precise mechanism underlying this upregulation is not fully understood, although AR signaling's effect on gene expression is likely involved. (4) Interestingly, on the last available PSMA-PET/CT 3 months after cessation of enzalutamide, PSMA expression remained high (whole-body SUV3mean 8.85), without evidence of discordant FDG-avid lesions.

Conclusion:

To our knowledge, this is the only case report with long-term enzalutamide-induced upregulation of PSMA expression. This finding suggests that pharmacologically induced PSMA upregulation can potentially enable patients previously deemed ineligible to become candidates for ^{177}Lu-PSMA RLT. Further research is warranted to explore the mechanisms underlying this effect and its implications for the efficacy of ^{177}Lu-PSMA RLT.

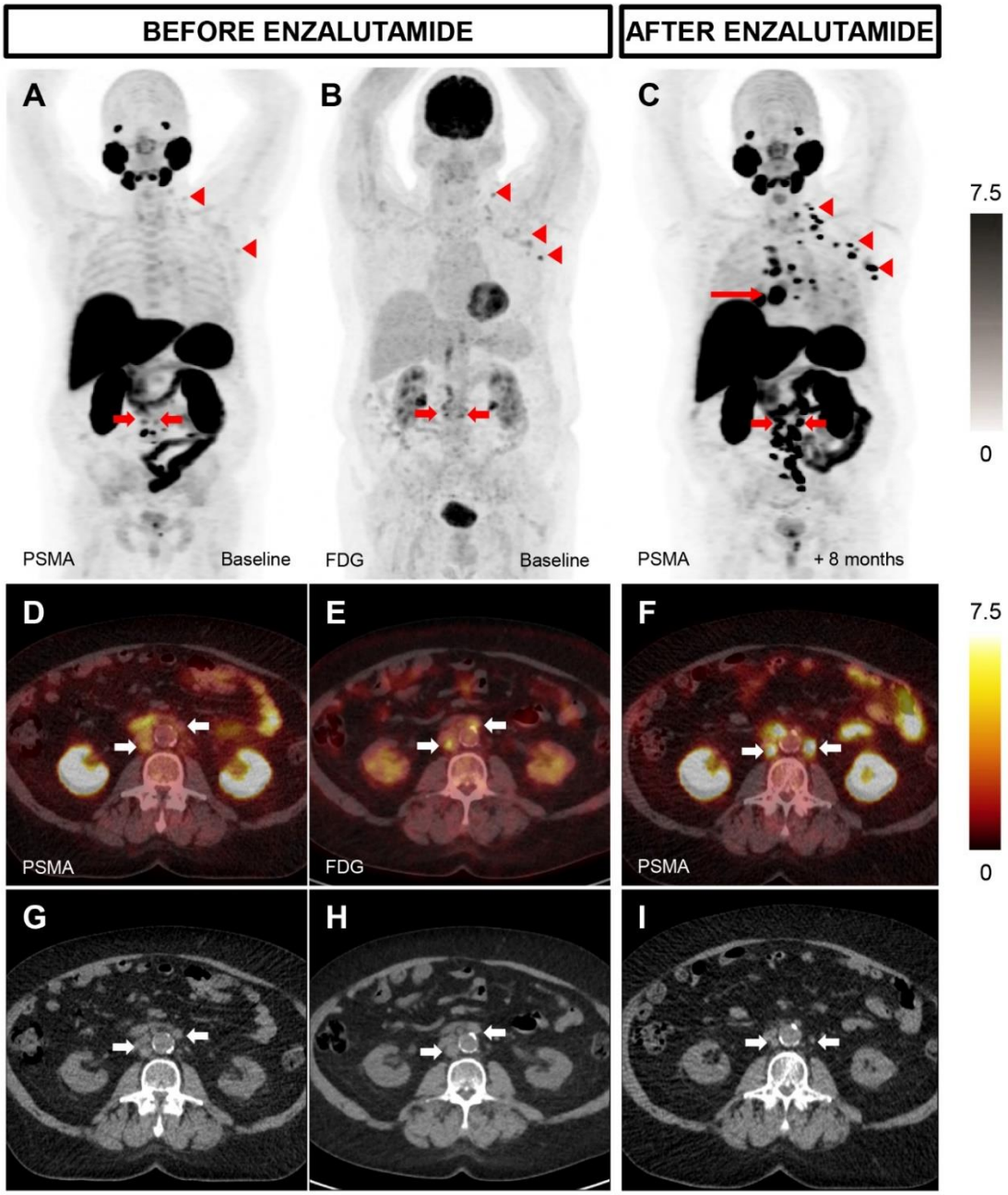

Figure 1. MIP images of the PSMA (A) and FDG (B) PET/CT scans at the time of disease progression with abiraterone, as well as the follow-up PSMA scan after enzalutamide (C), with corresponding axial slices of the PET/CT fusion images (D, E, F) and the CT images (G, H, I). Heterogeneous PSMA uptake is observed in the retroperitoneal lymph nodes, with nodes with low PSMA uptake but visible on FDG-PET/CT (small arrows in A and B). Discordant FDG avidity is seen

in the lower cervical and axillary lymph node metastases (arrowheads in A and B). Image C shows clear abdominal and retroperitoneal disease progression (small arrows) and prominent PSMA uptake in previously low-expressing cervical and axillary metastases (arrowheads). There are also new mediastinal and thoracic lymph node metastases (large arrow). Axial images demonstrate initially low PSMA and high FDG uptake in two retroperitoneal lymph nodes, with subsequent increase in PSMA uptake after enzalutamide treatment (arrows in D, E and F). Considering the comparable volumes between scans of the affected lymph nodes (image H and I), we can exclude partial volume effects as an explanation for the observed increase in intensity.

References:

(1) Sartor O, de Bono J, Chi KN, Fizazi K, Herrmann K, Rahbar K, et al. Lutetium-177-PSMA-617 for Metastatic Castration-Resistant Prostate Cancer. N Engl J Med. 2021;385(12):1091-103.

(2) Kuo PH, Morris MJ, Hesterman J, Kendi AT, Rahbar K, Wei XX, et al. Quantitative 68Ga-PSMA-11 PET and Clinical Outcomes in Metastatic Castration-resistant Prostate Cancer Following 177Lu-PSMA-617 (VISION Trial). Radiology. 2024;312(2).

(3) Kranzbuhler B, Salemi S, Umbricht C, et al. Pharmacological upregulation of prostate-specific membrane antigen (PSMA) expression in prostate cancer cells. Prostate. 2018;78:758–765.

(4) Murga J, Moorji S, Han A, et al. Synergistic co-targeting of prostate-specific membrane antigen and androgen receptor in prostate cancer. Prostate. 2015;75: 242–254.

(5) Rosar F, Dewes S, Ries M, et al. New insights in the paradigm of upregulation of tumoral PSMA expression by androgen receptor blockade: enzalutamide induces PSMA upregulation in castration-resistant prostate cancer even in patients having previously progressed on enzalutamide. Eur J Nucl Med Mol Imaging. 2020;47:687–694.

(6) Staniszewska M, Fragoso Costa P, Eiber M, Klose JM, Wosniack J, Reis H, Szarvas T, Hadaschik B, Lückerath K, Herrmann K, Fendler WP, Iking J. Enzalutamide Enhances PSMA Expression of PSMA-Low Prostate Cancer. Int J Mol Sci. 2021 Jul 11;22(14):7431.

A RARE CAUSE OF FEVER OF UNKNOWN ORIGIN AND A MASTER MIMICKER

Sébastien Mehaudens,1, Léa Frisson,2, Halil Yildiz,3, Veronique Roelants,4, Francois Jamar,5, Olivier Gheysens,6

[1] *Department of Nuclear Medicine, Cliniques Universitaires Saint-Luc, Brussels*
[2] *Department of Internal Medicine and Infectious Diseases, Cliniques Universitaires Saint-Luc, Brussels*

Case presentation

A 72-year-old man with no significant medical history was admitted to the internal medicine department because of fever (38.5°C), asthenia, fatigue, and headache for two weeks. Physical examination was largely unremarkable except for a mild systolic murmur. Laboratory tests revealed signs of an inflammatory syndrome with C-reactive protein at 121mg/L and an elevated white blood cell count (10670/µL), with increased proportion of neutrophils (71.4%). Both blood and urine cultures yielded negative results. Transthoracic echocardiography demonstrated aortic valve thickening but no vegetations indicative of endocarditis, a finding further corroborated by transoesophageal echocardiography. Due to the persistent inflammatory syndrome of unknown etiology, the patient was referred for an 18F-FDG PET/CT scan, which revealed an intensely hypermetabolic condensation in the right lower lobe as well as hypermetabolic mediastinal and upper abdominal lymphadenopathies raising the suspicion for pulmonary cancer or lymphoma (Figure). Subsequently, an endobronchial ultrasound-guided transbronchial needle biopsy of multiple mediastinal lymph nodes was performed. Histopathological examination revealed lymphoid hyperplasia with focal necrosis and neutrophilic infiltration, which suggested an infectious etiology. A broad infectious disease panel was ordered that was negative for tuberculosis, syphilis, brucellosis and Q fever. Ultimately, the infectious work-up identified a positive PCR for *Francisella tularensis* on tissue biopsy, further confirmed by positive serology and PCR on blood. Finally, the diagnosis of pulmonary tularemia with lymphadenopathies was established. The patient was treated with levofloxacin for two weeks, resulting in a gradual reduction of symptoms. Radiological follow-up with chest CT scans at one and three months demonstrated a substantial partial resolution, and the patient remained symptom-free.

Tularemia is a potentially life-threatening zoonotic infection caused by the Gram-negative coccobacillus *Francisella tularensis*. It is classified as a category A bioterrorism agent, alongside anthrax or smallpox. Its worldwide incidence remains poorly defined due to underreporting and underdiagnosis. In 2019, only four cases were reported in Belgium (https://www.ecdc.europa.eu/sites/default/files/documents/AER-tularaemia-2019.pdf).

While human-to-human transmission does not occur, the infection is typically contracted through ingestion of contaminated food/water, handling of infected animals or through bites from ticks or mosquitoes. More than 100 domestic and wild animals can serve as reservoirs for tularemia with rabbits, hares and rodents being the primary sources of human infection. Upon further history taking, the patient recalled an injury in a forest during his vacation in Italy, where hunters are accustomed to handling meat, but he could not remember any tick bites.

Pulmonary tularemia represents the most severe form of the disease, usually caused by inhalation of the bacteria or hematogenous spread. It typically presents as an atypical pneumonia and can lead to acute respiratory failure, secondary hematogenous spread or death without appropriate treatment. In contrast, ulceroglandular tularemia which accounts for 75% of the cases, is more benign and typically results from direct contact or tick bites. It presents with an ulcerative lesion, fever, chills and -sometimes widely enlarged- peripheral lymphadenopathies. Oculoglandular tularemia, one of the

rarest forms, is difficult to diagnose and is thought to arise from direct contact or contaminated water. It manifests itself as conjunctivitis with pre-auricular lymphadenopathies.

Treatment of tularemia is well-established and generally consists of one to three weeks of intravenous or oral aminoglycosides. Fluroquinolones (e.g. levofloxacin or ciprofloxacin) represent effective alternative treatments. In severe pulmonary cases, supportive care including ventilatory support or intravenous fluids is essential. Early diagnosis and treatment are crucial for preventing complications and ensuring a favourable outcome.

This case underscores the diagnostic challenges of tularemia, given its rarity and complex presentation that can mimic many other diseases and the delayed culture results. Physicians should be aware and maintain a high level of suspicion for this infectious disease. One should consider it in the differential diagnosis of patients with fever of unknown origin, even in the absence of a clear history of tick bites or other known exposure risks.

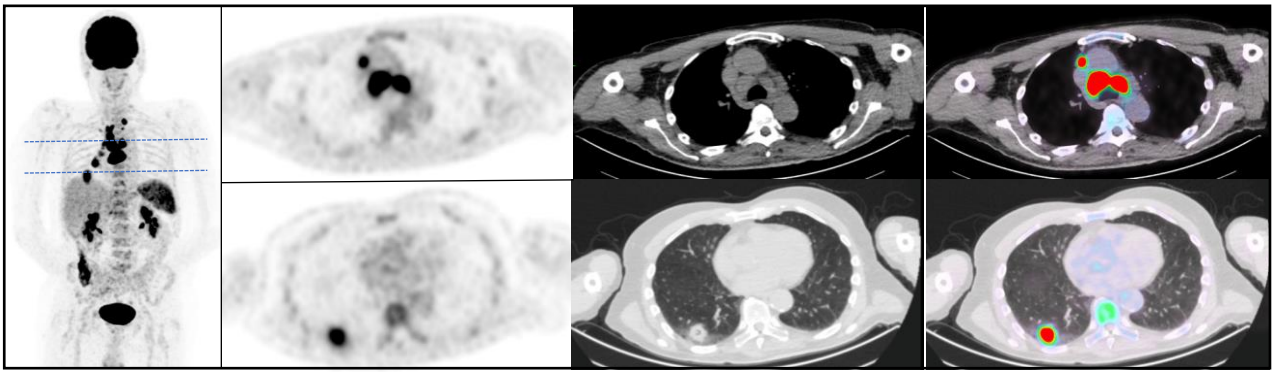

A DISEASE WITHOUT BORDERS: CASE SERIES ON EXTRAPULMONARY TUBERCULOSIS

Simon Gesquiere,[1], Bliede Van den Broeck,[2]

[1] Uz Gent; Uz Gent; Nuclear Medicine, [2] Uz Gent; Uz Gent

Tuberculosis (TB) remains one of the world's most significant public health challenges, with an estimated 1.3 million deaths in 2022 and millions affected globally (1). While pulmonary TB is the most common form, the infection is not confined to the lungs. TB can involve a variety of extrapulmonary sites, including the lymph nodes, pleura, skin, ear, nose, throat, genitourinary system, pericardium, gastrointestinal tract, bones, joints, and the central nervous system, often presenting diagnostic challenges due to nonspecific imaging characteristics. (2, 3)

Recent findings from a systematic literature review and meta-analysis have underscored the potential of FDG-PET/CT as an early detection method for TB, to identify lesions in the whole body. (4) We selected 5 cases to showcase the disease spectrum of extrapulmonary TB on FDG PET/CT.

Case 1:
A 34-year-old HIV-positive female from West Africa origin, residing in Belgium for three months, initially presented with several days of abdominal pain, high fever, anorexia, and occasional vomiting and diarrhea. Following her HIV diagnosis, HAART therapy was initiated. Initial clinical evaluation revealed a moderately distended abdomen, and laboratory tests showed a hemoglobin of 7.9 g/dL, and an elevated CRP (110 mg/L). An abdominal CT scan demonstrated significant free fluid, most pronounced in the paracolic gutters and pelvis, and diffuse thickening of the omentum and peritoneal folds, suggestive of an infectious or metastatic process.

Diagnostic laparoscopy revealed diffusely scattered peritoneal lesions with rice-grain-sized white nodules and turbid ascitic fluid. Histopathology identified granulomas with central necrosis and multinucleated giant cells, while immunohistochemical staining demonstrated spirochetal elements. An HIV infection with low CD4 cell count (36 cells/microL) was diagnosed. Empirical treatment with quadruple antituberculosis therapy initially resulted in clinical improvement. Antiretroviral therapy (ART) for the HIV infection was initiated.

However, after three weeks, the patient developed progressive abdominal distension with a painful, tube-shaped supraumbilical mass. FDG PET/CT evaluation revealed a hypermetabolic osteolytic lesion in the right first rib with adjacent soft tissue involvement (images A and B) and intensely active, diffuse peritoneal and omental infiltration with free pelvic fluid (images C and D). These findings are indicative of an immune reconstitution inflammatory syndrome (IRIS) of the underlying tuberculous infection following the initiation of antiretroviral therapy. The abnormalities on the FDG PET-scan resolved

under continued ART and antitberculous therapy.

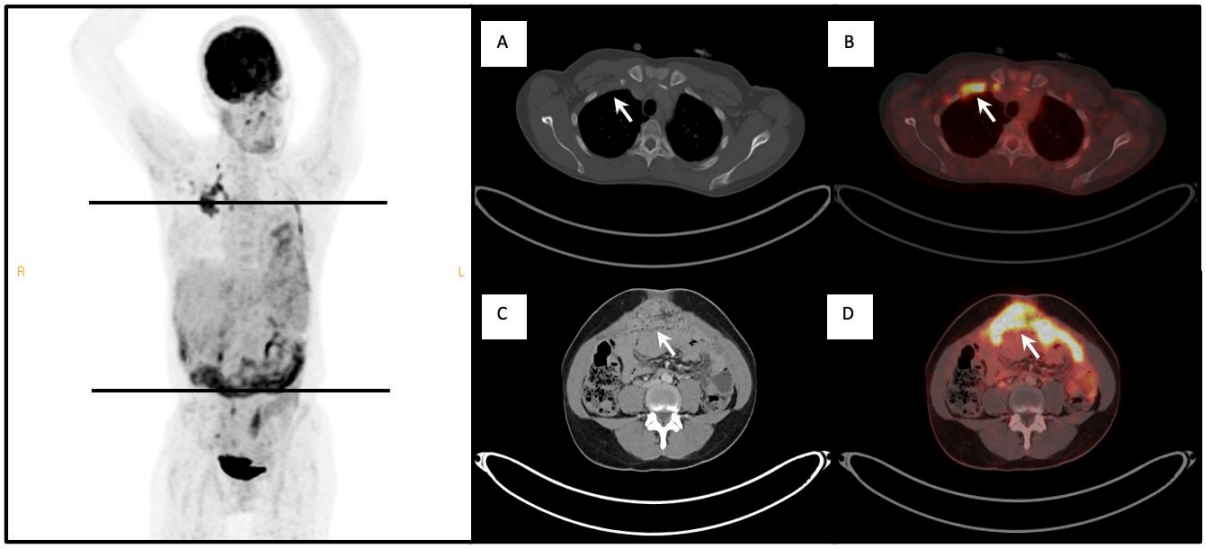

Figure 1 illustration of case 1; FDG PET/CT with MIP images and transversal CT and fusion images.

Case 2:

A 38-year-old male patient originally from Somalia, residing in Belgium since 2017, presented with a previous diagnosis of mediastinal tuberculous lymphadenitis (in 2019). Initially, the patient responded well to standard anti-tuberculous therapy; however, over the previous 2.5 months (in 2021), he experienced a relapse of symptoms. He reported progressive fatigue, lower back pain radiating to the upper thigh, discomfort in the right hemithorax, and an unintended weight loss. Laboratory evaluation revealed a markedly elevated CRP level of 105 mg/dL.

FDG PET/CT imaging demonstrated spondylodiscitis at the Th3-4 level (images A and B), accompanied by a paravertebral soft tissue component with possible extension into the spinal canal, leading to a secondary kyphotic deformity. Additionally, there was extensive osteomyelitis of the sacrum with a large presacral collection extending bilaterally through the greater ischiatic foramina (images C and D). A previously identified splenic nodule exhibited a hypermetabolic rim, suggestive of an active tuberculoma (images E and F). No active pulmonary lesions were identified, although an oval nodule in the lingula of the left lung was noted, likely representing a sequel. Diagnostic puncture of the large gluteal collection confirmed the presence of a multidrug resistant Mycobacterium tuberculosis,

supporting the diagnosis of a probable relapsing recurrent extrapulmonary tuberculosis.

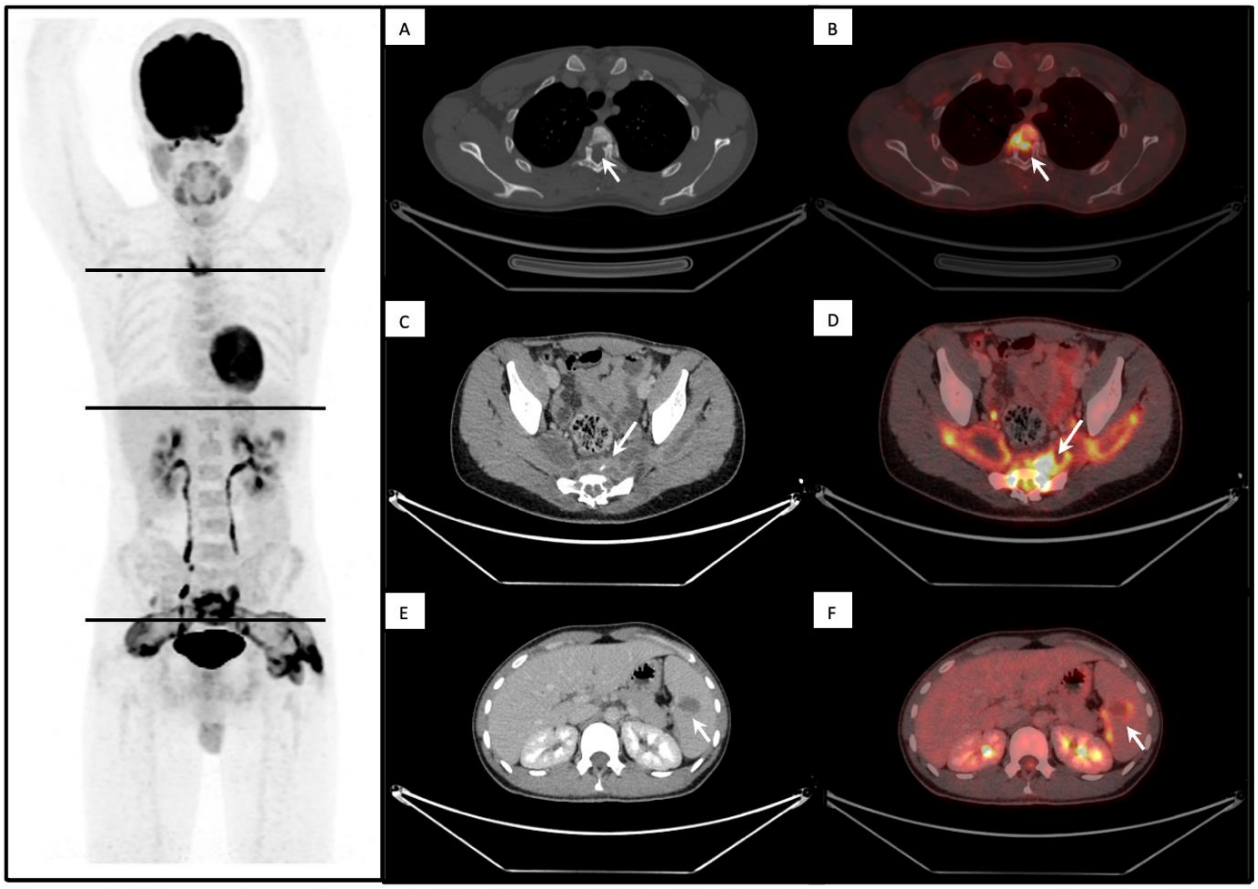

Figure 2 illustration of case 2; FDG PET/CT with MIP images, transversal CT and fusion images

Case 3:

A 43-year-old woman, originally from Somalia, underwent evaluation due to notable weight loss, generalized lymphadenopathy, and persistent lymphocytosis. She reported experiencing diffuse pain and systemic symptoms indicative of an inflammatory process, which was confirmed by abnormal laboratory inflammatory markers. Further investigation was undertaken with an FDG PET/CT scan, which revealed intensely hypermetabolic adenopathies in the periportal (images A and B) and retroperitoneal regions (images C and D). These lymph nodes demonstrated central necrosis and partial calcification. An excisional biopsy of a left axillary lymph node was performed for histopathological analysis, which revealed granulomatous lymphadenopathy with necrosis, and an interferon-gamma release assay (IGRA) returned positive, further supporting a diagnosis of tuberculosis. No microbiological cultures were obtained during the biopsy, leaving the differential

diagnosis between tuberculosis and an atypical mycobacterial infection unresolved.

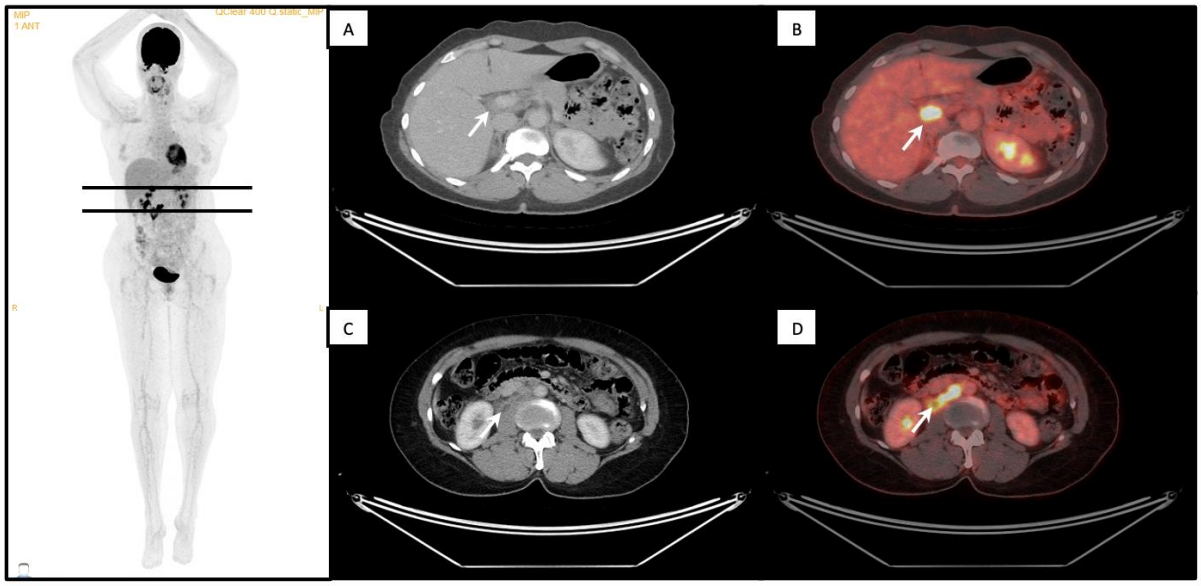

Figure 3 illustration of case 3; FDG PET/CT with MIP images, transversal CT and fusion images

Case 4:

A 13-year-old girl of Kenyan origin, residing in Belgium for 1 year and not having returned to Africa in the past year, presented with annular granulomatous skin lesions on the lower legs, which had developed over two months and rapidly deteriorated in the past month. A skin biopsy of the lower leg showed active and chronic, partially granulomatous and necrotizing dermatitis, suggestive of an infectious process. Both an IGRA test and Mantoux test were positive.

PET-CT findings revealed hypermetabolic lymphadenopathy (images A and B) in the right cervical, axillary, mediastinal, hilar, and retroperitoneal regions, as well as the right flank and inguinal areas. Diffuse cutaneous (images E and F) nodules and thickenings were observed on both lower legs and feet, with additional subcutaneous nodules on both gluteal regions and a hypermetabolic cutaneous area on the right forearm. Furthermore, an intensely metabolically active short-segment circumferential thickening of the ascending colon was noted (images C and D), accompanied by enlarged lymph nodes in the right flank. Arthritis of the right ankle was also present.

A biopsy of an infracarinal lymph node via esophageal ultrasound, a new skin biopsy, and aspiration of the right ankle joint were performed. Only on the lymph node biopsy it was possible to do a PCR,

confirming tuberculosis. Quadruple anti-tuberculosis therapy was initiated.

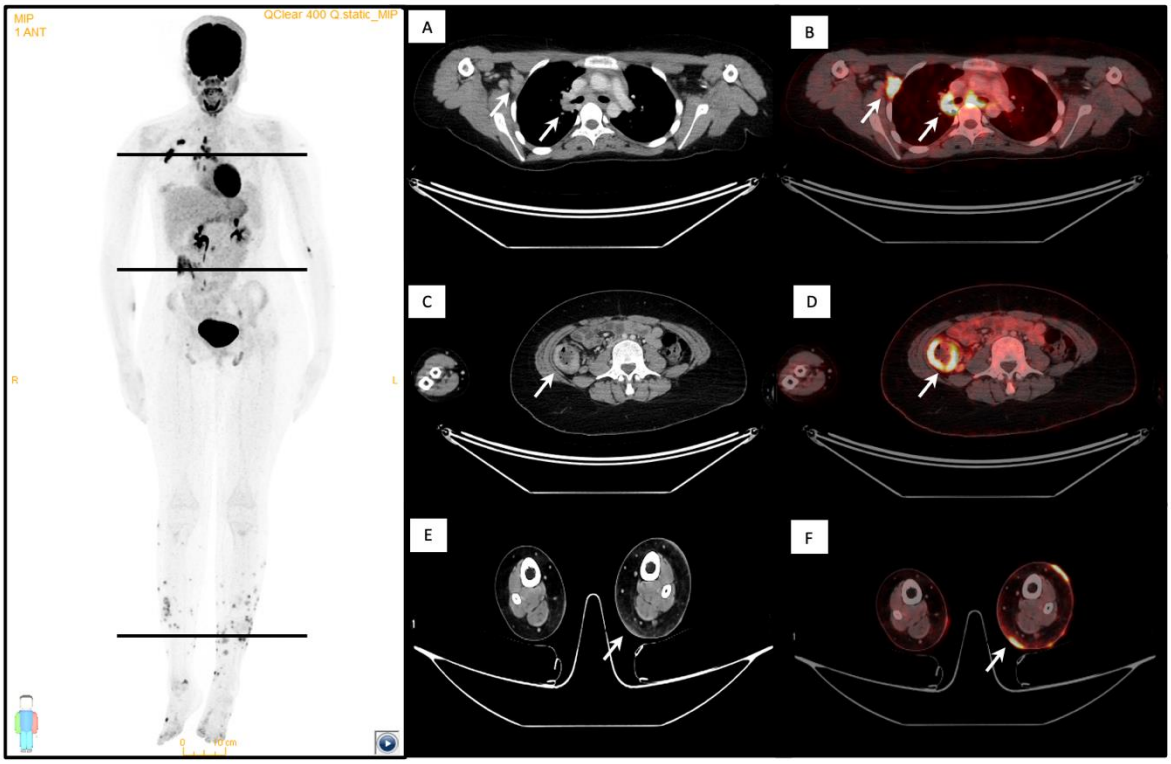

Figure 4 illustration of case 4; FDG PET/CT with MIP images, transversal CT and fusion images

Case 5:

A 13-year-old girl from Pakistan, who had been living in Belgium for four months, presented with a six-week history of persistent cough, vomiting, weight loss of 11 kg, low-grade fever, and general malaise. Clinical examination revealed diminished breath sounds and abdominal distension.

Initial hematological investigations showed pancytopenia and coagulation abnormalities. Biochemical tests indicated mildly elevated liver enzymes (AST 43 U/L, GGT 86 U/L, alkaline phosphatase 173 U/L), normal renal function, hypoalbuminemia (22 g/L), and elevated CRP (66 mg/L). A Mantoux test was negative, while an IGRA test was Positive. Acid-fast bacilli were identified in fasting gastric lavage samples.

Chest X-ray revealed bilateral patchy consolidations, and abdominal ultrasound demonstrated diffuse thickening of omental and mesenteric fat with ascites, suggestive of diffuse peritonitis or mesenteritis. Despite starting antituberculosis therapy, the patient showed insufficient clinical improvement and persistent fever, prompting an FDG PET/CT scan.

The PET/CT revealed central necrotizing adenopathy in the mediastinum and left hilum, along with lymph nodules in the pericardial fat. Alveolar consolidations and pulmonary nodules were scattered across all lung lobes. (Images A, B, C and D) Discrete hypodense lesions in the liver and spleen, consistent with hepatosplenic tuberculosis, showed minimal metabolic activity. Additionally, diffuse peritoneal hypermetabolism (Images E and F and multiple hypermetabolic skeletal foci (G and H), likely

granulomas, were observed. Currently she is still under antituberculous therapy.

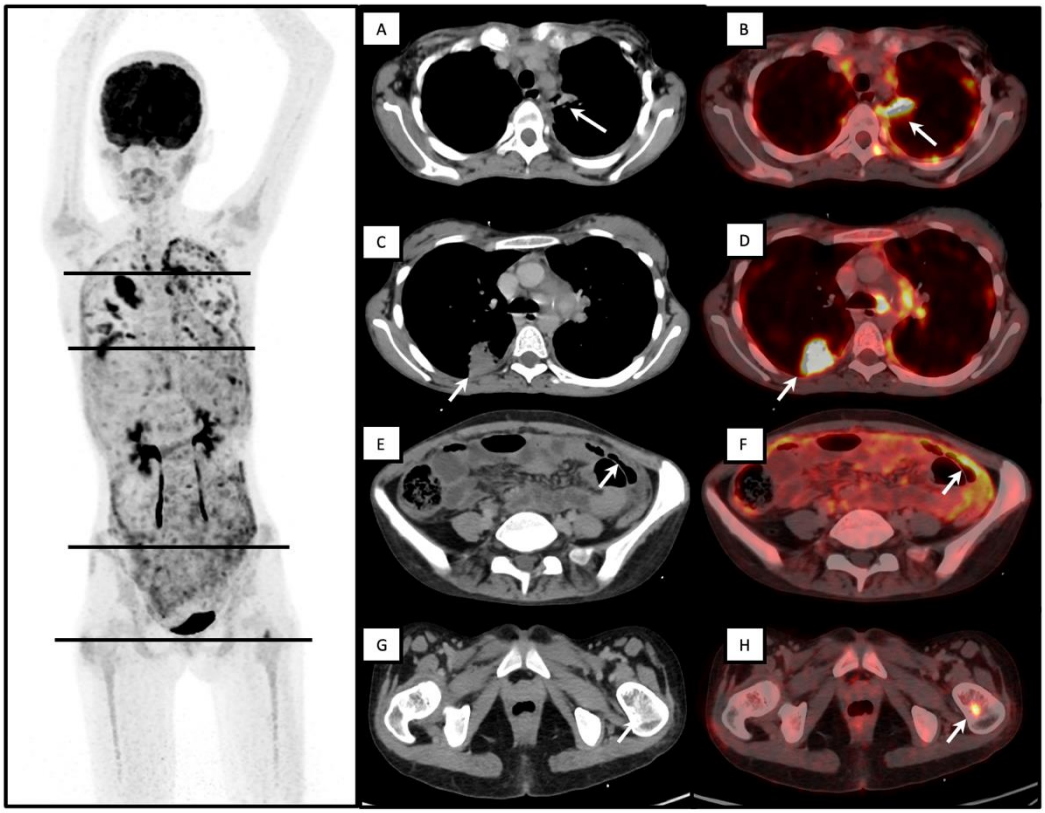

Figure 5 illustration of case 5; FDG PET/CT with MIP images, transversal CT and fusion images

REFERENCES

1. WHO. World TB Report 2024.
2. Kumar P, Clark M (2002) Textbook of clinical medicine. 9th edition
3. Tobin EH, Tristram D. Tuberculosis Overview. [Updated 2024 Dec 22]. In: StatPearls [Internet]. Treasure Island (FL): StatPearls Publishing; 2025 Jan-. Available from: https://www.ncbi.nlm.nih.gov/books/NBK441916/
4. Yayan J, Rasche K, Franke KJ, Windisch W, Berger M. FDG-PET-CT as an early detection method for tuberculosis: a systematic review and meta-analysis. BMC Public Health. 2024 Jul 29;24(1):2022. doi: 10.1186/s12889-024-19495-6. PMID: 39075378; PMCID: PMC11285570.

HER2-ABSOLUTELY KEY: MOLECULAR IMAGING IN METASTATIC BREAST CANCER

Alexis Philippot,[1], Martin Manley,[1], Evandro De Azambuja,[2], Patrick Flamen,[1], Géraldine Gebhart,[1]

[1] Hôpital Universitaire de Bruxelles (H.U.B.); Institut Jules Bordet; Nuclear Medicine, [2] Hôpital Universitaire de Bruxelles (H.U.B.); Institut Jules Bordet; Medical Oncology Department

A 76 years old woman was referred to our oncology department by her gynecologist, with acute swelling, edema and pain in the right upper limb, that she first noticed three weeks earlier. Relevant medical history includes a known hormone receptor positive (HR+), human epidermal growth factor receptor 2 negative (HER2-) right sided breast cancer, diagnosed 13 years prior. It was categorized initially as luminal invasive grade 3 localized breast cancer (cT2N0M0), for which she underwent neoadjuvant chemotherapy, followed by breast-conserving surgery and adjuvant radiotherapy. Her disease was then controlled under hormone therapy (anastrozole followed by tamoxifen) for 8 years.

At presentation, a contrast enhanced CT scan showed multiple infiltrations in the musculature of the right upper extremity (including biceps, triceps, pectoral and subscapular muscles). The tumor marker CA 15-3 was highly elevated (1823 IU/ml). The oncologist concluded malignancy recurrence and treatment was initiated with fulvestrant and ribociclib (anti-estrogenic and CD4/6 kinase inhibitor) prior to biopsy results due to the severity of her symptoms and the aggressive evolution. Biopsy results later showed triple-negative invasive lobular carcinoma, with Ki67 < 10% and negative PD-L1 status. Clinical response was initially good, with reductions in edema and CA 15-3 levels (from 2431 to 327 IU/ml after 2 months). Due to the positive evolution, the hormone treatment was continued despite triple negative status.

However, clinical progression occurred 4 months after initiation with increased pain, edema recurrence, and elevated CA 15-3 (1790 IU/ml). Re-staging by [^{18}F]FDG PET/CT (**Figure 1, A, B, C**) showed hypermetabolic right-sided axillary and supraclavicular lymph nodes and diffuse hypermetabolic muscular metastases in the right upper limb. Subsequent biopsy showed lobular carcinoma (HR- and HER2-). The patient was included in a prospective HER2 imaging study using a novel single-domain antibody-based tracer, [^{68}Ga]Ga-ABS011, to evaluate whether HER2 targeting therapy could be an option in the future. The scan (**Figure 1, D, E, F**) demonstrated high HER2-targeted tracer uptake matching the lesions identified on [^{18}F]FDG PET/CT, highlighting potential therapeutic targets.

This patient, initially diagnosed with HR+/HER2- breast cancer, is an example of HER2 expression heterogeneity in metastatic breast cancer. HER2 overexpression is associated with aggressive tumor behavior and poor prognosis.[1] However, HER2 expression can be heterogeneous within and between tumor sites.[2,3] Studies have demonstrated that HER2 heterogeneity is linked to reduced disease-free survival and can impact the efficacy of HER2-targeted therapies.[4] This heterogeneity necessitates accurate assessment methods to guide therapeutic decisions. In the IMPACT trial including 200 patients, Eisses et al., showed with ^{89}Zr-trastuzumab PET/CT that high HER2 expression was observed in one third of patients with a HER2-negative or –low metastasis biopsy.[5] Therefore, conventional biopsy methods do not fully capture the spatial and temporal heterogeneity of HER2 expression. Molecular imaging techniques, such as PET/CT with HER2-targeting tracers can offer non-invasive, whole-body assessments of HER2 status. The ZEPHIR trial, for example demonstrated that ^{89}Zr-trastuzumab PET/CT could predict responses to the HER2 targeting antibody-drug conjugate trastuzumab emtansine (T-DM1), highlighting its potential in personalized treatment planning.[6] In our case, despite initial biopsy results indicating triple-negative status, the HER2 targeting scan revealed high HER2 expression in metastatic lesions. This finding suggests potential eligibility for HER2-targeted

therapies in the future. Including HER2 imaging in the work-up of metastatic breast cancer patients could substantially improve therapy selection and ultimately improve patient outcomes in this patient population. Ongoing research is needed to validate HER2 targeting imaging.

At present, the patient is receiving chemotherapy treatment.

FIGURES

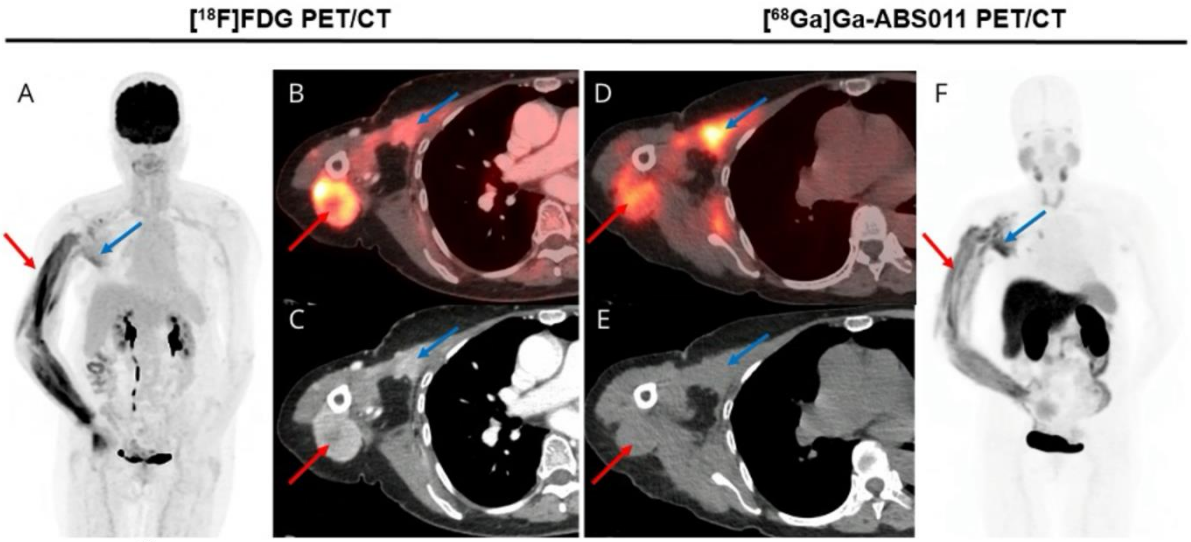

Figure 1: [^{18}F]FDG PET/CT Maximum intensity projection (**A**), axial fusion image (**B**) and axial contrast enhanced CT image (**C**), showing a hypermetabolic muscle metastasis in the triceps musculature of the right upper limb (SUVmax 7.6, red arrow) and a hypermetabolic metastasis in the right pectoral muscle (SUVmax 4.4, blue arrow). [^{68}Ga]Ga-ABS011 PET/CT Maximum intensity projection (**F**), axial fusion image (**D**) and axial CT image without contrast (**E**), showing elevated HER2 expression in the muscle metastasis in the triceps musculature of the right upper limb (red arrow) and the metastasis in the right pectoral muscle (blue arrow).

REFERENCES

1. Li Z, Metzger Filho O, Viale G, et al. HER2 heterogeneity and treatment response–associated profiles in HER2-positive breast cancer in the NCT02326974 clinical trial. *J Clin Invest*. 134(7):e176454. doi:10.1172/JCI176454
2. Geukens T, De Schepper M, Richard F, et al. Intra-patient and inter-metastasis heterogeneity of HER2-low status in metastatic breast cancer. *Eur J Cancer*. 2023;188:152-160. doi:10.1016/j.ejca.2023.04.026
3. Tarantino P, Ajari O, Graham N, et al. Evolution of HER2 expression between pre-treatment biopsy and residual disease after neoadjuvant therapy for breast cancer. *Eur J Cancer*. 2024;201. doi:10.1016/j.ejca.2024.113920
4. Buckley NE, Forde C, McArt DG, et al. Quantification of HER2 heterogeneity in breast cancer–implications for identification of sub-dominant clones for personalised treatment. *Sci Rep*. 2016;6(1):23383. doi:10.1038/srep23383
5. Eisses B, van Geel JJL, Brouwers AH, et al. Whole-Body HER2 Heterogeneity Identified on HER2 PET in HER2-Negative, -Low, and -Positive Metastatic Breast Cancer. *J Nucl Med Off Publ Soc Nucl Med*. Published online September 5, 2024:jnumed.124.267636. doi:10.2967/jnumed.124.267636

6. Mileva M, de Vries EGE, Guiot T, et al. Molecular imaging predicts lack of T-DM1 response in advanced HER2-positive breast cancer (final results of ZEPHIR trial). *NPJ Breast Cancer*. 2024;10:4. doi:10.1038/s41523-023-00610-6

WHEN THE PLEXUS GETS PERPLEXING

Louis Degryse,[1], Patrick Berkovic,[2], Christophe Dooms,[3], Adriana Dubbeldam,[4], Maarten Lambrecht,[2], Els Wauters,[5], Lennert Boeckxstaens,[6], Christophe Deroose,[7]

[1] Uzleuven; Nuclear Medicine, [2] Uzleuven; Radiotherapy, [3] Uzleuven; University Hospitals Leuven; Pulmonology, [4] Uzleuven; Radiology, [5] Uzleuven; Pulmonology, [6] Uz Leuven; Uz Leuven; Ku Leuven, [7] Uz Leuven; Campus Gasthuisberg; Nuclear Medicine (Be 0419 052 173)

A 75-year-old male with advanced-stage squamous cell lung carcinoma with thoracic wall invasion staged cT4N3M1c underwent chemo-immunotherapy (carboplatin–paclitaxel and pembrolizumab) combined with radiotherapy. A retrosternal recurrence was previously successfully treated with radiotherapy and the patient achieved a complete metabolic response on [18F]FDG PET/CT. Routine follow-up CT scans showed no recurrence.

One year later, the patient developed progressive right-arm paresis with refractory neuropathic pain. Electromyography (EMG) revealed significant abnormalities, suggesting brachial plexopathy. An additional MRI of the brachial plexus showed imaging findings consistent with denervation oedema in the right rotator cuff, which were also indicative of an inflammatory plexopathy. A radiation-induced etiology was initially suspected, with differential diagnoses including direct radiation damage to the brachial plexus or post-radiation fibrosis in the right upper pulmonary lobe. Given the low likelihood of functional recovery, management centered on symptomatic relief through duloxetine therapy and orthopedic support with a custom-fitted brace.

One year after symptom onset, due to intolerable pain and further progressive paresis, the routine semiannual thoracic CT was replaced by [18F]FDG PET/CT, which revealed intense hypermetabolic activity in an infiltrative lesion originating from the spinal nerve roots at C4–C5, extending into the right brachial plexus, highly suggestive of metastatic plexopathy. No other FDG-avid lesions were detected.

Based on the PET/CT findings for target volume delineation, the patient underwent re-irradiation in 10 fractions of 3 Gy to a total dose of 30 Gy. At the completion of radiotherapy, there was a significant reduction in pain symptoms, with the VAS score decreasing from 10/10 to 2/10, along with an improvement in fine motor function.

Metastatic brachial plexopathy is a rare but clinically significant manifestation of lung carcinoma recurrence, presenting primarily with severe neuropathic pain and upper limb paresis. Similar [18F]FDG PET/CT findings can be observed in brachial plexus neurolymphomatosis and metastatic plexopathy from breast carcinoma, with rarer occurrences in melanoma, sarcoma, head and neck squamous cell carcinoma, and malignant mesothelioma.

In patients with prior radiotherapy, distinguishing radiation-induced plexopathy from metastatic plexopathy poses a significant diagnostic challenge due to overlapping clinical and imaging features. While MRI remains the gold standard for brachial plexus structural evaluation, its limited ability to differentiate post-radiation changes from malignancy underscores the added diagnostic utility of [18F]FDG PET/CT.

This case underscores the pivotal role of [18F]FDG PET/CT in distinguishing metastatic plexopathy from post-treatment effects, directly influencing clinical decision-making in oncologic follow-up.

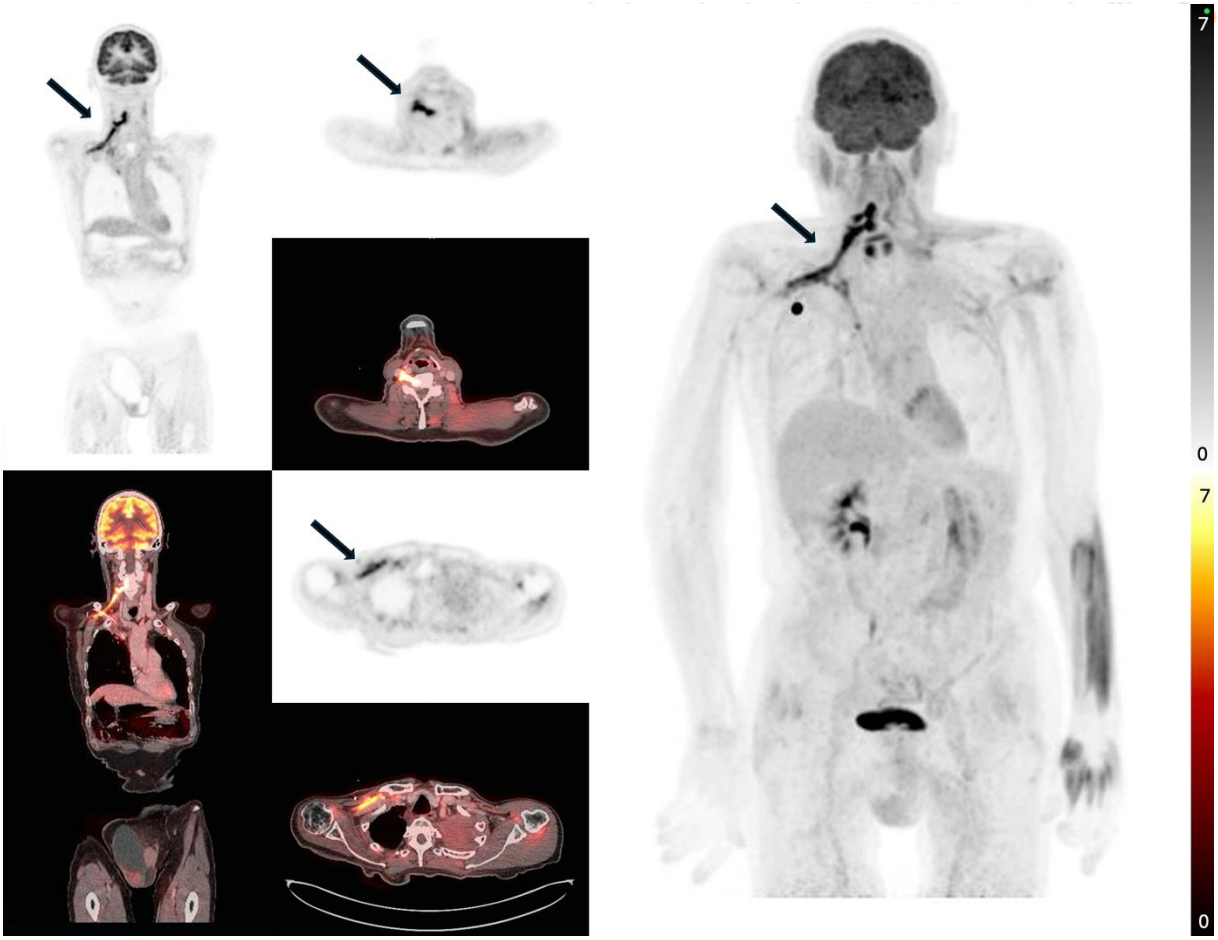

Figure 1: Coronal images, axial images and a MIP of a 75-year-old male patient with a highly hypermetabolic mass (black arrow) affecting the spinal nerve roots C4-C5 and extending through the right brachial plexus to retropectoral.

UNCOVERING A RARE CAUSE OF LOWER BACK AND BUTTOCK PAIN IN AN ELDERLY WOMAN

Emilie Jonard,[1], Caroline Chabot,[2], Thomas Schubert,[3], Renaud Lhommel,[4], Lokmane Taihi,[2], Olivier Gheysens,[5]

[1] Cliniques Universitaires Saint-Luc; Cliniques Universitaires Saint-Luc; Nuclear Medicine, [2] Cliniques Universitaires Saint-Luc; Radiology, [3] Cliniques Universitaires Saint-Luc; Orthopedic Surgery, [4] Cliniques Universitaires Saint-Luc; Cliniques Universitaires Saint-Luc; Médecine Nucléaire, [5] Clinique Universitaire Saint-Luc; Cliniques Universitaires Saint-Luc; Nuclear Medicine

A 62-year-old woman with no significant medical history presented with radiating pain from the lower back and buttock into the left leg, lasting for two years. Physical examination strongly suggested typical sciatica, prompting further evaluation with MRI and bone scintigraphy. MRI revealed lumbar discopathy at the L4-L5 and L5-S1 levels, significant spinal stenosis at L4-L5 and a marked L5-S1 left foraminal stenosis.

Bone SPECT-CT (Fig. a) showed no pathological uptake in the lumbar spine. However, a moderately increased uptake was observed in the posterior column of the left acetabulum. This area corresponded to a radiolucent region with central calcifications and peripheral reactive sclerosis. Although these imaging findings were non-diagnostic, they raised a high suspicion for a juxta-articular osteoid osteoma.

The patient subsequently underwent surgery, which included neurolysis and decompression of the entrapped left L5 nerve root, combined with a left-sided microdiscectomy at the L4-L5 level. Post-surgical recovery was uneventful, with complete resolution of the preoperative radicular pain.

However, five months later, intermittent left radicular pain returned, primarily localized in the buttock region. This recurrence was likely related to the lesion seen on bone SPECT-CT, as no other abnormalities were detected on the preoperative lumbar spine MRI. Consequently, further investigations with MRI and CT were performed. MRI revealed a relatively extensive bone marrow edema-like signal abnormality in the inferoposterior acetabulum, centered on a 7 mm focal lesion as well as a peak in signal enhancement during the arterial phase after gadolinium administration (Fig. b). The CT scan demonstrated a small intra-spongious lucency with central calcification, consistent with a nidus surrounded by perilesional osteosclerosis (Fig. c). These imaging findings confirmed the diagnosis of a juxta-articular osteoid osteoma in the posterior column of the left acetabulum. The lesion was successfully treated with radiofrequency ablation and the patient remained symptom-free thereafter.

This case highlights the atypical presentation and location of an osteoid osteoma, posing a diagnostic challenge, especially in elderly patients. Osteoid osteomas are small benign bone-forming lesions that are extremely rare in older women (less than 3% of cases in individuals over 30 years, with a male predominance of 3:1). The acetabular location is also uncommon, accounting for less than 1% of cases. Older adults often present with atypical symptoms; the typical nocturnal bone pain relieved by aspirin is less commonly observed in this age group.

This case underscores the diagnostic difficulty in identifying osteoid osteoma in elderly patients, whose symptoms may be atypical and overlap with more common conditions such as lower back pain.

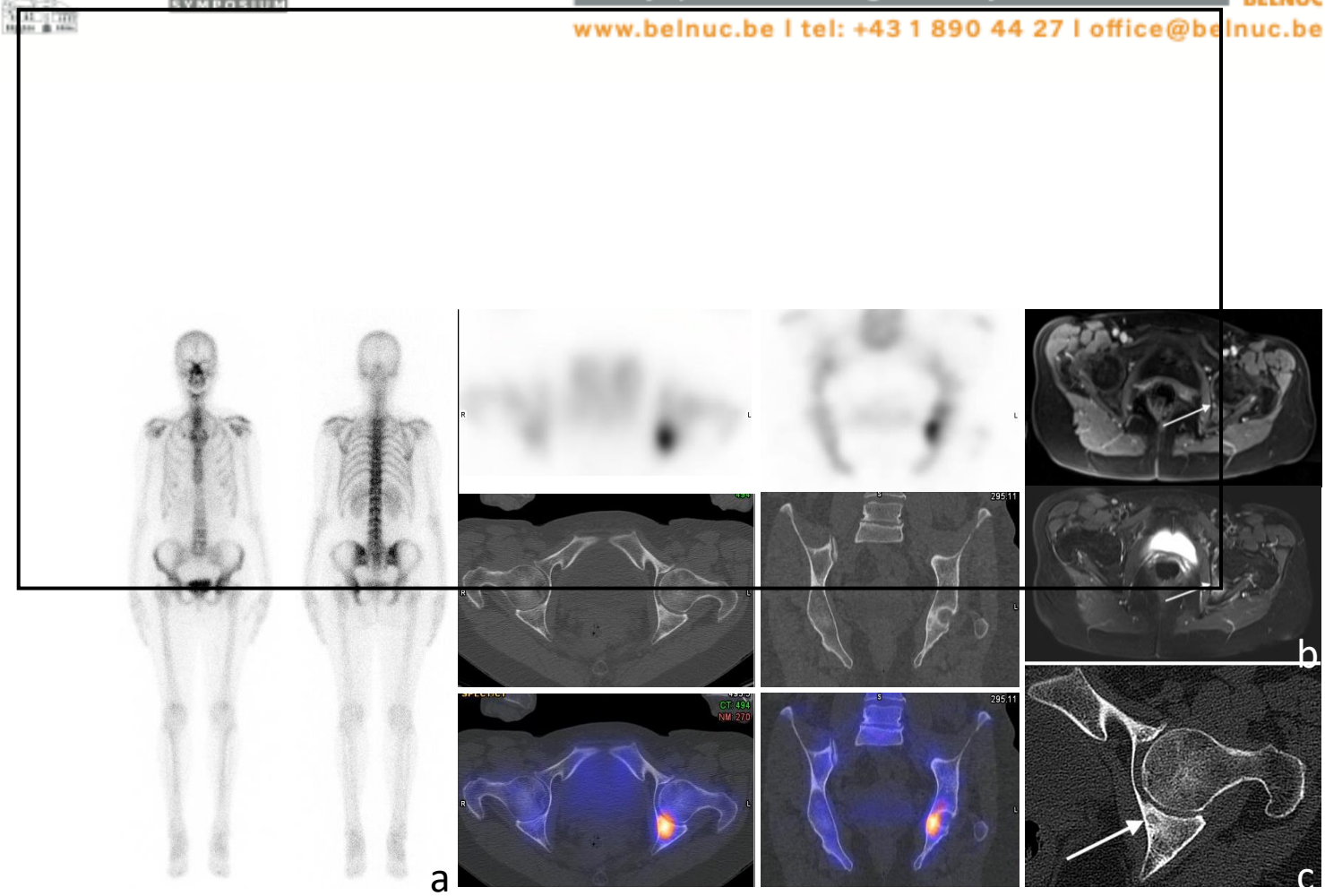
a
b
c

PREOPERATIVE LOCALIZATION OF CSF LEAKS USING RADIONUCLIDE CISTERNOGRAPHY

Odrade Gondry,[1], Pieter De Bondt,[1], Dirk Ooms,[1], Sim Vermeulen,[1], Benedicte Verhaeghe,[2], Paulien Moyaert,[3], Victor Nuttens,[4], Olivier De Winter,[1]

[1] Azorg; Nuclear Medicine, [2] Azorg; Otorhinolaryngology, [3] Uz Brussel; Azorg; Nuclear Medicine, [4] Ku Leuven; Azorg; Nuclear Medicine

Background

A cerebrospinal fluid (CSF) leak indicates a defect or tear in the dura mater. Although the most common cause is a head trauma, a CSF leak can also be iatrogenic or even spontaneous. In some cases, the leak is apparent, when clear fluid drains from the ear or nose, or when recurrent bacterial meningitis raises suspicion. However, many patients present with rather non-specific symptoms such as headaches, nausea or neck pain (1).
As untreated CSF leaks can lead to life-threatening complications such as meningitis, accurate diagnosis is crucial (2). The optimal diagnostic approach depends on the suspected location and underlying cause (3). Computed Tomography (CT) myelography and contrast-enhanced Magnetic Resonance Imaging (MRI) are often first-line imaging modalities. However when the leak is difficult to localize, radionuclide cisternography with ^{111}In-DTPA or ^{99m}Tc-DTPA can be highly effective. For suspected nasal leaks, the beta-2 transferrin test can also offer a non-invasive confirmation (4,5).

Case Presentation

A 49-year-old male with a history of head trauma and trepanation in 1996, was admitted to the hospital in March 2023 with bacterial meningoencephalitis. His medical history included a second frontal head injury several weeks prior, followed by the development of a headache and mild rhinorrhea, for which no medical advise was sought.
A follow-up MRI in August 2023 showed a spontaneous T1 hyperintense focus in the right frontal sinus, measuring 1 cm, located adjacent to the meninges. A small CSF leak could not be excluded. A subsequent CT later that year confirmed a focal bone defect at the level of the right lamina cribrosa. Surgical closure of the defect was planned.
To identify the exact location of the CSF leak, radionuclide cisternography was performed preoperatively. The patient received 185 MBq ^{99m}Tc-DTPA via lumbar puncture. Imaging was conducted using a 360° multi-headed CZT SPECT-CT system (Veriton-CT 200 series, Spectrum Dynamics) at 2, 4, and 22 hours post-injection (pi). The first acquisition was 3.5 min per bed position, and included a CT scan (100 kV; 21.12mAs) from the vertex to the feet. The second lasted 3.5 min per bed position and a CT was performed (100 kV; 19.4 mAs) from vertex to mid-thigh and the last was done with 5.1 min per bed position and a CT from vertex to mid-thigh (120 kV; 58.12 mAs).
At 2 hours pi, images appeared normal (Figure 1.A). By 4 hours pi, radiotracer uptake was observed in the right nasopharynx (Figure 1.B), suggestive of a CSF leak. At 22 hours pi, activity was also detected in the right nasal tampon, with uptake more anteriorly in the skull (Figure 1.C), further localizing the leak.
This led to surgical intervention aimed at closing the CSF leak at the level of the anterior cranial fossa. The defect was accessed through a right eyebrow incision, followed by the creation of a cranial bone flap to reach the skull base. Both intradural and extradural repair techniques were employed, utilizing a patch, TachoSil, and fibrin glue to ensure adequate closure of the defect.
The patient has currently returned to full-time work, and no recurrence of meningitis has been reported. However, no follow-up imaging has been performed to confirm complete closure of the CSF leak.
This case demonstrates that 3D SPECT/CT imaging enhances the precise localization of dural defects responsible for cerebrospinal fluid (CSF) leakage.

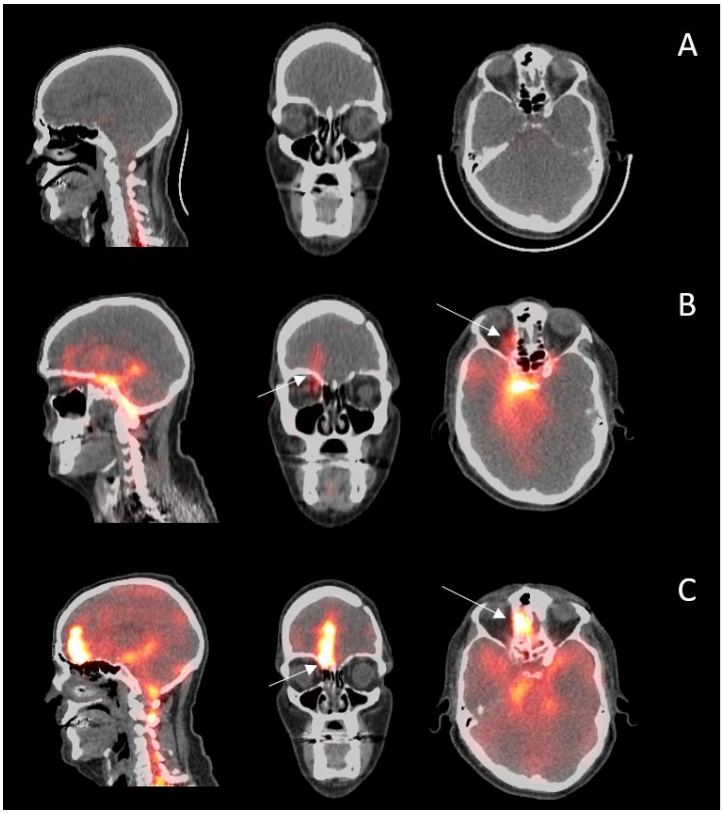

Figure 1: Here the site oft he leak, near the lamina cribrosa is shown at 2h pi (A), 4h pi (B) and 22h pi (C), in the sagittal, coronal and axial axis.

Sources

1. Severson M, Schaurich CG, Strecker-McGraw MK. Cerebrospinal Fluid Leak. [Updated 2023 Mar 6]. In: StatPearls [Internet]. Treasure Island (FL): StatPearls Publishing; 2025 Jan- Available from: https://www.ncbi.nlm.nih.gov/books/NBK538157/
2. Ter Horst L, Brouwer MC, van der Ende A, van de Beek D. Community-acquired Bacterial Meningitis in Adults With Cerebrospinal Fluid Leakage. Clin Infect Dis. 2020 May 23;70(11):2256-2261.
3. Xie M, Zhou K, Kachra S, McHugh T, Sommer DD. Diagnosis and Localization of Cerebrospinal Fluid Rhinorrhea: A Systematic Review. Am J Rhinol Allergy. 2022 May;36(3):397-406.
4. Hiremath SB, Gautam AA, Sasindran V, Therakathu J, Benjamin G. Cerebrospinal fluid rhinorrhea and otorrhea: A multimodality imaging approach. Diagn Interv Imaging. 2019 Jan;100(1):3-15.
5. Chan DT, Poon WS, IP CP, Chiu PW, goh KY. How useful is glucose detection in diagnosing cerebrospinal fluid leak? The rational use of CT and Beta-2 transferrin assay in detection of cerebrospinal fluid fistula. Asian J Surg. 2004 Jan;27(1):39-42.

WHEN HYPERTENSION 'NODS' TO A BIGGER PROBLEM

Justine Maes,[1], Marie Bex,[2], Brigitte Decallonne,[2], Karolien Goffin,[3], Steven Vanderschueren,[4], Christophe Deroose,[5]

[1] Uz Leuven; Nuclear Medicine, [2] Uz Leuven; Endocrinology, [3] Uz Leuven; Uz Leuven; Nuclear Medicine, [4] Uz Leuven; Internal Medicine, [5] Uz Leuven; Campus Gasthuisberg; Nuclear Medicine (Be 0419 052 173)

A 21-year-old female patient with no significant past medical history presented to her general practitioner for a routine consultation with a request for oral contraception. During this consultation, she was found to have grade II arterial hypertension (confirmed by home monitoring). She also reported intermittent palpitations and a long-standing history of headaches. There were no other systemic complaints. Her mother had essential hypertension, otherwise there was no other notable family history.
The patient was then referred to our centre for the work-up of the arterial hypertension. On examination, the patient exhibited no signs of significant systemic disease. Blood pressure readings confirmed grade II hypertension. Biochemically, the patient showed no elevated inflammatory markers and a mild decline in renal function, with an eGFR of 73 mL/min/1.73 m^2 and a serum creatinine of 1.08 mg/dL

Further evaluation of the hypertension was planned:

- The ECG showed signs of atrial and ventricular hypertrophy along with sinus tachycardia (heart rate of 119 bpm), suggesting ongoing cardiovascular strain likely related to the hypertension. A TTE was scheduled.
- Urinalysis showed limited proteinuria (PCR 0.36 g/g creatinine).
- The patient had recently undergone a reassuring ophthalmologic examination.
- An ultrasound of the kidneys and adrenal glands was planned to look for any signs of nephropathy, to rule out renal artery stenosis and to evaluate the adrenal glands.
- A 24-hour urinary metanefrine and catecholamine excretion measurement was planned.

The biochemical test panel unexpectedly revealed a hypercalcemia (3.62 mmol/L (normal range: 2.2-2.6 mmol/L)) and a low serum phosphate level. A markedly elevated PTH of 617 ng/L (normal range 14.9 - 56.9 ng/L), established the diagnosis of primary hyperparathyroidism. Furthermore, an isolated increase in alkaline phosphatases was discovered.

The patient was admitted to the endocrinology unit for intravenous fluids, a calcimimetic, vitamin D replacement and localisation studies. Ultrasound revealed a well-demarcated hypoechogenic mass posterior to the right upper pole/interpolar region of the thyroid measuring 22 x 16 x 29 mm (Fig. 1).

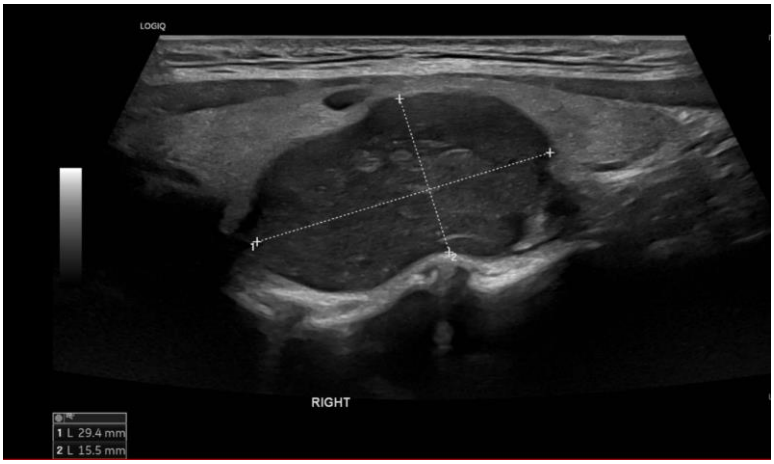

Fig. 1; Parathyroid ultrasound.

To assess for ectopic parathyroid tissue, a dual isotope parathyroid scintigraphy was performed.

The ^{123}I scan showed normal tracer distribution in the thyroid gland except for a zone of relative hypocaptation at the upper pole of the right thyroid lobe. The ^{99m}Tc-Sestamibi scan showed increased tracer uptake posterior to the upper pole of the right thyroid lobe. The subtraction images showed a clear localization of a parathyroid mass (see Fig 2).

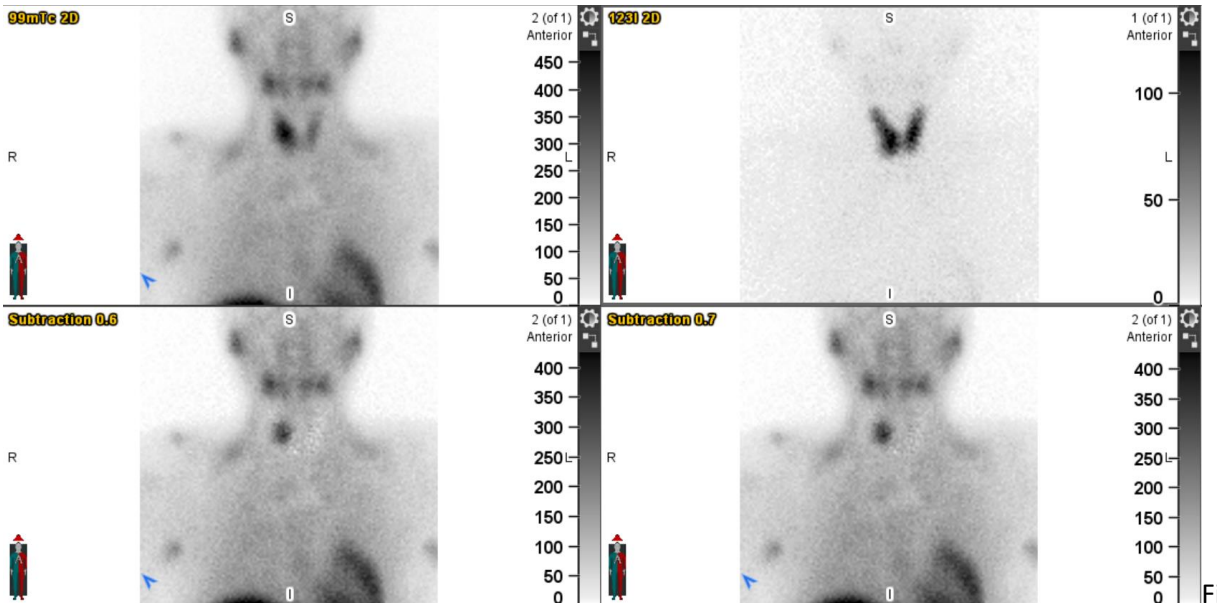

Fig. 2; Parathyroid scintigraphy. Left upper image: ^{99m}Tc-Sestamibi scan. Right upper image: ^{123}I scan. Lower images: subtraction.

Remarkably, a slightly increased ^{99m}Tc-Sestamibi uptake was also noticed in the right shoulder region.
Additional SPECT/CT images revealed this uptake to be an osteolytic bone lesion lateral in the right clavicle (Fig. 3).
Moreover, other smaller osteolytic lesions were visualised.

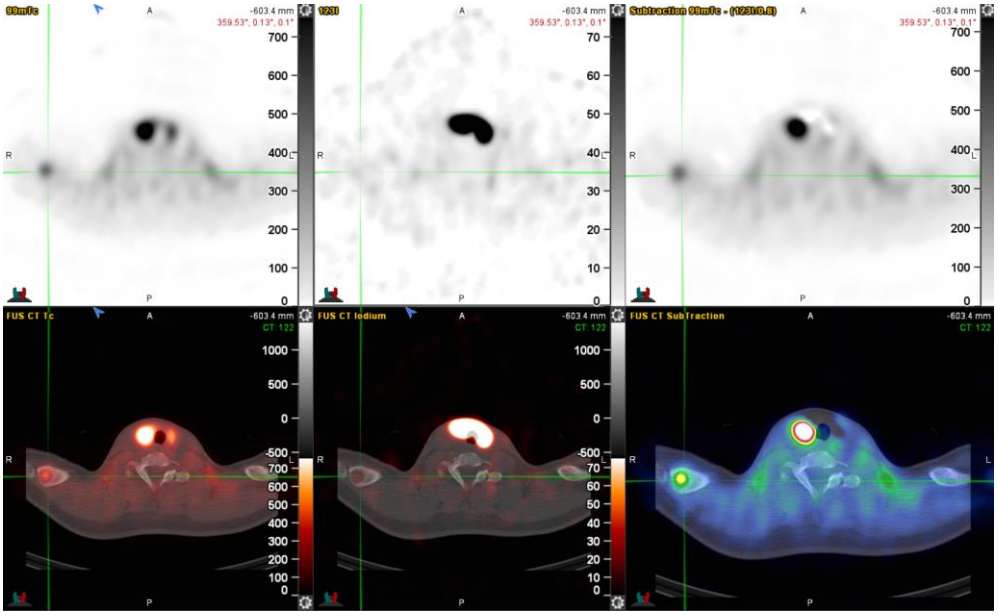

Fig. 3; Parathyroid scintigraphy showing ^{99m}Tc-Sestamibi uptake in the right clavicle, at a site of osteolysis.

The differential diagnosis for these osteolytic lesions included the possibility of a malignant process with metastases, originating from the parathyroid gland (e.g. parathyroid carcinoma) or another primary tumour (e.g. multiple myeloma, Langerhans cell histiocytosis).

However, in this case, considering the young age and the severity of the hyperparathyroidism, the preferred diagnosis was a parathyroid adenoma with secondary brown tumours.

Brown tumours are a benign complication of long-standing hyperparathyroidism. The increased levels of PTH have a direct effect on the bone by stimulating osteoclast activity, resulting in bone resorption. This process leads to the release of calcium from the bone, leading to hypercalcemia. Over time, these high levels of PTH can cause bone demineralization, which may manifest as osteopenia, osteoporosis, or in more severe cases, the formation of osteolytic lesions called brown tumours. Brown tumours are non-malignant, but they can cause significant skeletal deformities if left untreated. (1) Their vascular nature contributes to the increased ^{99m}Tc-Sestamibi uptake and they are most commonly found in the long bones, ribs, and clavicles.

Further investigation revealed bilateral medullary nephrocalcinosis on renal ultrasound, explaining the renal function decrease. Following this diagnosis of primary hyperparathyroidism complicated by nephrocalcinosis and probable brown tumours, the patient underwent parathyroidectomy. Histopathology confirmed a benign parathyroid adenoma.
Post-operatively, calcium levels normalised. The arterial hypertension, the initial cause of presentation, also normalised after surgery, suggesting it was probably secondary to the hypercalcemia (pheochromocytoma screening was negative and renal artery stenosis was excluded with ultrasound).

The patient was started on calcium supplementation to prevent hungry bone syndrome, a condition in which bones rapidly absorb calcium after the removal of hyperparathyroidism. Additionally, vitamin D supplementation was continued. Because of her young age and probable longstanding hyperparathyroidism, genetic screening was initiated (still pending).

This case illustrates the essential role of parathyroid scintigraphy, not only in identifying and localizing the underlying parathyroid pathology, but also in evaluating associated complications, such as osteolytic bone lesions (brown tumours).

Other nuclear imaging modalities have been described in the assessment of brown tumours. A systematic review covering 392 brown tumour lesions found that [^{18}F]fluorocholine PET/CT was the most effective in the detection of these tumours (2). Other modalities, such as [^{18}F]FDG PET/CT, [^{18}F]-sodium fluoride PET/CT, and bone scans, also show significant uptake but can be misleading, as they may mimic metastatic cancer spread (2). Given their ability to mimic secondary bone cancer, brown tumours should always be considered in the differential diagnosis of osteolytic bone lesions, especially in patients with known or suspected hyperparathyroidism.

1. Can Ö, Boynueğri B, Gökçe AM, Özdemir E, Ferhatoğlu F, Canbakan M, Şahin GM, Titiz Mİ, Apaydın S. Brown Tumors: A Case Report and Review of the Literature. Case Rep Nephrol Dial. 2016 Mar 18;6(1):46-52. doi: 10.1159/000444703. PMID: 27066494; PMCID: PMC4821153.
2. Jacquet-Francillon N, Prevot N. Brown tumors in nuclear medicine: a systematic review. Ann Nucl Med. 2023 May;37(5):255-270. doi: 10.1007/s12149-023-01832-1. Epub 2023 Mar 18. PMID: 36933117.

Radiopharmacy Track

DEVELOPMENT OF [89ZR]ZR-DFOSTAR-BELANTAMAB IMMUNOPET FOR THE SENSITIVE DETECTION OF MULTIPLE MYELOMA TUMOR BURDEN.

Noémie Mourot[1,2], Sébastien Anguille[2], Tim Van den Wyngaert[1], Filipe Elvas[1]

[1] *Molecular Imaging and Radiology (MIRA), University of Antwerp, Wilrijk, Belgium*

[2] *Laboratory of Experimental Hematology, University of Antwerp, Wilrijk, Belgium*

Aims

Multiple myeloma (MM) is an incurable haematological malignancy involving the abnormal proliferation of plasma cells within the bone marrow (BM). Despite considerable advances in treatment, patients still relapse, indicating the presence of residual disease below the level of detection. The B-cell maturation antigen (BCMA) is a transmembrane glycoprotein involved in the proliferation and maturation of plasma cells. Importantly, BCMA is selectively expressed on the surface of malignant plasma cells in most MM cases, supporting its potential as an imaging target. We aimed to develop an anti-BCMA ImmunoPET imaging strategy to visualize the expression of BCMA in MM.

Methods

We designed a novel radioimmunoconjugate based on belantamab (anti-BCMA antibody, GSK2857914). This antibody was first conjugated at 4-fold molar excess to the bifunctional chelator DFO* (DFO*-pPhe-NCS). The degree of conjugation of the bioconjugate was assessed by Reverse phase Liquid Chromatography-Mass Spectrometry (RPLC-MS) and its affinity was evaluated by indirect ELISA. Subsequently, the Ab-conjugate was radiolabelled with ^{89}Zr and purified, as reported previously by Dewulf et al. (2021). Quality control was performed by size exclusion chromatography-high performance liquid chromatography (SEC-HPLC) and instant thin-layer chromatography (iTLC) using 50mM DTPA and 20mM citric acid/acetonitrile (9:1, v/v) solutions. The radioimmunoconjugate was further characterized in vitro using BCMA-transduced K562 and wild-type K562 (for nonspecific binding) cells to determine the binding affinity and internalization kinetics. BCMA expression and binding of bioconjugates were assessed by cell surface staining using Fluorescence Activated Cell Sorting (FACS).
The targeting potential and the tissue distribution of the radiotracer were then assessed using a MM xenograft model. For this purpose, CB17 SCID mice (CB17/Icr-Prkdcscid/IcrIcoCrl) were subcutaneously inoculated with the K562 BCMA-transduced cell line (CB17 SCID K562 BCMA+). K562 wild-type cell line was inoculated to generate a negative control group (CB17 SCID K562 WT). Once the tumors were palpable and reached a volume of 100-200mm^3, mice received 3.7µCi/µg of [^{89}Zr]Zr-DFO*-Belantamab and underwent a PET/CT scan at day 3 and 5 post-injection (p.i). Four CB17 SCID K562 BCMA + tumor-bearing mice received a pre-infusion of 100-fold excess of cold belantamab one hour prior to the tracer injection.

Results

The conjugation of DFO* (4-fold excess) with belantamab was successful with up to 3 DFO* chelators per antibody. The average chelator-to-antibody ratio was 0.69. The bioconjugate showed a high affinity for human BCMA (hBCMA) with a preserved affinity compared to the native belantamab (Dissociation constant (Kd)~ 0.53 ± 0.01 vs 0.28 ± 0.02 nM). [^{89}Zr]Zr-DFO*-Belantamab was obtained with a non-decay corrected radiochemical yield of 90%,

>95% radiochemical purity and 186.1 ± 26.5 MBq/mg (n=6) specific activity. The radiotracer remained stable in formulaion buffer over 7 days with a radiochemical purity >80%. FACS results confirmed BCMA expression and binding of the immunoconjugate on K562 BCMA+ cells. In vitro assays demonstrated good affinity (Kd = 4.01 ± 0.63 nM) and slow internalization kinetics of [^{89}Zr]Zr-DFO*-Belantamab in BCMA+ K562 cells, with a maximum internalized fraction at 72 hours (16.5 ± 0.1 % cell associated activity/10^6 of cells) (Figure 1). At day 3 and 5 p.i., CB17 SCID K562-BCMA+ mice showed a high tumor uptake on PET/CT scan. However, we observed a background in nonspecific organs such as the spleen, joints (knees, hips and shoulders), heart and liver. Minimal tumor uptake was observed for blocking and wild-type control groups, confirming the specificity of the radiotracer for BCMA. While the nonspecific uptake observed in the BCMA+ group decreased using a pre-infusion of cold belantamab, the background uptake in healthy organs increased in the wild-type group (Figure 2).

Conclusion

[^{89}Zr]Zr-DFO*-Belantamab was successfully produced and showed favorable *in vitro* stability and binding affinity, supporting further validation as a potential novel immunoPET imaging agent of BCMA expression in *in vivo* studies. The *in vivo* results were associated with high tumor retention in BCMA-positive tumors. However, it is associated with a nonspecific uptake in organs such as the spleen, liver and heart.

Acknowledgement

This project is funded by the Research Fundation Flanders (FWO). Project : G024623N.

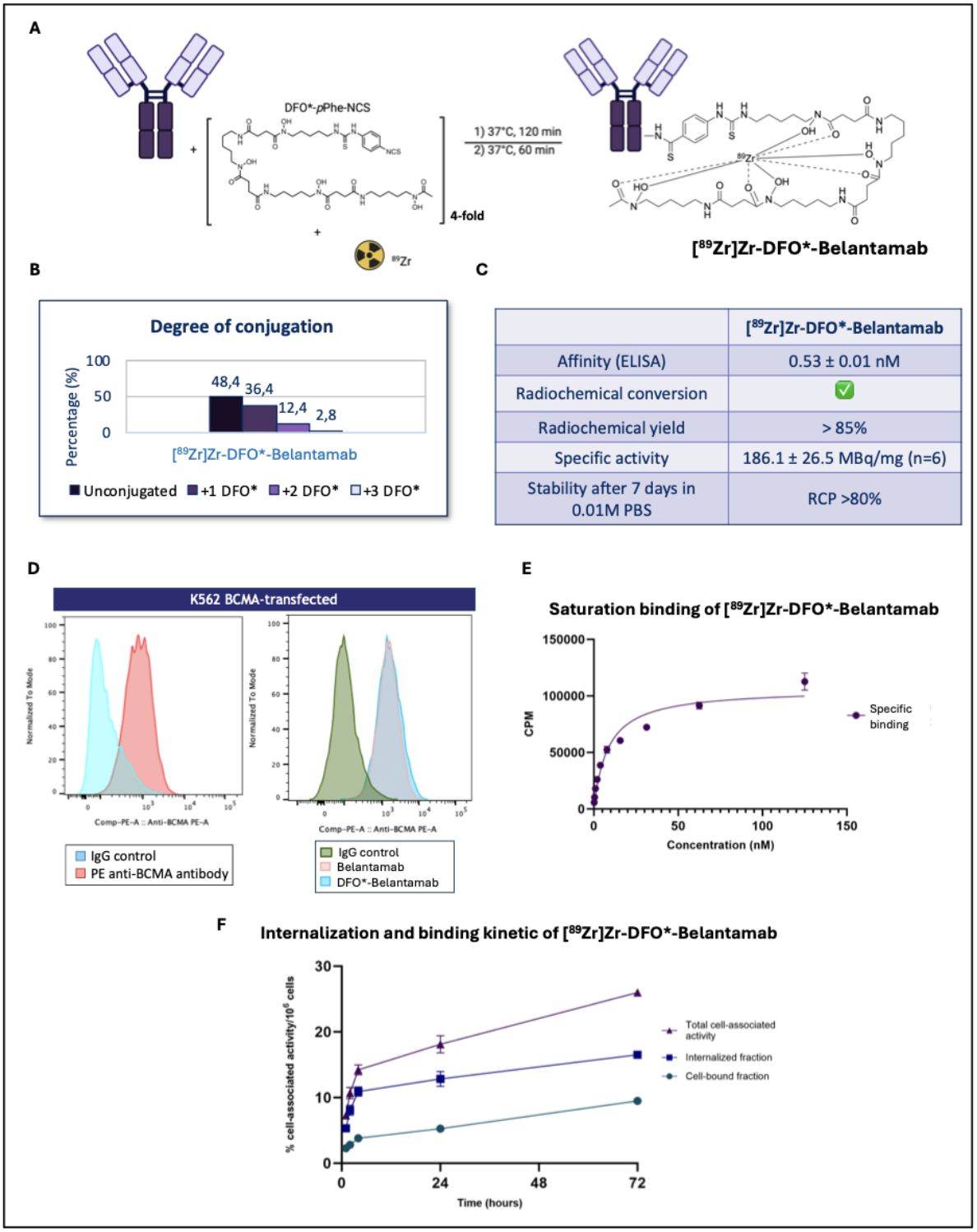

Figure 1. In vitro characterization of [^{89}Zr]Zr-DFO*-Belantamab construct. (A) Design and synthesis of the radioimmunoconjugate. (B) MS measurement results show the degree of conjugation of [^{89}Zr]Zr-DFO*-Belantamab. (C) Summary of ELISA results of DFO*-Belantamab immunoconjugate and radiolabelling efficiency of [^{89}Zr]Zr-DFO*-Belantamab. (D) Fluorescent Activated Cell Sorting (FACS) results show the BCMA expression of K562

BCMA-transduced cell line and the binding of conjugated and unconjugated Belantamab to K562 BCMA-transduced cells. (E) Saturation binding assay of [^{89}Zr]Zr-DFO*-Belantamab using K562 BCMA+ cell line and K562 WT cell line (for nonspecific binding). (F) Internalization of [^{89}Zr]Zr-DFO*-Belantamab using K562 BCMA+ cell line.

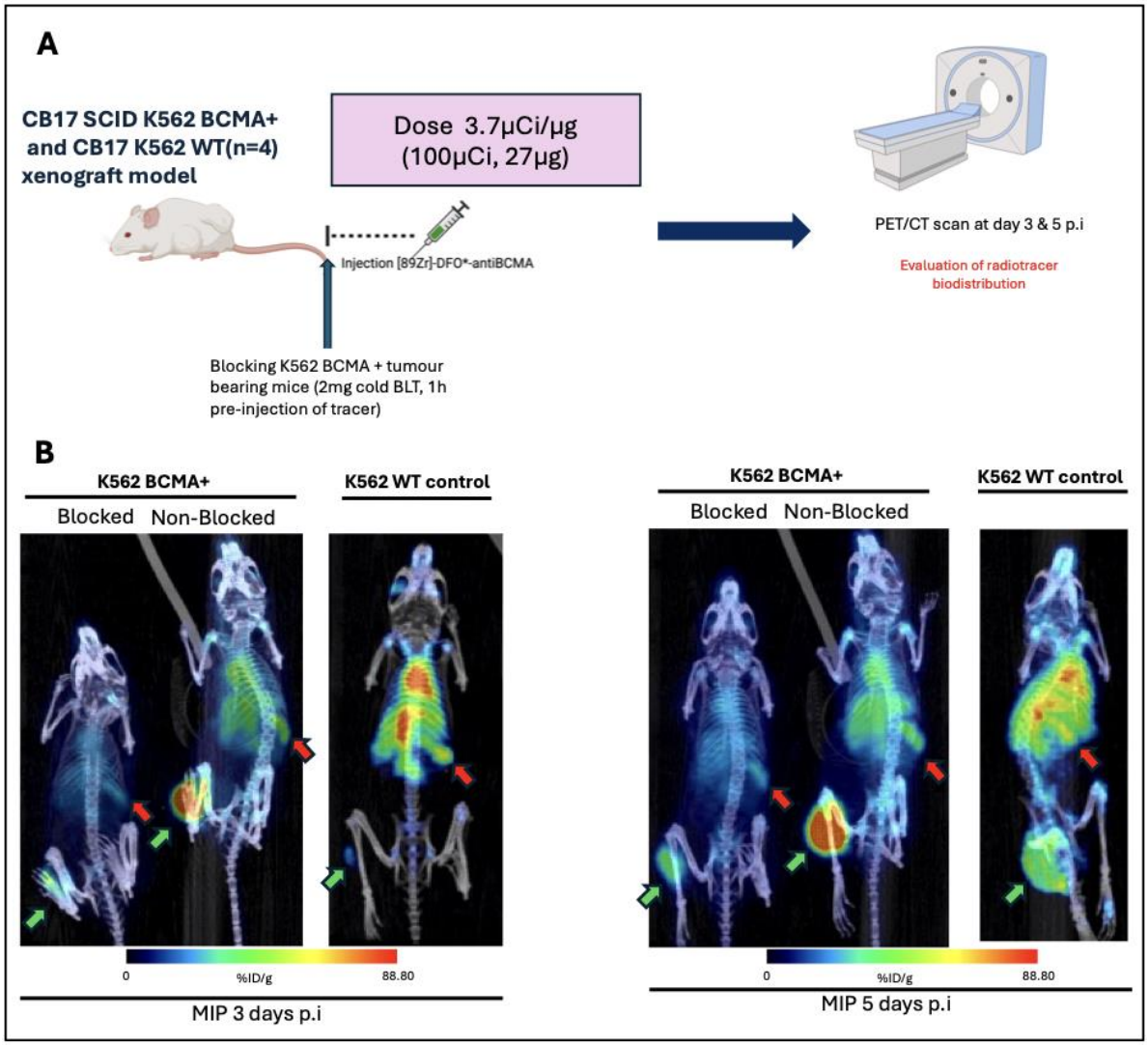

Figure 2. In vivo characterization of [^{89}Zr]Zr-DFO*-Belantamab construct. (A) Schematic representation of ImmunoPET imaging of MM xenograft model using [^{89}Zr]Zr-DFO*-Belantamab radiotracer. (B) PET/CT imaging of CB17 SCID K562 BCMA+ tumor-bearing mice and CB17 SCID K562 WT tumor-bearing mice at day 3 (left images) and 5 (right images) p.i. The coronal maximum intensity projection (MIP) images showed a clear delineation of the tumor for the BCMA-positive model. Minimal uptake within the tumor was observed for the blocking and BCMA-negative control group. The nonspecific uptake in the heart, liver and spleen is limited by the blocking. Tumor is indicated by the green arrows. The spleen is indicated with the red arrows.

DEVELOPMENT OF A NOVEL PRE-TARGETING STRATEGY FOR THE IMAGING OF 18F-LABELLED CAR T CELLS IN VIVO

Louis Lauwerys,[1], Donovan Flumens,[2], Max De Bisschop,[1], Christel Vangestel,[1], Karuna Adhikari,[1], Pieter Van Der Veken,[3], Eva Lion,[2], Filipe Elvas,[1]

[1] University of Antwerp; Molecular Imaging and Radiology (Mira), [2] University of Antwerp; Laboratory of Experimental Hematology (Leh), [3] University of Antwerp; Laboratory of Medicinal Chemistry (Uamc)

Aims

CAR T cell therapies have demonstrated promising results for the treatment of haematological cancers, with multiple FDA-approved CD19- and BCMA-targeting cell therapies. However, not all patients respond to therapy and severe toxicities, such as the cytokine release syndrome, can occur. Furthermore, there is a need to assess the biodistribution of CAR T cells and changes in functional state after infusion. Therefore, it is important to develop novel tools that allow early therapy response evaluation of CAR T cells. Molecular imaging of CAR T cells could provide important insights on therapeutic effectiveness earlier than currently possible and provide information on the longitudinal distribution and functional state of CAR T cells after patient infusion.

Methods

In this study, azido-modified monosaccharides were integrated in the glycan of T cells followed by strain-promoted alkyne-azide cycloaddition (SPAAC) with an ^{18}F-labelled counterpart ([^{18}F]DBCO[1] (Figure 1A)). Radiofluorination of [^{18}F]DBCO was performed by nucleophilic substitution of the tosylated precursor. The partition coefficient (LogD) was measured using the 'shake-flask' method (N=3). The *in vitro* stability of [^{18}F]DBCO was evaluated in formulation (N=1) and mouse plasma (N=3) by HPLC. Tracer biodistribution and metabolic stability were assessed in CD1 nude mice (N=4). Isolated T cells were incubated with 25 µM of a per-acetylated azido-containing monosaccharide (Ac_4GlcNAz, Ac_4ManNAz or Ac_4GalNAz) for 48 hours. After washing and resuspending the T cells, 5 µCi [^{18}F]DBCO (5.4 pmol) or 10 nmol DBCO-Cy5 were added for 1 h before measuring cell-associated radioactivity or evaluating cell fluorescence by flow cytometry, respectively. Lentiviral transduced CD19-CAR T cells from a single donor were acquired and characterized by flow cytometry. CAR T cells were incubated with 25 µM Ac_4ManNAz for 48 h, washed and resuspended in 10 nmol DBCO-Cy5 followed by flow cytometry analysis.

Results

[^{18}F]DBCO was prepared with a decay-corrected radiochemical yield of 7.71 ±3.55%, a radiochemical purity of 95.76 ±2.35% and a molar activity of 85.21 ±53.97 GBq/µmol (N=19). A LogD of 1.40 ±0.014 was measured. The tracer showed good stability in formulation for up to 2 hours, however, a faster degradation was observed in mouse plasma with 63.0 ±2.0% remaining after 2 hours. After 15 minutes *in vivo*, a smaller amount of radiotracer remained intact in vivo, 15 min after injection (28.6 ±14.9% intact tracer). [^{18}F]DBCO showed slow distribution from the blood to other organs, a high activity in organs in the thorax and abdomen (lungs, liver and intestines) and a mixed renal-hepatobiliary excretion (Figure 1B,C). DBCO-Cy5 labelling of T cells incubated with and without Ac_4ManNAz resulted in a mean fluorescence intensity (MFI) of 9127 ±6920 and 342 ±224, respectively (Figure 1D) (p= 0.0159, N=5). [^{18}F]DBCO-labelling of T cells incubated with or without Ac_4ManNAz resulted in a cell associated activity of 1.41 ±0.63 %added activity(AA)/1 x10^6 cells and 0.70 ±0.19 %AA/1 x10^6, respectively (Figure 1E)(p=0.1143, N=4). DBCO-Cy5 labelling of the CD19-CAR T cells (71.3% CAR expression, 2.84 ±0.36% $CD4^+$, 94.8 ±1.40 % $CD8^+$)

incubated with or without Ac_4ManNAz resulted in a mean fluorescence of 18974.33 ±817 .30 and 980.33 ±216.31, respectively.

Conclusions

After incubation with Ac_4ManNAz, T cells could be labelled with [^{18}F]DBCO and DBCO-Cy5 *in vitro*. [^{18}F]DBCO shows moderate stability *in vitro* and *in vivo* and a mixed renal-hepatobiliary clearance. The metabolic labelling strategy was successfully translated to CD19-CAR T cells *in vitro*. Future work will consist of validating the concept of labelling CD19-CAR T cells for in an *in vivo* tumour model, making this the first bioorthogonal ^{18}F-metabolic labelling strategy for CAR T cell therapy imaging *in vivo*.

References

1 Kettenbach et al., *Med. Chem. Commun.,* 2016,7, 654-657.

Acknowledgements

This research was funded by University of Antwerp BOF-DOCPRO4 (46060), and a FWO post-doctoral grant (12T8821N). The CD19 CAR T cells were kindly provided by Dr. Eduardo Laborda from Calibr at Scripps Research (USA).

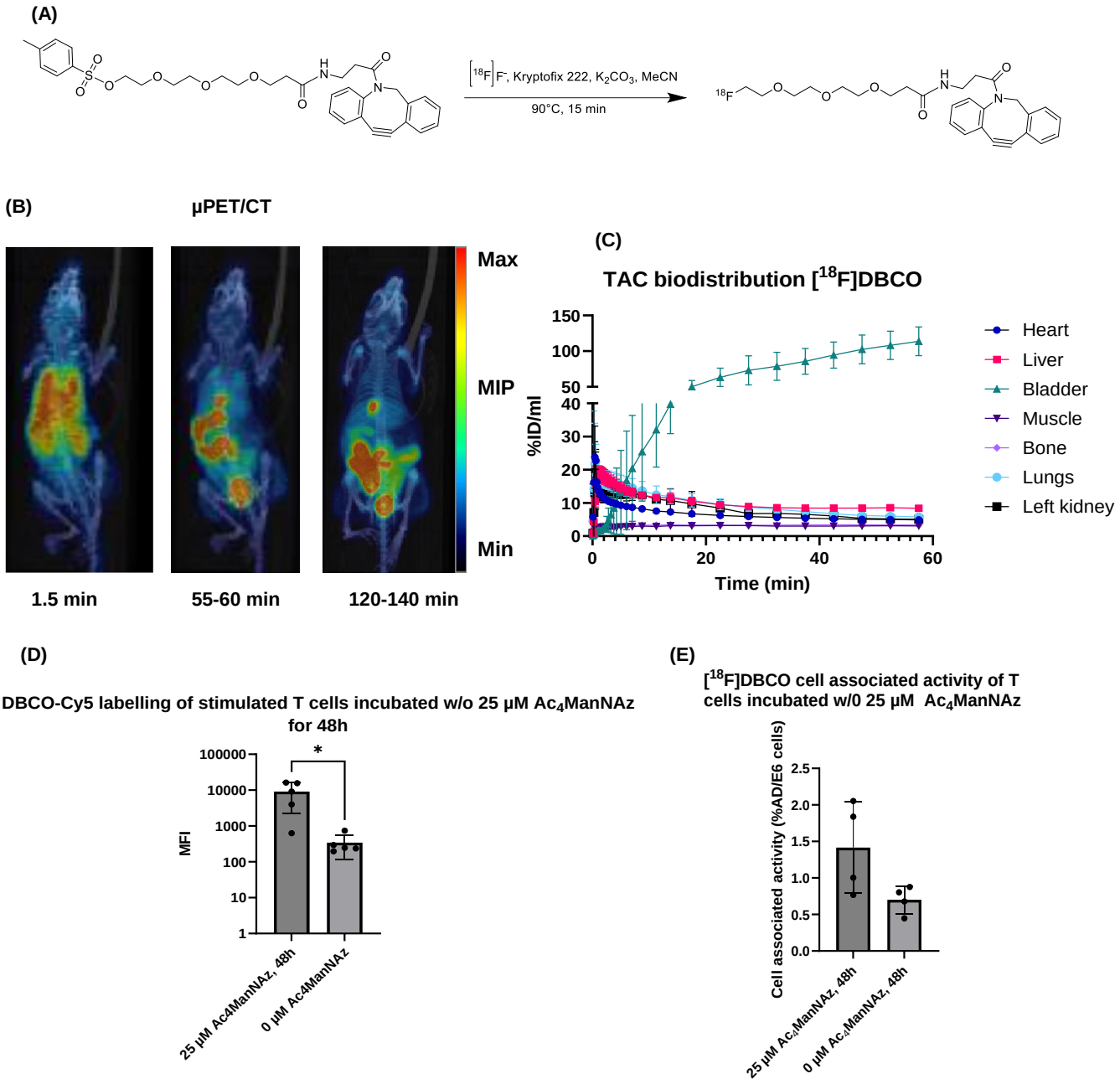

Figure 3 Radiosynthesis of [18F]DBCO (A). Mean intensity projection (MIP) and time activity-curves TAC of [18F]DBCO in CD1 nude mice. C,D). MFI values of DBCO-Cy5 labelled T cells pre-incubated with or without 25 µM Ac4ManNAz for 48 h (D). Cell-associated activity of [18F]DBCO-labelled T cells pre-incubated with or without 25 µM Ac4ManNAz for 48 h (E).

INDEPENDENT VERIFICATION OF ACTIVITY DETERMINATION FOR RADIOPHARMACEUTICAL PREPARATIONS IN NUCLEAR MEDICINE

Kristof Baete,[1], Liviu-Cristian Mihailescu,[2], Wies Deckers,[1], Christelle Terwinghe,[1], Raf Aarts,[2], Wies Claeys,[3], Janke Kleynhans,[4], Christophe Deroose,[1]

[1] Uz Leuven; Nuclear Medicine, [2] Belgian Nuclear Research Centre (Sck Cen), [3] Nuclear Medicine and Molecular Imaging, Ku Leuven; Department of Imaging and Pathology, [4] Radiopharmaceutical Research, Ku Leuven; Department of Pharmaceutical and Pharmacological Sciences

Aims

The use of radionuclides for therapy applications in nuclear medicine (NM) is increasing very rapidly. Hospitals require dedicated equipment for the preparation, determination of activity, dispensing, and administration of radionuclides for therapeutic use. The traceability and the accuracy of the measured activities are of course very important in clinical routine, for the diagnosis and planning of radionuclide therapies, and for treatment optimization. Unfortunately, the manufacturers of activity meters that are part of this dedicated equipment do not provide much information that is necessary to assess the accuracy and traceability of the activity determination. This is a legal requirement and needs to be verified independently as part of medical physics acceptance testing, quality assurance and control procedures.

The NM department of UZ Leuven installed a shielded isolator for the synthesis and dispensing of diagnostic and therapeutic radiopharmaceuticals (Phaedra Combo, Comecer S.p.A., Italy). After the installation, we verified the accuracy and calibration settings of the built-in activity meters for some specific radionuclides and using some recipients.

Methods

The shielded isolator contains two activity meters: a re-entrant well-type ionization chamber (VIK-202, Comecer), which is intended for the measurement of recipients during radiopharmaceutical preparation, and a pass-through chamber (DVK-103, Comecer), which is intended for the final measurement of the activity in a vial with the prepared radiopharmaceutical.

We verified the accuracy of both activity meters using traceable encapsulated reference sources, such as ^{57}Co, ^{60}Co, ^{133}Ba, and ^{137}Cs. The response of the activity meters was compared to other devices at the NM department using ^{99m}Tc. We assessed the energy response of the ionisation chambers for a variety of calibration settings using the aforementioned reference sources and compared that to other comparable ionisation chambers.

Subsequently, the Fidelis secondary standard radionuclide calibrator, provided by the Laboratory for Nuclear Calibrations (LNK) of the Belgian Nuclear Research Centre (SCK CEN), was involved for the calibration and verification of the activity meters when using 68Ga, 89Zr, and 177Lu. A standardized source geometry was used to relate the measurements to an activity determination that is traceable to a designated metrological institute.

Results

Initial acceptance testing of the activity meters showed reassuring results for the re-entrant well-type ionization chamber VIK-202. However, the pass-through chamber DVK-103 showed a deviation of about 18% for the accuracy when using a ^{57}Co reference source. It appeared that the recipient holder of the activity meter, and its automated positioning system, was not taken into account when the device was calibrated by the manufacturer. Hence, on site adjustment of the electrometer gain settings appeared to be necessary and required the determination of new calibration factors.

Subsequently, we were able to establish new calibration factors for 68Ga, 89Zr, and 177Lu using the onsite availability of the Fidelis secondary standard radionuclide calibrator. The DVK-103 pass-through chamber demonstrated the need for additional calibration factor adjustments when using 177Lu with specific recipients. Moreover, the accuracy of the activity determination in this chamber showed to be highly influenced by the volume of the radiopharmaceutical solution in the recipient.

Conclusions

Traceable calibration of activity meters and independent verification of the accuracy of the activity determination shows to be very important in NM. We analysed the accuracy of the activity determination using a shielded isolator and required significant adjustments of the factory based calibration settings.

We explicitly recommend the involvement of a national metrological service for the independent verification of activity determination in NM applications.

References

Decristoforo, C., Hayashi, S. F., Bordeau, C., Haddad, F., Viertl, D., Deville, C., Naidoo, C., Pedersen, K. S., Jensen, M., Köster, U., Correia, J. G., Gano, L., Bruchertseifer, F., Baete, K., Mikolajczak, R., Collins, S., Geistlich, S., van der Meulen, N., Ponsard, B., … Campillos, M. (2022). *Standards for clinical translation*. Zenodo. https://doi.org/10.5281/zenodo.6599181

Cunha, L., Baete, K., Leijen, C., & Jamar, F. (2023). Main challenges in radiation protection with emerging radionuclide therapies. *The Quarterly Journal of Nuclear Medicine and Molecular Imaging*, *67*(1). https://doi.org/10.23736/S1824-4785.22.03502-6

Saldarriaga Vargas, C., Rodríguez Pérez, S., Baete, K., Pommé, S., Paepen, J., Van Ammel, R., & Struelens, L. (2018). Intercomparison of 99m Tc, 18 F and 111 In activity measurements with radionuclide calibrators in Belgian hospitals. *Physica Medica*, *45*, 134–142. https://doi.org/10.1016/j.ejmp.2017.12.011

IN-HOSPITAL PRODUCTION AND QUALITY CONTROL OF RADIOTRACER [68GA]GA-NODAGA-EXENDIN-4 ON TRASIS EASYONE SYNTHESIZER

Sonja Van den Block,[1], Julien Masset,[2], Charles Vriamont,[3], Sophie Bourgeois,[4], Vicky Caveliers,[5]

[1] Vrije Universiteit Brussel; Uz Brussel; Mith Research Group - Nuclear Medicine Department, [2] Trasis; Trasis, [3] Trasis, [4] Uz Brussel; Uz Brussel; Nuclear Medicine Department, [5] Uz Brussel; Uz Brussel; Department of Nuclear Medicine

Aims

[^{68}Ga]Ga-NODAGA-Exendin-4 is a promising radiopharmaceutical for positron emission tomography (PET) in pancreatic β-cell imaging to non-invasively detect, diagnose, and preoperatively localize insulinomas [1]. Exendin-4 is a peptide analogue of glucagon-like peptide-1 (GLP-1) and binds with similar affinity to the GLP-1 receptor which is highly expressed in human insulinomas. The synthesis protocol of [^{68}Ga]Ga-NODAGA-Exendin-4 was reported earlier [2] but in this work we aimed at synthesizing the radiotracer in an automated production process on a Trasis EasyOne synthesizer in a hospital-based radiopharmacy.

Methods

^{68}Ge/^{68}Ga generator Galli Eo^{TM} (IRE-Elit Radiopharma, Fleurus, Belgium) was used to produce the radionuclide, and was connected to the EasyOne synthesis module (Trasis SA, Ans, Belgium). The chemicals, reagents and consumables for the radiolabelling procedure were commercially provided as single use kits (Trasis SA, Ans, Belgium). EDTA-Tween solution was obtained from ABX advanced biochemical compounds (Radeberg, Germany). The GMP grade precursor peptide Lys40(NODAGA)-Exendin-4 (Acetate) was purchased from piCHEM GmbH (Raaba-Grambach, Austria). The radiolabelling was optimized using different incubation temperatures and times in combination with variable starting masses of the peptide. Quality control methods included visual inspection of the final product, determination of pH, radiochemical and radionuclide identity, radiochemical purity (RCP) by reverse phase high pressure liquid chromatography (RP-HPLC) and instant thin layer chromatography (iTLC), colloid detection by iTLC, bacterial endotoxins by limulus amebocyte lysate (LAL)-test, and filter integrity test. The ^{68}Germanium breakthrough of the generator was tested periodically. Sterility testing of the final product was done after conditional release, verifying the absence of microorganisms, essential for final release.

Results

The optimized automated synthesis of [^{68}Ga]Ga-NODAGA-Exendin-4 was performed with the following parameters: 10µg of precursor and incubation time of 15 minutes at 85°C. Acetate buffer was used during the labelling step, guaranteeing a stable pH while limiting the formation of ^{68}Ga-colloids. It resulted in a sterile final product >500MBq with a RCP >95%, comprising both oxidized and non-oxidized [^{68}Ga]Ga-NODAGA-Exendin-4, as the oxidized form of the tracer does not impact its quality [3,4]. Results show an apparent molar activity >250GBq/µmol and a decay corrected (DC) overall radiochemical yield (RCY) of 81,6±3,8% (n=3). Three validation batches confirmed both the robustness of the synthesis process and the reproducibility in production yield and quality of the radiotracer.

Conclusions

[^{68}Ga]Ga-NODAGA-Exendin-4 was successfully synthesized on a Trasis EasyOne using the IRE ^{68}Ge/^{68}Ga generator Galli Eo^{TM,} making the radiopharmaceutical available to a broader community. It can be used for application in clinical settings, routine productions, and translation to a GMP facility for further use in clinical trials.

References

1. Boss M, Buitinga M, Jansen TJP, Brom M, Visser EP, Gotthardt M. PET-based human dosimetry of 68Ga-NODAGA-exendin-4, a tracer for β-cell imaging. Journal of Nuclear Medicine. 2020 Jan 1;61(1):112–6.

2. Tokgöz S, Boss M, Prasad S, Shah P, Laverman P, van Riel M, et al. Protocol for Clinical GLP-1 Receptor PET/CT Imaging with [68Ga]Ga-NODAGA-Exendin-4. In: Methods in Molecular Biology. Humana Press Inc.; 2023. p. 143–53.

3. Janota B, Karczmarczyk U, Laszuk E, Garnuszek P, Mikołajczak R. Oxidation of methionine - Is it limiting the diagnostic properties of 99mTc-labeled exendin-4, a glucagon-like peptide-1 receptor agonist? Nuclear Medicine Review. 2016 Jul 29;19(2):104–10.

4. Jodal A, Lankat-Buttgereit B, Brom M, Schibli R, Béhé M. A comparison of three 67/68Ga-labelled exendin-4 derivatives for β-cell imaging on the GLP-1 receptor: the influence of the conjugation site of NODAGA as chelator. EJNMMI Res. 2014 Jun 22;4(1):1–10.

DEVELOPING A THERANOSTIC CU-64/CU-67 PRETARGETING STRATEGY FOR CD70 EXPRESSING SOLID TUMORS

Quanyi Yu,[1], Karuna Adhikari,[1], Filipe Elvas,[2], Tim Van den Wyngaert,[3]

[1] University of Antwerp; Molecular Imaging and Radiology (Mira), [2] University of Antwerp; Antwerp University Hospital; Molecular Imaging Center Antwerp, [3] Antwerp University Hospital; Nuclear Medicine

Aims: A radiotheranostic approach using monoclonal antibodies (mAbs) provides an attractive strategy to target tumor-associated antigens. Pretargeting strategies utilizing bioorthogonal inverse electron-demand Diels-Alder (IEDDA) reaction can overcome the high radiation exposure associated with this technique. However, since most targets, like CD70, undergo intracellular internalisation upon binding, which reduces the availability of bioorthogonal tags, hindering effective radioligand accumulation in tumors. To address this, we aim to develop cell-permeable trans-cyclooctenes (TCOs) labeled with the theranostic pair Cu-64/Cu-67, to efficient reaction with mAb-conjugated tetrazines both extra- and intracellularly in a model of CD70-expressing tumor, enabling precise and effective radio-payload delivery with minimal systemic exposure.
Methods: The TCOs were synthesized using a previously reported procedure [1], followed by conjugation with linkers displaying different lipophilicity (alkyl chain and polyethylene glycol (PEG) chain) and the macrocyclic chelator, NOTA, to yield precursors (CREANT-201 and CREANT-202) which are relatively small, stable, charge-neutral after complexed with Cu-64/Cu-67. The radiolabelling conditions were optimized with Cu-67, focusing on parameters including stoichiometry, incubation time and temperature, to achieve maximal labeling efficiency. Radiochemical conversions (RCC) were determined by radio-thin-layer chromatography (radio-TLC), while radiochemical purity (RCP) was assessed via radio-high-performance liquid chromatography (radio-HPLC). Radiolabelled compounds were further evaluated regarding *in vitro* stability towards *cis* isomerization (in PBS buffer up to 4h), and reacted with a Bis(pyridin-2-yl)-1,2,4,5-tetrazine (Bispyr-Tz) to confirm their reactivity.
Results: CREANT-201 and CREANT-202 were labelled with Cu-67 under optimized condition by incubation with 0.2M ammonium acetate buffer, pH 5.5 at room temperature for 15 min (Fig. 1). The RCC and RCP were over 95% for both [^{67}Cu]Cu-CREANT-201 and [^{67}Cu]Cu-CREANT-202. The logD values for two tracers were determined to be -1.75 $\pm$ 0.11 and -2.45 $\pm$ 0.03, respectively, revealing that [^{67}Cu]Cu-CREANT-202 which contains a PEG moiety, exhibits greater hydrophilicity. After the reaction with a Bispyr-Tz, a new radioactive peak corresponding to the dihydropyridazine reaction product could be observed, which indicates the radiolabelled-TCOs preserved the reactivity towards Tz (Fig. 1). Tracers showed good stability in PBS without copper release. Isomerization from *trans* to *cis* was observed after 2h with 72% of *trans*-isomer remaining.

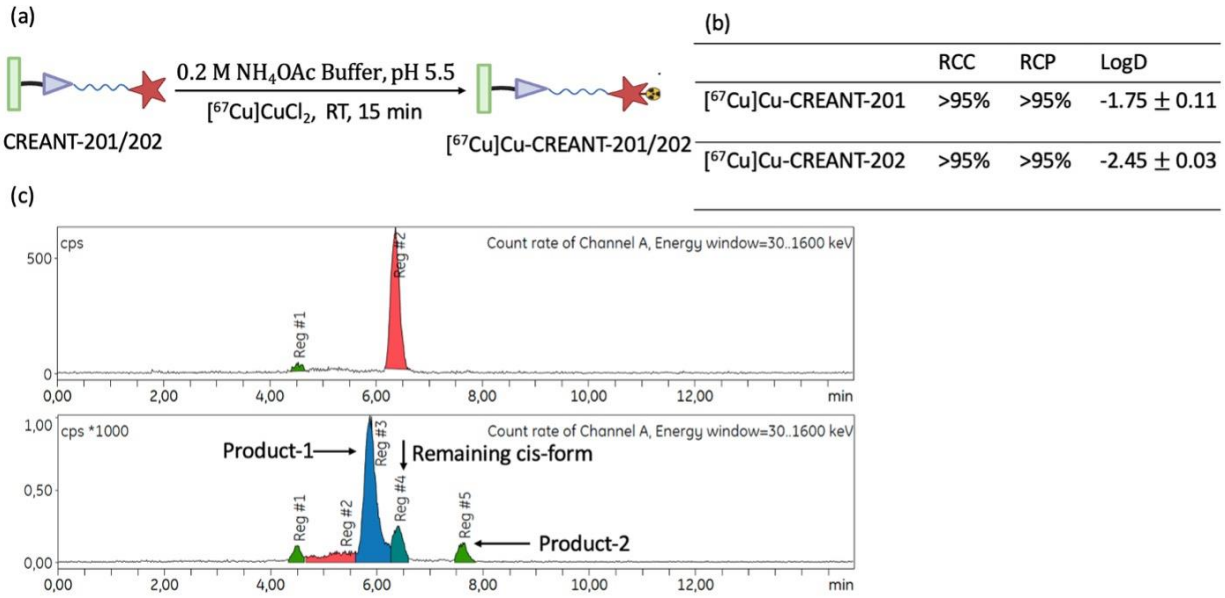

	RCC	RCP	LogD
[67Cu]Cu-CREANT-201	>95%	>95%	-1.75 ± 0.11
[67Cu]Cu-CREANT-202	>95%	>95%	-2.45 ± 0.03

Figure 1. The radiolabeling of CREANT-201/202 with Cu-67 (a) The radiolabeling scheme with [^{67}Cu]CuCl$_2$; (b) The labeling result of [^{67}Cu[Cu-CREANT-201/202; (c) The radio-chromatogram of [^{67}Cu]Cu-CREANT-202 top: before the addition of Bispyr-Tz bottom: after the addition of Bispyr-tz

Conclusions: The TCOs can be radiolabelled with Cu-67 with high efficiency and preserved reactivity. [^{67}Cu]Cu-TCO is promising for pretargeted therapy using tetrazine-conjugated mAbs. These copper-labelled ligands will be further evaluated *in vitro* with CD-70 positive cells and *in vivo* with CD-70 expressing tumor-bearing mice via the pretargeting approach.

Reference:

1. Adhikari, K., et al., Characterization of Structurally Diverse 18F-Labeled d-TCO Derivatives as a PET Probe for Bioorthogonal Pretargeted Imaging. ACS Omega, 2023. **8**(41): p. 38252-38262.

ACTIVITY DETERMINATION OF TB-161 USING RADIONUCLIDE CALIBRATORS

Jason Noben,[1], Wies Deckers,[2], Janke Kleynhans,[3], Wies Claeys,[4], Matthijs Sevenois,[2], Christophe M. Deroose,[2], Kristof Baete,[2]

[1] Ku Leuven; Physics and Astronomy, [2] Uz Leuven; Nuclear Medicine, [3] Ku Leuven; Radiopharmaceutical Research, [4] Ku Leuven; Imaging and Pathology

Aims

In recent years, the treatment of patients in nuclear medicine using novel radionuclides formulated in targeted therapies injected intravenously has gained a lot of attention. Together with that, the need for quantitative imaging, treatment verification, and the clinical interest to assess treatment effectiveness has increased as well. At the root of these challenges lies the accuracy of the activity determination. There are legal provisions about the determination of administered activity to patients, for which the accuracy should be within acceptable ranges of the intended, prescribed activity. Inaccuracies could lead to treatment failures or adverse effects and should be avoided. But also the development and translation of new radiopharmaceuticals could be affected if the calibration of imaging equipment and activity measurement devices for preclinical research in theranostics would suffer from inaccurate activity determination. Eventually, this could lead to misinterpretations of dose-effect relationships, which is an important contribution of preclinical research to the preparation of clinical trials.

In this study, we investigated how well the activity of the novel radionuclide terbium-161 (Tb-161) could be measured using radionuclide calibrators together with a variety of recipients that are relevant for clinical and preclinical practice.

Methods

An amount of uniform Tb-161 solution (Tb^{3+} in aqueous 0.05 M HCl) was provided by SCK-CEN in standardized recipients (10R Schott vials containing 4 g of solution). The activity was accurately measured with the Fidelis secondary standard radionuclide calibrator of the Laboratory for Nuclear Calibrations (LNK) at SCK-CEN . The standardized source geometry was used to relate the measured activity to a designated metrological institute. First, the solution was used to obtain calibration factors for Tb-161 on 5 Capintec (CRC-55tR, CRC-15PET and CRC-15R) and 3 Comecer (VIK-202) radionuclide calibrators at UZ Leuven and KU Leuven. Subsequently, a part of the activity was put in a new 10R Schott vial, which will be referred to as the “master solution”. Mass based amounts of activity derived from the uniform master solution were used to measure the influence of recipients and source volume on the activity determination using activity meters.

The investigated recipients include three plastic containers—a 1.5 ml LoBind® Eppendorf tube (normally used for radiolabeling procedures), a 0.5 ml diabetic syringe (used to inject doses for preclinical studies), a 10 ml BD Luer-Lok™ syringe (for patient doses), as well as two glass vials, i.e. a 10R Schott and an SV-25A vial. These recipients were filled to at least two different volumes to observe the volumetric effects. For that, the master solution was diluted to achieve higher volumes. The Eppendorf was measured twice: once in a polystyrene holder and once without.

We investigated the effect of the dipper and also used two in-house manufactured dippers, made of polymethyl methacrylate (PMMA) and polycarbonate (PC): one with an indentation at the bottom to allow for the stability of the 10R Schott and one for the SV-25A.

The results were converted to the normalized deviation from the expected activities. The difference between manufacturers was assessed by subtracting the Comecer (VIK) deviations from the Capintec (CRC) deviations. The

difference between dippers was determined by comparing the deviations of the used in-house dipper with those of the original dippers.

Results

The resulting deviation ranges inferred from the data are shown in Table 1. An example of the visualization of the data are shown in Figures 1–2. Notably, the plastic recipients strayed further from the expected true activity than the glass ones. Similarly, the difference in response between the Comecer VIKs and the Capintec has a smaller absolute value for the glass vials than the plastic recipients. In most cases, the Capintec radionuclide calibrators overestimated the activity more than the VIK radionuclide calibrators. Additionally, the difference between the used dippers is the smallest for the 10 ml BD Luer-Lok.

Table 1: The maximum activity deviation ranges for the different recipients and volumes across all devices.

Recipient	**Deviation from expected [%]**	**Difference VIK & Capintec [%]**	**Difference Original & In-House Dipper [%]**
Eppendorf + Holder	14.2–20.9	0.7–5.0	-0.8–1.4
Eppendorf	11.9–16.7	-0.6–4.5	-1.8–1.7
Diabetic Syringe	18.9–28.7	4.3–8.7	-1.0–0.4
10 ml BD Luer-Lok	17.2–27.7	3.1–6.3	-0.25–0.25
10R Schott	-3.8–1.1	-1.1–2.6	1.5–2.5
SV-25A	-0.1–3.2	-1.1–2.6	-0.6–1.6

Discussion

The results indicate that the choice of recipient and to a lesser extent the volume have a large effect on the accuracy of the measured activity using radionuclide calibrators. The deviation from the expected activity for the vials being lower than for the syringe can be attributed to the difference of material with the former being made of glass and the latter being made of plastic. Particularly the low-energy X-rays (5.7–9.0 keV) resulting from the decay of Tb-161 may contribute significantly to this difference.

Furthermore, for Tb-161 the choice of dipper did not seem to impact the results in the case of the 10 ml BD Luer-Lok syringe. This was expected as most of the activity is positioned in the more sensitive zone of the dose calibrator and less of the particles travel through the dipper. Similarly, it was expected that the dipper does make a difference for the smaller syringe as the emission of Tb-161 might interact more with the plastic rod of the dipper. For vials and the Eppendorf, the dipper does have a minor impact on the measured activity which was also expected as these recipients are surrounded by the well of the dipper.

Lastly, the difference in response between Comecer and Capintec models might suggest that the electronics or internal wall thickness of the ionization chamber differ in such a way that this impacts the measurement results. Capintec seems to overestimate syringe activity more than Comecer compared to vials, indicating that various chambers can measure a significant different response for the positioning of the source. Further research will be needed to test this hypothesis.

Conclusion

In summary, when using Tb-161, special care must be taken to ensure that the measured activity matches the true activity when using radionuclide calibrators. Assuming a one size fits all calibration factor is an archaic approach that is not applicable to most newly applied exotic radionuclides and may lead to large errors (up to 29% deviations from the expected) when using a variety of recipients in the early stages of a study or treatment.

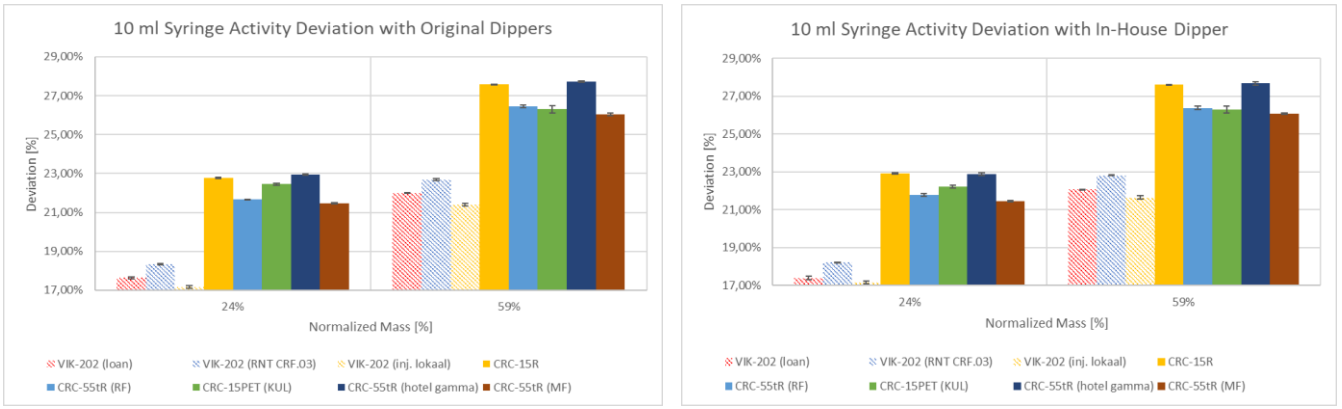

Figure 4: The deviation of the measured activity from the expected for a 10 ml BD Luer-Lok syringe with a BD Microlance 3™ Blue needle. The mass was normalized to the maximally recommended fill volume (10 ml).

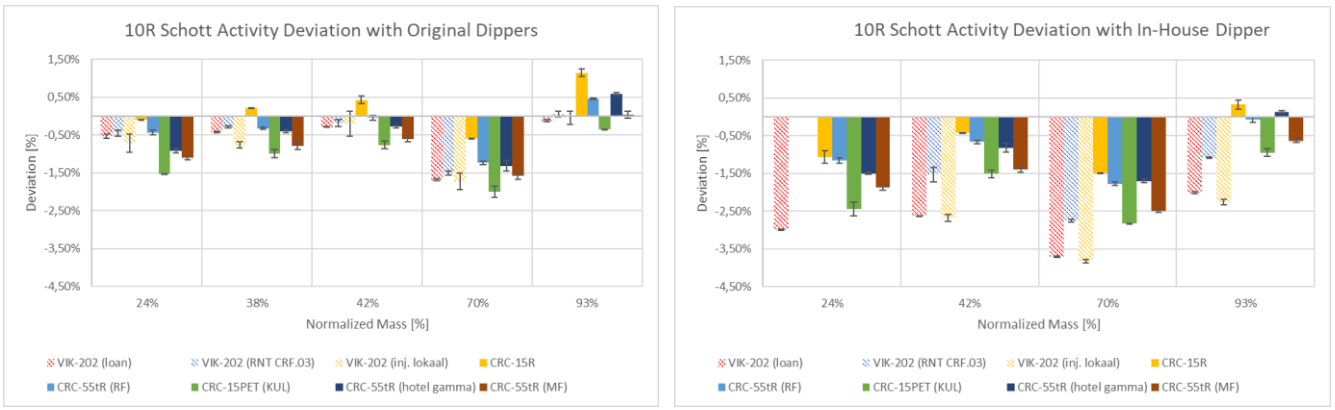

Figure 5: The deviation of the measured activity from the expected for a 10R Schott. The mass was normalized to the maximally recommended fill volume (10 ml).

Physics and Engineering Track

MONTE CARLO SIMULATION OF A LOW-COST TOTAL-BODY PET SCANNER DESIGN BASED ON FLAT-PANELS WITH MONOLITHIC DETECTORS

Elke Dhaenens,[1], Maya Abi Akl,[1], Boris Vervenne,[1], Jens Maebe,[1], Christian Vanhove,[1], Stefaan Vandenberghe,[1]

[1] *Medisip*

Aims

While PET provides the highest sensitivity among molecular imaging techniques, the sensitivity of current standard clinical PET scanners remains limited due to their short axial field of view (AFOV) of approximately 15-26 cm. This led to the development of long AFOV PET systems ranging from 70 cm to 195 cm, which have demonstrated sensitivity gains of 10-40 times compared to conventional systems [1]. These improvements enable lower radiation doses, reduced scan times, and/or enhanced signal-to-noise ratio. However, the widespread adoption of such systems is hindered by their high acquisition and maintenance costs, related to the high number of detector crystals, which scales proportionally with the AFOV. Operational challenges such as patient positioning and throughput limitations further complicate cost-effective implementation in the clinic.

Cost-effective LAFOV PET designs are being developed, aiming to expand clinical accessibility by reducing system cost and increasing patient throughput. The Walk-Through Total Body PET (WT-TB-PET) system that is studied and built at the MEDISIP group (Ghent University) replaces the traditional ring-based design with two large vertical panels of monolithic detectors positioned 50 cm apart. This configuration maintains a large solid angle, enhancing geometric sensitivity. Using monolithic LYSO detectors results in a high spatial resolution and depth of interaction capabilities. This setup eliminates bed positioning delays, significantly increasing efficiency and reducing cost per scan [2].

Building on this concept, this study proposes a novel cost-effective flat-panel system designed for high-throughput imaging: the **Slide-Through Total-Body PET (ST-TB-PET)** (see Figure 1). It consists of two narrow vertical panels that span the entire height of the patient with monolithic detectors. The ST-TB-PET employs a dynamic slide-through mechanism where the patient stands on a moving platform that gradually translates through the scanner. This approach maintains high geometric sensitivity while reducing the number of required detector elements, optimizing both performance and cost-efficiency. Additionally, by making the upper sections of the panels twice as wide as the lower sections, the design prioritizes image quality in the torso region, where detailed imaging is most clinically relevant but attenuation is high. While the reduced angular coverage may introduce elongation artifacts, the system's high throughput and reduced component cost are expected to make it a promising, cost-effective alternative for traditional TB-PET scanners.

This study aims to evaluate the performance of the ST-TB-PET through Monte Carlo simulations. The findings will contribute to developing a more accessible TB-PET solution, potentially improving global PET imaging availability while maintaining high diagnostic accuracy.

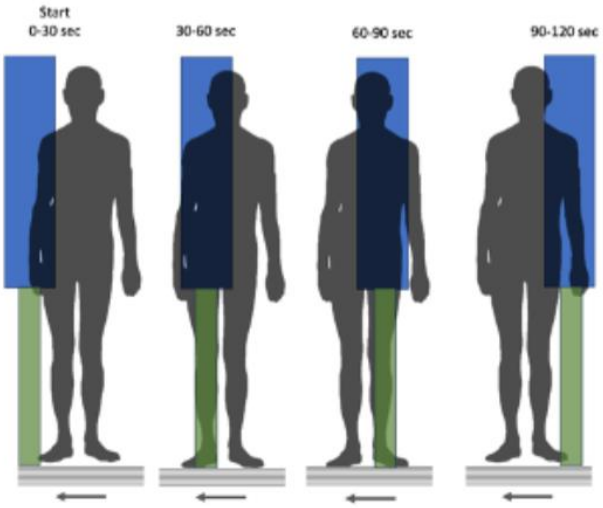

Figure 6: The ST-TB-PET with the patient on the platform moving relative to the panels to scan the torso and legs

Methods

This study evaluates the sensitivity and image quality of the ST-TB-PET, comparing it to two reference designs: a large flat-panel system (with 4.5 times more detectors, designed to cover the entire patient), and a cylindrical system (with the same total number of detectors as the ST-TB-PET). The large reference flat-panel system is included to study the impact of the narrow field of view of the ST-TB-PET on sensitivity and limited angle artifacts. The reference cylindrical system rearranges a similar number of detectors as the ST-TB-PET within a configuration resembling the Siemens Biograph Vision 600 [3]. All systems use monolithic LYSO detectors (50×50×16 mm^3) coupled to an 8×8 array of of 6×6 mm^2 SiPMs, offering 300 ps time-of-flight, 1.14 mm full-width-at-half-maximum (FWHM) 2D intrinsic spatial resolution, and 2.67 mm FWHM depth of interaction resolution [4]. The details of these scanners are shown in Table 1.

Table 2: overview of different PET scanner designs and specifications. Slide-Through Total-Body PET, Large reference flat-panel system, and Reference cylindrical system

	Slide-Through Total-Body PET	**Large reference flat-panel system**	**LIGHTING UP THE PATH TO RLT: A REMARKABLE PSMA-PET/CT CASE**

Scanner Designs	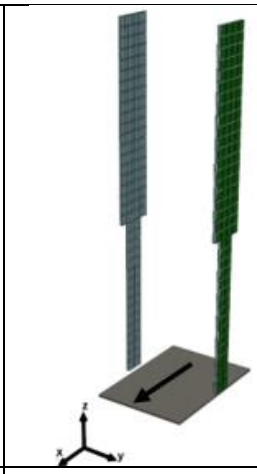	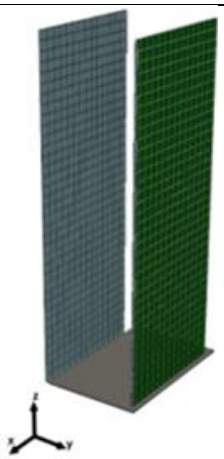	**Aster Marin,[1], Tim Van den Wyngaert,[2], Taco Cappenberg,[3], Sigrid Stroobants,[4]**
Crystal Count	224	1008	**[1] U Antwerpen, [2] Antwerp University Hospital; Nuclear Medicine, [3] Uz Antwerpen, [4] University Hospital Antwerp; University of Antwerp; Department of Nuclear Medicine**
Dimensions	Top section: 105.7×20.9 cm^2 Bottom section: 84.5×10.3 cm^2	Panel dimension: 190.5×73.9 cm^2	
Spacing between the panels	50 cm	50 cm	**Lighting Up the Path to RLT: a remarkable PSMA-PET/CT case**
Motion	The patient stands upright on a moving platform. The total lateral length covered with motion for the top section is 73.9 cm.	No motion	Aster Marin[1], Tim Van den Wyngaert[1], Taco Metelerkamp Cappenberg[1], Sigrid Stroobants[1]

Sensitivity and image quality evaluation

Sensitivity measurements were performed using line and cylindrical sources (1 MBq activity) of varying lengths. For the flat-panel systems, sources were positioned centrally between the panels along the system axis, while for the reference cylindrical system, they were placed along its central axis. A 70 cm line source was used to benchmark the reference cylindrical system against the NEMA sensitivity of the Biograph vision 600. The line source was positioned in the middle of the system and the system was kept stationary. A 190 cm source, which spans the full axial length of the systems, allows a comparison of the geometric coverage in stationary conditions for flat-panel systems. This was simulated for the ST-TB-PET and the large reference flat-panel system. A 70 cm cylindrical source was embedded in a 70 cm cylindrical water phantom with 20 cm diameter, to simulate attenuation. The phantom was positioned in the upper section of the ST-TB-PET, with its lower edge matching the lower edge of the bottom section, to study the torso region. This was simulated for the moving ST-TB-PET and the reference cylindrical system with phantom translation.

Finally, an anthropomorphic XCAT phantom (male with normal BMI) was simulated to assess image quality in a clinical scenario. The data was reconstructed using iterative MLEM (voxel size of 2×2×2 mm^3) as implemented in in-house software.

Results

Sensitivity

For the 70 cm line source, the reference cylindrical system exhibits a sensitivity of 13.6 cps/kBq, which is comparable to the Biograph Vision 600 (16.4 cps/kBq NEMA sensitivity [3]). A key difference between the systems is the detector type: the reference cylindrical system uses a monolithic scintillator with 16 mm thickness, while the Biograph Vision 600 utilizes pixelated scintillators with a thickness of 20 mm and has a slightly longer AFOV. These observations support and validate our Monte Carlo system model.

For the 190 cm line source, the large reference flat-panel system achieves a much higher sensitivity (162.0 cps/kBq) than the ST-TB-PET (43.8 cps/kBq), highlighting the increased geometric coverage of the large reference flat-panel system (using 4.5 × more detectors).

For the 70 cm cylindrical source embedded in a 70 cm cylindrical water phantom, both with 20 cm diameter, the phantom's attenuation and scanner motion represent more accurate clinical conditions. The ST-TB-PET detects 5.4 cps/kBq, compared to 1.3 cps/kBq for the reference cylindrical system, demonstrating the advantage of the flat panel configuration in head and torso scanning with attenuation.

XCAT

The results for the XCAT simulation for all three systems (including scanning motion) are shown in Figure 2. In the transverse and sagittal views of the flat-panel images, limited-angle artifacts can be observed. These are most obvious for the ST-TB-PET. Differences in count statistics are due to the sensitivity variations and different simulation times. Simulation times were set realistically: the reference cylindrical system reflects clinical practice, while the simulation time of the ST-TB-PET was limited to prevent excessive motion artifacts, as the patient must stand during acquisition.

Figure 2: XCAT simulations for different PET scanner designs for different image views (coronal, sagittal, transverse): Slide-Through Total-Body PET (47.9 M counts), Large reference flat-panel system (62.2 M counts) and Reference cylindrical system (83.8 M counts).

Slide-Through Total-Body PET	**Large reference flat-panel system**	**Reference cylindrical system**
4 min scan	30 sec scan	9.15 min scan
Coronal:		

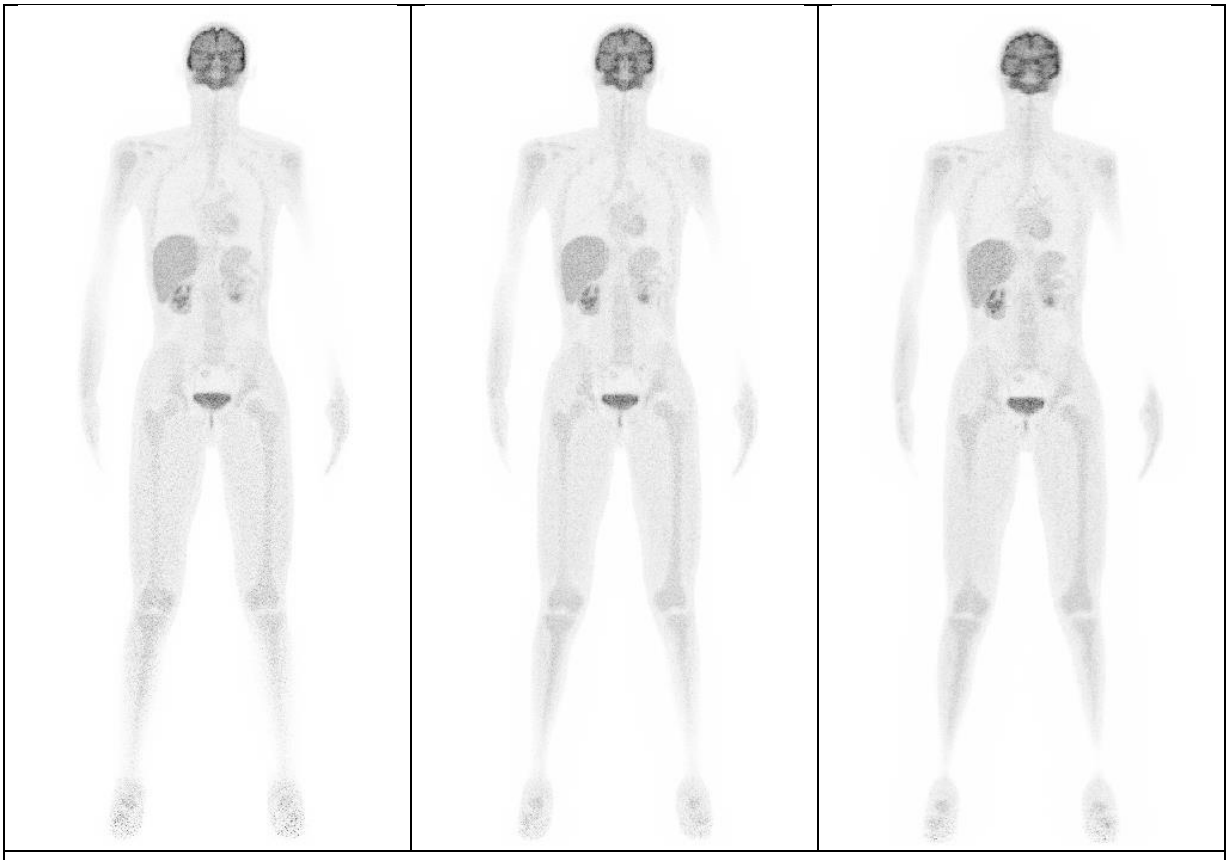

Sagittal:

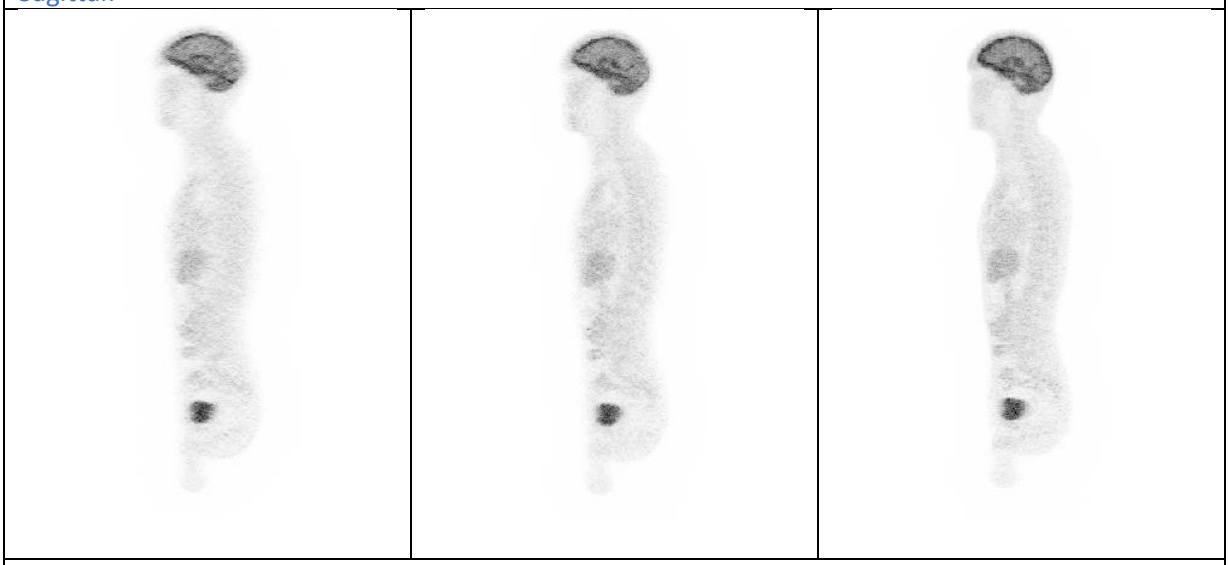

Transverse:

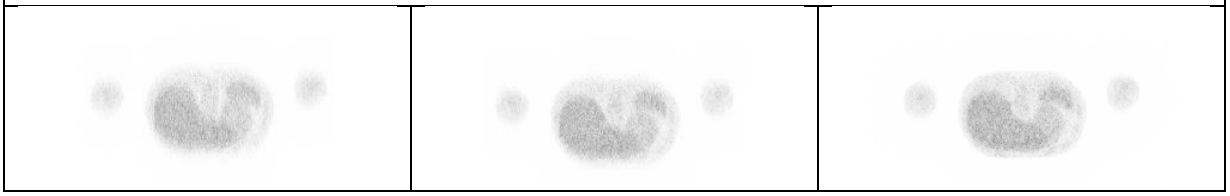

Conclusions

The sensitivity study benchmarks the reference cylindrical system against the Biograph Vision 600 NEMA sensitivity, providing validation for the model. The results show that the concept of ST-TB-PET results in high quality reconstructions for a limited number of detectors. The ST-TB-PET system shows improved performance in detected counts over the reference cylindrical system in dynamic scanning conditions with attenuation, highlighting the advantages of a flat panel configuration for head and torso imaging. However, in stationary conditions, the sensitivity of the large reference flat-panel system is still much higher, emphasizing the importance of extended geometric coverage.

The XCAT phantom results demonstrate that a 4-min scan on the ST-TB-PET results in decent image quality, comparable to a 9-minute scan on the reference cylindrical system, thanks to its higher sensitivity and resolution. The ST-TB-PET is affected by limited angle artifacts, but outlines of the organs are still clear. The large reference flat-panel system is less affected thanks to the increased coverage.

This study is ongoing: the impact of these elongation artifacts will be studied by including hot spheres in the XCAT to study contrast recovery of small lesions. Also the spatial resolution will be studied and its variations throughout the FOV will be investigated. To reduce limited angle artifacts for this system, we will also explore alternative motion strategies to extend the angular coverage, and assess the impact using similar evaluation strategies.

References

[1] S. R. Cherry et al., “Total-Body PET: maximizing sensitivity to create new opportunities for clinical research and patient care,” *JNM*, Sep. 2017, doi: 10.2967/jnumed.116.184028.

[2] S. Vandenberghe *et al.*, “Walk-through flat panel total-body PET: a patient-centered design for high throughput imaging at lower cost using DOI-capable high-resolution monolithic detectors,” *EJNMMI*, Jul. 2023, doi: 10.1007/s00259-023-06341-x.

[3] M. M. Peña-Acosta et al., “Application of NEMA protocols to verify GATE models based on the Digital Biograph Vision and the Biograph Vision Quadra scanners,” *Zeitschrift Für Medizinische Physik*, Feb. 2024, doi: 10.1016/j.zemedi.2024.01.005.

[4] M. Stockhoff et al., “High-resolution monolithic LYSO detector with 6-layer depth-of-interaction for clinical PET,” *PMB*, Jul. 2021, doi: 10.1088/1361-6560/ac1459.

A GENERIC PRECLINICAL MODEL FOR DOTA-TATE-BASED TRT: PHYSIOLOGICALLY-BASED PHARMACOKINETIC INSIGHTS INTO ^{161}TB-DOTA-TATE AND ^{177}LU-DOTA-TATE

Justine Henriot,[1], Lara Struelens,[2], Michelle Andersson,[3], Sunay Perez Rodriguez,[3], Michel Koole,[4], Clarita Saldarriaga Vargas,[3]

[1] Dosimetry research for targeted radionuclide therapy, Department of Nuclear Medical Applications, Belgian Nuclear Research Centre (SCK CEN), Mol, BELGIUM
[2] Nuclear Medicine and Molecular Imaging, Department of Imaging and Pathology, Katholieke Universiteit Leuven (KUL), Leuven, BELGIUM
[3] Medical Physics Department, Institut Jules Bordet, Université Libre de Bruxelles (ULB), Brussels, BELGIUM

Aims

Targeted radionuclide therapy (TRT) is clinically used for treating neuroendocrine tumors (NET) overexpressing the somatostatin receptor type 2 (SSTR2). [^{177}Lu]Lu-DOTA-TATE, that binds with high affinity to SSTR2 and emits β^--particles, is currently the only FDA- and EMA-approved radioligand for this therapy. Meanwhile, [^{161}Tb]Tb-DOTA-TATE is an emerging radiopharmaceutical with a similar β^--spectrum, but with additional emission of Auger and internal conversion electrons, offering potentially higher efficacy for SSTR2-based TRT. Given their similar physicochemical properties, we propose developing a generic preclinical physiologically-based pharmacokinetic (PBPK) model. PBPK modeling, is a helpful tool to understand activity distribution, tissue uptake, and optimize treatment strategies. In this study, we apply PBPK modeling to investigate whether a single generic model could accurately describe the pharmacokinetics of different therapeutic DOTA-TATE-based radiopharmaceuticals and therefore predict their uptake in organs at risk and tumoral lesions.

Methods

A murine whole-body PBPK model for [^{161}Tb]Tb-DOTA-TATE was implemented using MATLAB Simbiology®. The model structure and model parameters were based on a published [^{212}Pb]Pb-DOTAM-TATE tumor mice PBPK model (1). An overview of the development, testing and application workflow of the PBPK model is summarized in Figure 7.

The model was initially developed in healthy mice, to accurately describe the organs at risk such as kidneys. The model was adapted to reflect the physicochemical properties of [^{161}Tb]Tb-DOTA-TATE, incorporating novel in vitro binding data (2) and specific mice characteristics. A plasma protein binding of 50% (3) was included, therefore limiting SSTR2-mediated targeting in tissues to unbound radio-DOTA-TATE. The competition between labeled and unlabeled DOTA-TATE regarding SSTR2 targeting was refined by implementing separate administrations and distributions. Model kinetic parameters and SSTR2 densities were fitted to preclinical biokinetic data of [^{161}Tb]Tb-DOTA-TATE in the kidneys, pancreas, liver, spleen, and lungs (C57Bl/6JRj mice). Model performance was evaluated by comparing the simulated time-integrated activities (TIA) with the experimental data. A good prediction is usually defined by relative errors falling between -50% and +100%. The model was then verified using an independent dataset (4), prior to its application to [^{177}Lu]Lu-DOTA-TATE data.

The [^{161}Tb]Tb-DOTA-TATE model was further developed for tumor-bearing mice by re-fitting the SSTR2 densities and kinetic parameters of both tumor and pancreas based on corresponding biokinetic data (BALB/c nude mice bearing a CA20948 rat pancreatic tumor (5)). In absence of a verification dataset, the developed model was then directly applied to [^{177}Lu]Lu-DOTA-TATE data to assess its generalizability.

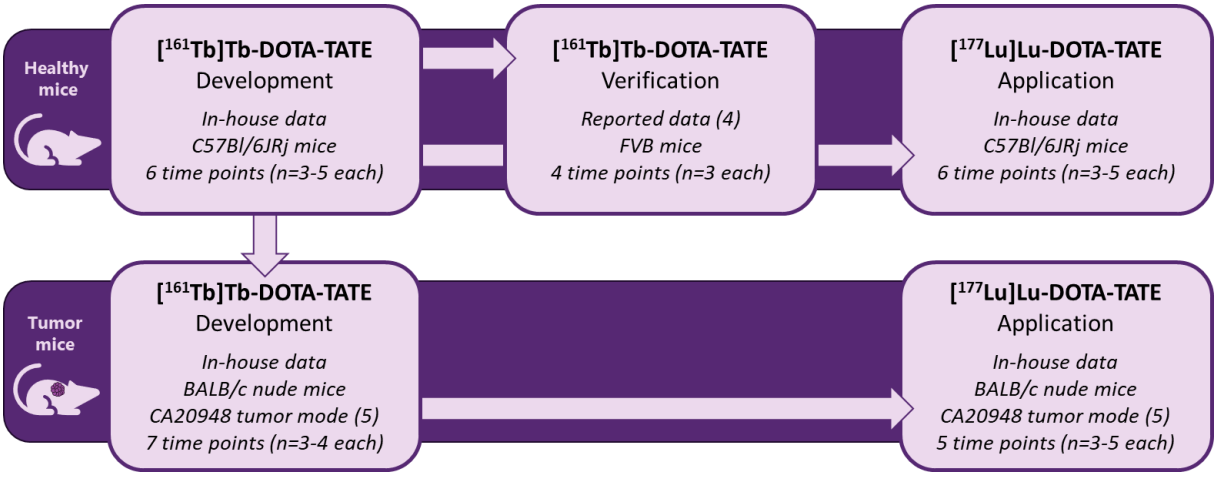

Figure 7 Workflow summary

Results

The PBPK model for [^{161}Tb]Tb-DOTA-TATE in healthy mice was successfully developed showing a good fit of the model to the biodistribution data. The relative errors for TIAs ranged from -7% to +65% in the development dataset, and from +21% to +95% in the verification dataset (4). Model verification confirmed the model kinetic parameters, but highlighted the need for further optimization of tissue SSTR2 densities. Applying the healthy mice model to [^{177}Lu]Lu-DOTA-TATE data also showed successful results, with TIAs relative errors ranging between -40% and +39%. Notably, the TIAs in kidneys were always very accurately predicted with relative errors between -1% and +21%.

When scaling the PBPK model to tumor-bearing mice injected with [^{161}Tb]Tb-DOTA-TATE, a good visual fit was observed. However, some TIAs were overestimated, with relative errors reaching up to 173%. Nevertheless, TIAs of kidneys and tumor were very well predicted with relative errors of +3% and -15%, respectively. The developed model performed well when applied to [^{177}Lu]Lu-DOTA-TATE, resulting in TIA predictions with relative errors between -41% for the tumor and +60%, and specifically -33% for the kidneys. All time activity curves are presented in Figure 8.

SSTR2 densities were fitted at different stages of model development. We hypothesize that these discrepancies across models arise from differences between mouse strains. Still, the relative SSTR2 levels between organs obtained in fitted parameters remained relatively constant in all mice strains. Indeed, defining the kidneys as a reference (100%), the simulated proportions were on average 19 ± 3% for the pancreas, 2 ± 1% for the liver, 1 ± 0% for the spleen, and 10 ± 5% for the lungs (mean ± standard deviation).

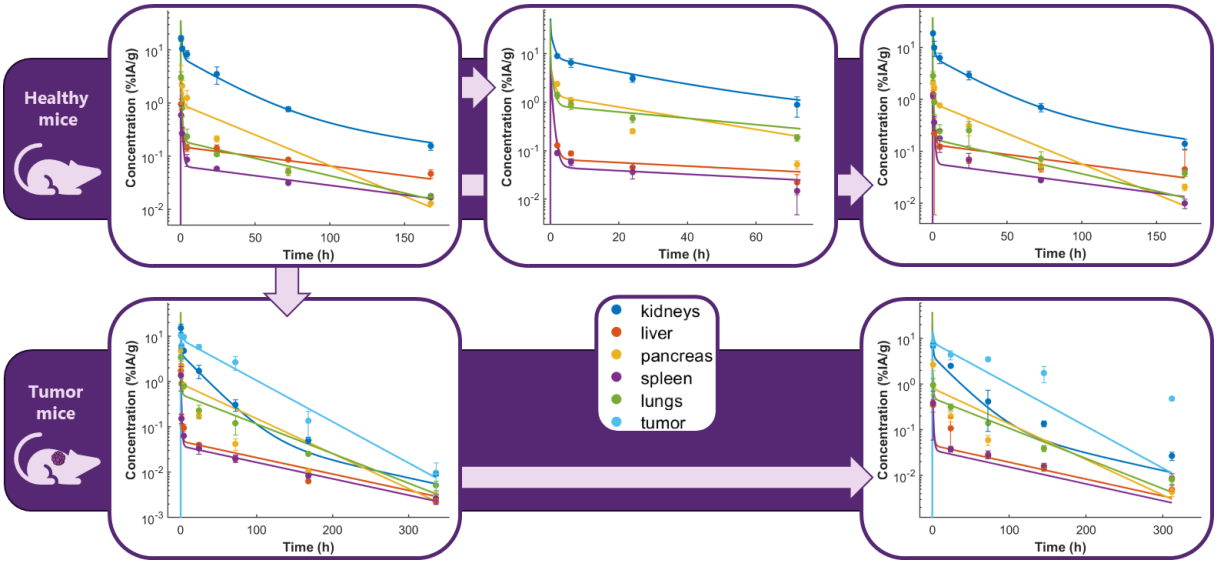

Figure 8 Workflow summary with time-activity curves in major organs. Dots: experimental data. Curves: simulated data.

Conclusions

The developed PBPK models successfully described the pharmacokinetics of [^{161}Tb]Tb-DOTA-TATE both in healthy and tumor-bearing mice. Our findings also indicate that the models can be applied to [^{177}Lu]Lu-DOTA-TATE, demonstrating its general applicability for DOTA-TATE-based TRT and supporting the clinical translation of the model to predict tumoral and organ uptake of both [^{161}Tb]Tb-DOTA-TATE and [^{177}Lu]Lu-DOTA-TATE in NET patients. SSTR2 densities emerged as strain-specific parameter essential for accurately matching experimental data. Their significant influence on the radiopharmaceutical kinetics emphasized the need for a precise characterization and quantification of SSTR2 expression in tissues, which will be the focus of our future research. These preclinical results constitute a first step towards the application of PBPK modeling to support dosimetry-based TRT personalization with radiolabeled somatostatin analogues.

References

1. Zaid NRR, Kletting P, Winter G, Prasad V, Beer AJ, Glatting G. 2021. *Pharmaceutics*. 13(12):2132
2. Spoormans K, Struelens L, Vermeulen K, Saint-Hubert MD, Koole M, Crabbé M. 2024. *J. Nucl. Med.*
3. Hennrich U, Kopka K. 2019. *Pharmaceuticals (Basel)*. 12(3):114
4. Busslinger SD, Mapanao AK, Kegler K, Bernhardt P, Flühmann F, et al. 2024. *Eur J Nucl Med Mol Imaging*. 51:4049–61
5. Bernard BF, Krenning E, Breeman W a. P, Visser TJ, Bakker WH, et al. 2000. *Nuclear Medicine Communications*. 21(11):1079

MULTICENTER COMPARISON OF ACTIVITY METERS AND SPECT/CT IMAGING FOR QUANTITATIVE LUTETIUM-177 MEASUREMENTS

Wies Claeys,[1], Kristof Baete,[2], Laurence Beels,[3], Claire Bernard,[4], Rachele Danieli,[5], Yves D'asseler,[6], An De Crop,[7], Michel Hesse,[8], Victor Nuttens,[9], Bruno Vanderlinden,[10], Michel Koole,[11]

[1] Ku Leuven; Imaging and Pathology, [2] Uz Leuven; Nuclear Medicine, [3] Az Groeninge; Az Groeninge; Nuclear Medicine, [4] University of Liege; Chu Liege; Nuclear Medicine, [5] Institut Jules Bordet, [6] Uzgent; Uzgent; Nuclear Medicine, [7] Az Delta; Az Delta; Nuclear Medicine, [8] Cliniques Universitaires Saint-Luc; Cliniques Universitaires Saint-Luc; Department of Nuclear Medicine, [9] Ku Leuven; Azorg; Nuclear Medicine, [10] Hôpital Universitaire de Bruxelles; Institut Jules Bordet; Medical Physics, [11] Ku Leuven; Uz Gasthuisberg; Nuclear Medicine and Molecular Imaging

Aims

Following the recent successes of radionuclide therapies for treating neuroendocrine tumors and prostate cancer, the therapeutic use of ^{177}Lu has dramatically increased in clinical practice. The number of hospitals providing these therapies as well as the number of patients treated have quickly expanded. For optimal treatment quality of each patient and to ensure comparable results across hospitals, especially in clinical trials, it is crucial to accurately and consistently measure the administered activity and use standardized quantitative SPECT/CT imaging procedures. Therefore, the goal of this study is to investigate the accuracy of ^{177}Lu measurements using activity meters and SPECT/CT imaging in different centers across Belgium, and to assess the variability between the equipment across hospitals.

Methods

2 vials and 2 imaging phantoms were measured over 2 weeks at 8 different hospitals that regularly perform ^{177}Lu-therapies. These hospitals were chosen to obtain a representative selection of SPECT/CT scanners (Siemens, GE, Spectrum Dynamics) and activity meters (Capintec, Comecer).

The vials and phantoms were prepared at UZ Leuven using two activity meters and a gamma counter that were previously calibrated against the Fidelis, the secondary standard radionuclide calibrator of the Belgian Nuclear Research Center (SCK CEN).

Two different vial geometries were tested: a 10 ml Schott Type 1 plus reference vial containing 4ml of solution (291MBq at start of the measurements) and a 25 ml SV-25A vial containing 10 ml of solution (158 MBq at start of the measurements). Each site performed multiple measurements with each vial using their site-specific clinical ^{177}Lu-protocol.

The phantoms were a uniform cylinder (814 MBq in 6.3l) and a NEMA IEC body phantom with a 6 cm sphere (3.75 MBq/ml in the spheres, no activity in the background). Each site imaged the phantoms using their own clinical ^{177}Lu-SPECT/CT protocol, as well as a standardized protocol. Moreover, the sites with SPECT scanners that were calibrated for ^{177}Lu, were asked to use the resulting images to estimate the total activity inside each phantom, using the methodology of their choice.

Results

In total, 8 activity meters (2 x CRC-55tR, 6 x VIK-202) were tested using 9 different protocols, see figure 1. A maximum spread of 11% between the different activity meters was observed, with 7 out of 9 reported activities having a deviation of less than 5%. This spread is due to non-standardized measurement protocols, mostly relying on calibration using various vials from different radiopharmaceutical companies. Therefore, calibration

with respect to a common traceable standard like the Fidelis, could further improve the accuracy of activity measurements.

The results for the SV-25A vial were very similar: the mean relative response compared to the Schott vial was -0.6% and -0.4% for the VIK-202 and CRC-55tR respectively. This shows that the vial geometry only has a minor impact the activity measurements of ^{177}Lu.

In total, 8 SPECT scanners (Discovery 670, Discovery 870, 2 x Starguide, Symbia, 2 x Intevo Bold, Veriton) were calibrated for ^{177}Lu. The SPECT-based estimation of the activity inside the uniform cylinder for all these systems is summarized in figure 2. In general, the deviations are larger than for the activity meters: the maximum spread of reported activities was 20%, with 6 out of 8 systems having an accuracy of 10% or better.

Analysis of the cylinder data showed that the system sensitivity is similar across NaI(Tl) cameras of the same manufacturer (10-12 cps/MBq for GE systems, 19-20 cps/MBq for Siemens systems), while CZT systems showed a much higher sensitivity. Further analysis of the NEMA phantom data will be performed to compare the image quality and resolution between the various systems.

Conclusions

This study found a 10% spread of activity measurements using activity meters across different hospitals. This shows that the current method using vials supplied by pharmaceutical companies can be further improved by direct calibration to a secondary standard like the Fidelis.

Furthermore, a spread of 20% in SPECT-based activity quantification was observed for the uniform cylinder. This shows the challenge of image-based activity quantification compared to direct measurement using activity meters, highlighting the need for improved methodologies and harmonization.

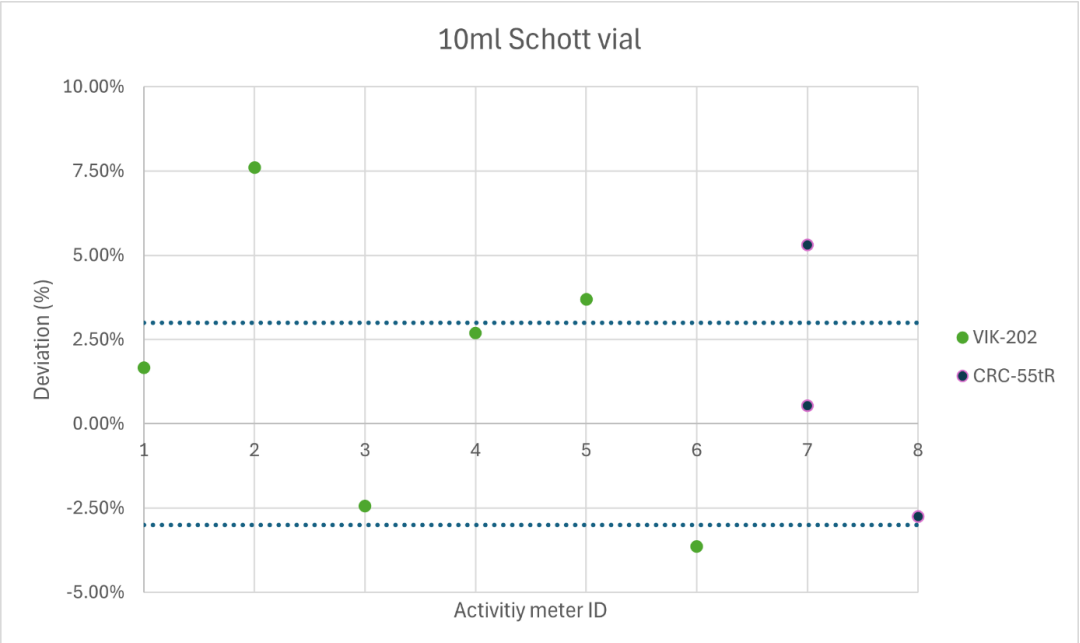

Figure 9: Activity in the Schott vial measured at the different sites, compared to the true activity that was determined using two separate activity meters that were calibrated against the Fidelis secondary standard. The

95% confidence interval for the true activity is 3%, indicated by the dashed lines. Note that activity meter 7 had a separate protocol for ^{177}Lu-PSMA and ^{177}Lu-DOTATATE.

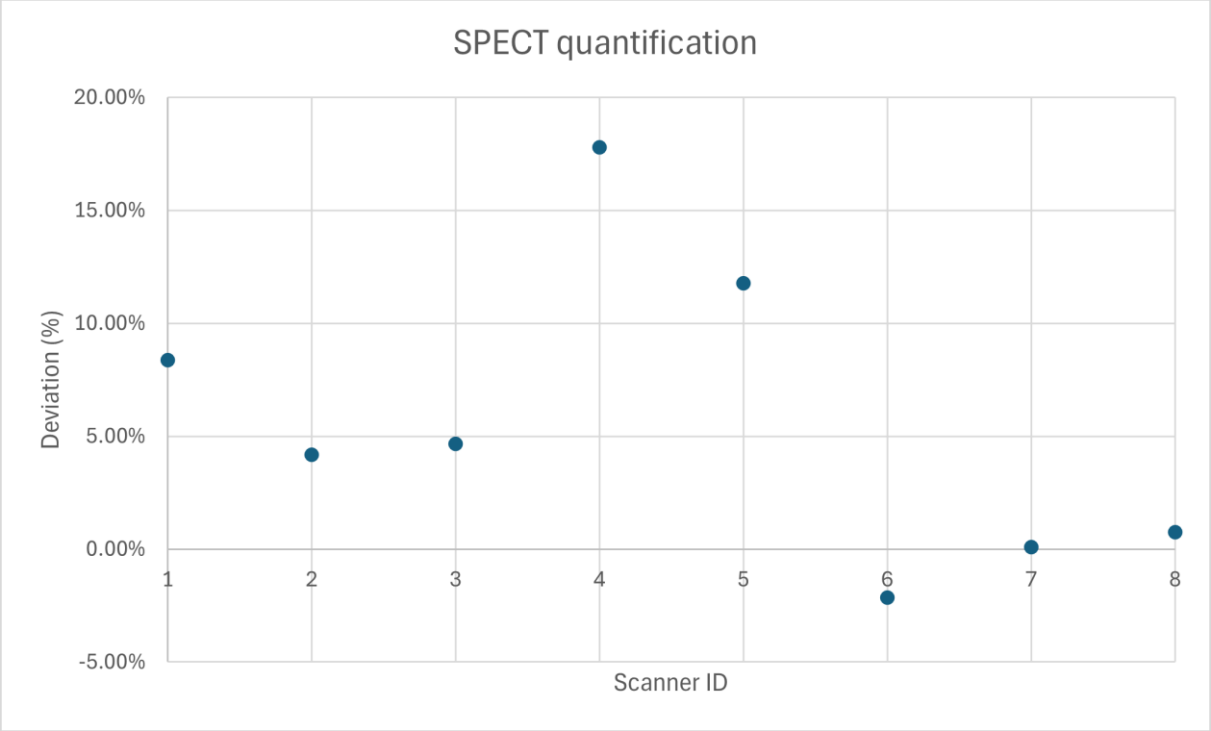

Figure 10: The image-based activity in the cylindrical phantom for the different calibrated SPECT systems. The true activity was calculated from the measurements using the calibrated gamma counter.

COUNTING, CONTOURING AND CONVERGENCE: ROBUSTNESS OF QUANTITATIVE SPECT/CT FOR CARDIAC AMYLOIDOSIS

Stijn De Schepper,[1], John Dickson,[2], Gopinath Gnanasegaran,[3], Tim Van den Wyngaert,[4]

[1] Antwerp University Hospital; Antwerp University Hospital; Nuclear Medicine, [2] University College of London Hospitals Nhs; Institute of Nuclear Medicine; Institute of Nuclear Medicine, [3] Royal Free London NHS Foundation Trust; Royal Free Hospital; Nuclear Medicine, [4] Antwerp University Hospital; Nuclear Medicine

Aims

Cardiac SPECT/CT for diagnosing amyloid transthyretin cardiomyopathy (ATTR-CM) lacks contrast on CT between affected and unaffected myocardium or bloodpool. As a result, contouring is done on SPECT-only images. The current study aims to show how iteration number and resolution modeling (RM) affect different contouring methods in quantitative SPECT/CT for ATTR-CM. A 3D-printed anthropomorphic phantom of a heart was developed based on MRI imaging of a patient with severe cardiac hypertrophy due to ATTR-CM.

Methods

An MRI scan of a severely hypertrophic heart due to ATTR-CM was segmented and used to create an anthropomorphic phantom with three compartments: 1) affected myocardium: apex to mid-ventricles; 2) unaffected myocardium: top of ventricles and atria combined, 3) Blood pool. The phantom was filled with $^{99m}TcO_4$ activity concentrations based on patient data with a target-to-background ratio of 5:1 (59 kBq/mL:12 kBq/mL). All scans were performed on a GE Discovery 670 NM/CT 16 slice SPECT/CT camera (GE Healthcare, Haifa, Israel) with LEHR collimators (120 projections at 100-seconds per projection, 128x128 matrix, detectors at 30cm from the center of rotation). The SPECT/CT and radionuclide calibrator were cross-calibrated according to the manufacturer's recommendation. All data was reconstructed using the quantitative OSEM reconstruction in MIM 7.3.2 (MIM Software Inc., Cleveland, USA) with increasing number of iterations (fixed 10 subsets), with and without RM. Contouring was either manual on CT, by thresholding (25%, 50%) or edge detection.

Results

Edge detection had great difficulties providing stable contours and showed susceptibility to the chosen starting voxel. Therefore, this method was not considered for further investigation. Overall, RM improved activity recovery and, unexpectedly, also the convergence rate, except for the blood pool compartment. For all methods when RM was applied, the activity recovery reaches convergence after 90 updates, but for the threshold methods divergence is observed from 120 iterations onwards (figure 1D). Similarly, the contrast-to-noise ratio (CNR) and number of voxels show convergence, with marked increases in CNR and decreases in voxels for threshold methods after 120 updates when RM is applied (figure 1E&1F).

When contour volumes converge, both thresholds either overestimate (threshold 25%) or underestimate (threshold 50%) the true volume (figure 1C&F). The geometric agreement of the 25% threshold and the manual contours was best (Dice coefficient: 0.72). When RM was applied, higher iterations (above 120 updates) resulted in countours containing mostly noise rather than the actual tracer uptake. To test the impact of noise on countouring performance, two regions of background activity were added representing the spine and liver, and reconstructions with reduced counting statistics were performed through Poisson sampling. Adding the background volumes improved the recovery curve, but did not change the convergence rate. Using lower count statistics consisting of 10% and 5% of the phantom data and reconstructed with the same settings, showed no difference in the convergence rate for the 10% statistics. In contrast, at 5% of the data there was a complete lack

of convergence (Figure 2). Similar convergence behavior was observed in a preliminary analysis of two ATTR-CM patients when RM was applied.

Conclusions

An anthropomorphic phantom for ATTR-CM was developed to study the impact of RM and iteration number on contouring methods. Edge detection was unable to achieve stable contouring. The threshold methods either achieved geometric agreement (threshold 25%) or high recovery (threshold 50%). RM improved the convergence of threshold methods, but suffers from noise at higher iterations. Therefore, further validation in patient data is warranted to define a reliable window of convergence for threshold methods. Alternatively, manual contouring may be preferred.

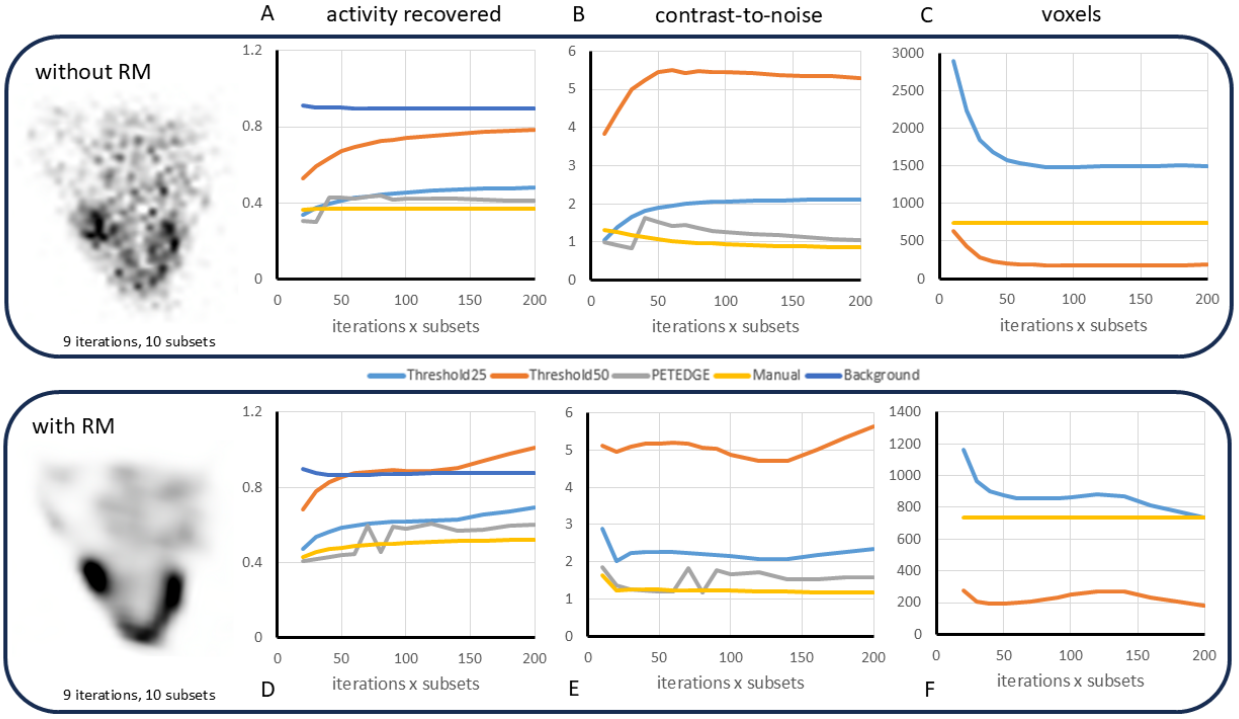

Figure 11 An overview of the results for activity recovery, contrast-to-noise ratio and number of voxels in each contouring method.

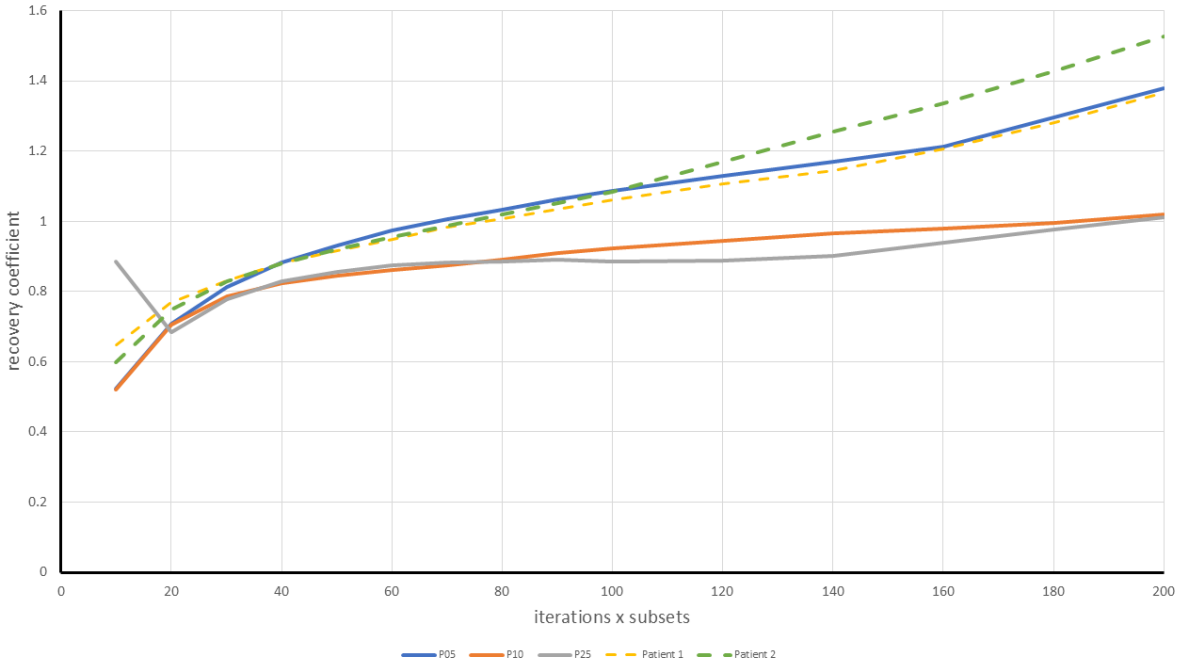

Figure 12 The evolution of recovery coefficients of the Poisson sampled data for the 50% threshold contours when RM is applied. The activity concentration for the patients was normalized to match the 88% recovery of P05 at 40 updates. P25: 25s/projection equivalent, P10: 10s/projection, P05: 5s/projection

LOW-COUNT WHOLE-BODY PET WITH DEEP LEARNING IN A MULTICENTER, MULTI-TRACER AND EXTERNALLY VALIDATED STUDY

Justine Maes,[1], Charles Carron,[2], Simon Dekeyser,[3], Tomas Brants,[3], Amine Chaouki,[4], Azzam Abdalla Ibrahim,[5], Camille Steenhout,[6], Gerard Moulin-Romsee,[1], Isaac Kargar Samani,[7], Ludovic D'hulst,[8], Sezgin Ustmert,[9], Maarten Larmuseau,[10]

[1] Ku Leuven, [2] Ku Leuven; Uz Leuven; Nuclear Medicine, [3] Nuclivision, [4] Chirec, [5] Adrz Goes, [6] Chu of Liège, [7] Epicura; Médecine Nucléaire, [8] Sat, [9] Az Groeninge, [10] Ugent

Aims

The increasing demand for PET scans, particularly for long-term cancer surveillance, has raised concerns about cumulative radiation exposure. Additionally, PET imaging is gaining prominence in neurodegenerative diseases such as Alzheimer's, where amyloid and tau-based tracers aid in early diagnosis and treatment planning. However, high tracer costs and delays in reimbursement limit accessibility and widespread clinical adoption.

Recent advancements in deep learning and convolutional neural networks (CNNs) present a promising solution. By employing in-silico enhancement techniques, high-quality PET images can be achieved with reduced scan times and lower radiotracer doses. This innovation mitigates radiation risks and reduces overall imaging costs, improving accessibility across medical fields.

Despite these advancements, training deep learning models for low-count PET image enhancement poses challenges: (a) ensuring generalizability across diverse imaging centers and radiotracers, (b) preserving quantitative accuracy in lesions, and (c) preventing over-smoothing due to noise level differences between training and real-world data. Thus, rigorous validation in multi-center, multi-tracer, and multi-protocol clinical studies is crucial.

In this study, we evaluate NUCLARITY, an encoder-decoder CNN, in a blinded, multi-center, multi-tracer, and externally validated reader study. We assess its performance in terms of image quality, quantitative accuracy, and lesion detection to determine its clinical viability and potential impact on PET imaging workflows.

Methods

PET scan data were collected from three European hospitals in list-mode format, which records all radioactive events during the scan. To simulate a 50% reduction in scan time or radiotracer dose, only half of the measured positron emission events were used for reconstruction. Matched clinical and 50% reduced scans were obtained from 65 subjects. GDPR compliance was assured and all scans were anonymized from patient health information. Eligible subjects were adults undergoing standard whole-body PET-CT with 18F-FDG (40 patients), 18F-PSMA (10 patients), 68Ga-PSMA (10 patients), or 68Ga-DOTATATE (5 patients) for diverse malignancies and varying disease stages. The PET scan data was acquired with a GE Omni Legend, GE Discovery MI and Siemens Biograph 128 mCT.

The 50%-reduced scans were processed using NUCLARITY, a deep learning algorithm developed by NUCLIVISION. NUCLARITY employs a CNN-based approach to enhance image quality by reducing noise while preserving structural details. It analyzes voxel relationships to neighboring pixels, applies optimized filters with minimal pre-processing, and uses a residual learning framework to maintain image integrity.

Six independent nuclear medicine physicians (experience: 2–16 years) conducted a randomized blinded evaluation of the low-count enhanced (LCE) and standard-count (SC) PET scans. Three assessed the 100 18F-labeled scans, while the other three evaluated the 30 68Ga-labeled scans.

Readers identified abnormalities across six body regions: lung, liver, lymph nodes, bone, spleen, and muscle. If more than five abnormalities were detected in a region, the count was capped at six. Readers also provided a diagnostic confidence (DC) score on a 3-point Likert scale (1 = not sure, 2 = confident, 3 = very confident) and a diagnostic image quality (DIQ) score on a 5-point Likert scale (1 = very poor, 2 = poor, 3 = acceptable, 4 = good, 5 = excellent). Sensitivity and specificity were determined by classifying a body region as abnormal if all readers identified at least one lesion. Inter-reader and inter-scan agreement on lesion counts were assessed using Cohen's kappa.

Two additional independent readers reviewed only the SC scans and semi-automatically delineated volumes of interest (VOIs) for abnormal lesions. These VOIs were transferred directly to LCE scans, enabling a direct comparison of quantitative accuracy. Concordance correlation coefficients (CCC) and Bland-Altman plots were used to assess SUVmax and SUVmean in the VOIs.

Results

Pooled DIQ scores for standard-count (SC) and low-count enhanced (LCE) scans were 4.1 ± 0.7 and 3.6 ± 0.7, respectively. Corresponding DC scores were 2.8 ± 0.3 for SC scans and 2.5 ± 0.3 for LCE scans.

A total of 243 hypermetabolic lesions were segmented on SC scans by the additional readers. Quantitative metrics in lesion segmentations showed a strong correlation between SC and LCE scans, with concordance correlation coefficients (CCC) of 1.00 for SUVmean and 0.99 for SUVmax. Outliers, where large SUVmax differences were observed, originated from highly metabolically active regions (SUVmax > 20 in SC scans) in F - and Ga-labeled PSMA scans. As observed from Bland-Altman plots, the mean difference was -0.11 SUV and -0.65 SUV for SUVmean and SUVmax, respectively, with 95% confidence limits of agreement of 0.31 SUV and 3.42 SUV.

Across all readers, 46 body regions were classified as abnormal on SC scans, while 43 of these regions were also identified as abnormal on LCE scans. One false-positive abnormal region was detected on LCE scans, while three regions were missed (false negatives). This resulted in an overall sensitivity of 0.93, specificity of 0.99, and an F1-score of 0.96, with a high correlation in lesion detection between LCE and SC scans (CCC = 0.95).

Inter-reader agreement, averaged over all reader pairs, was 0.44 for LCE scans and 0.47 for SC scans. The inter-scan agreement, averaged across readers, was 0.70 for 18F-labeled data and 0.66 for 68Ga-labeled data.

Conclusions

Our results demonstrate that NUCLARITY effectively enhances PET image quality, enabling comparable lesion detection and quantitative accuracy to standard-count scans while using only half the radiotracer dose or scan time. The high concordance between SUV measurements in SC and LCE scans, along with strong sensitivity and specificity, supports the clinical feasibility of deep learning-based PET denoising. While minor variations were observed in highly active lesions, overall diagnostic performance remained robust. This advancement has the potential to significantly reduce patient radiation exposure and imaging costs, making PET scans more accessible. Future studies will focus on further optimizing model generalizability, quantification accuracy and exploring its impact on clinical decision-making.

Technologist Track

131-IODINE THYROID UPTAKE MEASUREMENT IN HYPERTHYROIDISM TREATMENT : IMPACT STUDY OF A GOOD POSITIONING WITH DIFFERENT ACQUISITION MODES AND GAMMA-CAMERAS, A TECHNOLOGIST JOURNEY

Éléonore Crasson,[1], Benoît Collette,[2], Eric Ligot,[3], Sophie Boeckmans,[4], Bruno Vanderlinden,[5], Rodrigo Moreno,[6], Carlos Artigas,[7], Patrick Flamen,[8]

[1] Haute Ecole Léonard de Vinci - Ipl, [2] Hub Hôpital Erasme - Ulb; Nuclear Medicine, [3] Haute Ecole Léonard De Vinci - Ipl, Woluwe-Saint-Lambert, [4] Hub, Hôpital Erasme-Ulb, [5] Hôpital Universitaire de Bruxelles; Institut Jules Bordet; Medical Physics, [6] Hôpital Universitaire de Bruxelles; Hub - Hôpital Erasme; Nuclear Medicine, [7] Institut Jules Bordet, [8] Hub; Institut Jules Bordet; Nuclear Medicine Imaging and Radionuclide Therapy

Aims:

Measuring thyroid uptake is a primordial step in determining the most effective 131-Iodine treatment for patients with hyperthyroidism. This study aims to assess how different thyroid positions and technical choices affect the acquisition of thyroid uptake measurements. The primary objective is to assist physicians and technologists in identifying the most reliable and reproductible methods for thyroid uptake camera-based measurements.

Methods:

This study utilized two types of phantoms : a thyroid-like phantom (Figure 1) and a neck phantom containing a reference “standard” vial (Figure 2) mimicking clinical practice with exactly the same activity, in planar imaging. We used three gamma-cameras : a Philips BrightView SPECT and a GE Aurora SPECT/CT both with classical crystal thicknesses, and a GE 870 DR SPECT/CT with a thicker crystal. In order to evaluate the influence of the distance from collimator and lateral position changes on the uptake measurements, a first round of acquisitions was performed using 99m-Technetium. This was assessed using two types of collimators : a pinhole (for the BrightView only) and low energy parallel holes (for all cameras). In a second round, same measurements were performed using 131-Iodine (excepting the parallel holes for the BrightView because no high energy was available). For 131-Iodine, both planar imaging and SPECT/CT were conducted to evaluate the added value of such tomography. In planar imaging, both thyroid phantom and “standard” vial (in a neck phantom) images were analyzed through a semi-automatic MIM software workflow (Figure 3). In SPECT/CT, only one volume containing the thyroid phantom and the “standard” vial (without neck phantom) was acquired and analyzed in MIM. Activities being the same in the phantoms, the uptake result must be 100 %.

Results:

Our results show a considerable variation in the measurements using pinhole collimator as compared to parallel hole collimators measurements. An overestimation of the uptake by 20% to 22% was found (Table 1 with 99m-Tc and 131-I respectively) for a perfectly centered position of the thyroid, 5 cm far from the pinhole, our x = 0, y = 0, and z = 0 (0,0,0) position. The uptake measurement decreases with lateral shift and even more with vertical

remoteness (Figure 4 and Table 2), reaching more than 50% decrease for a 5 cm distance shift (0,0,-5). In contrast, using parallel hole collimators in planar imaging, we found a decrease of about 7 % for the same 5 cm distance shift and lateral position variations did not produce here significant changes. Also, reaching a 100 % uptake needs to shift the thyroid phantom in the z direction probably due to the different geometries and the lack of attenuation correction (Table 2 and Figure 3). This issue led us to perform 131-Iodine SPECT/CT on the two gamma-cameras equipped with high energy parallel hole collimators. This technique shown few improvements in the thyroid uptake measurements (Table 3), and hospital staff have found it more convenient due to requiring only a single placement for both "standard" vial and thyroid. However, special attention needs to be given to reconstruction parameters and the use of attenuation correction.

Conclusions:

This study shows that using a pinhole for measuring thyroid uptake is not recommended, due to a considerable bias, even if technologists correctly position the patient. Hospitals that have no access to a scintillation probe for thyroid uptake measurement should consider parallel hole collimators and planar or SPECT/CT imaging for a better accuracy.

position (0,0,0)	pinhole Brightview	planar Brightview	planar Aurora	planar 870DR
99m-Tc	120,47%	104,80%	103,52%	104,74%
131-I	122,46%		108,97%	106,51%

Table 1 : Uptake comparison between Philips BrightView with pinhole and parallel hole collimators, GE Aurora and GE 870 DR with parallel hole collimators, for 99m-Tc and 131-I, in planar imaging

position	pinhole Brightview	planar Aurora	planar 870DR
(0,0,0)	122,46%	108,97%	106,51%
(1,0,0)	122,84%		
(1,1,0)	117,09%		
(2,0,0)	113,89%		
(3,0,0)		107,97%	105,43%
(0,3,0)		106,51%	105,30%
(3,3,0)			104,69%
(0,0,-1)	102,15%	104,12%	104,09%
(0,0,-2)	90,07%	103,69%	103,09%
(0,0,-3)	71,17%	100,20%	101,82%
(0,0,-4)	62,62%	99,20%	100,49%
(0,0,-5)	54,01%	95,65%	99,31%

Table 2 : Uptake comparison between Philips BrightView with pinhole collimator, GE Aurora and GE 870 DR with parallel hole collimators, only for 131-I, in planar imaging

Attenuation corretion	GE Aurora	GE 870DR
No	87,63%	87,27%
Yes	104,27%	101,30%

Table 3 : Uptake comparison between GE Aurora and GE 870 DR with parallel hole collimators, only for 131-I, in SPECT/CT imaging

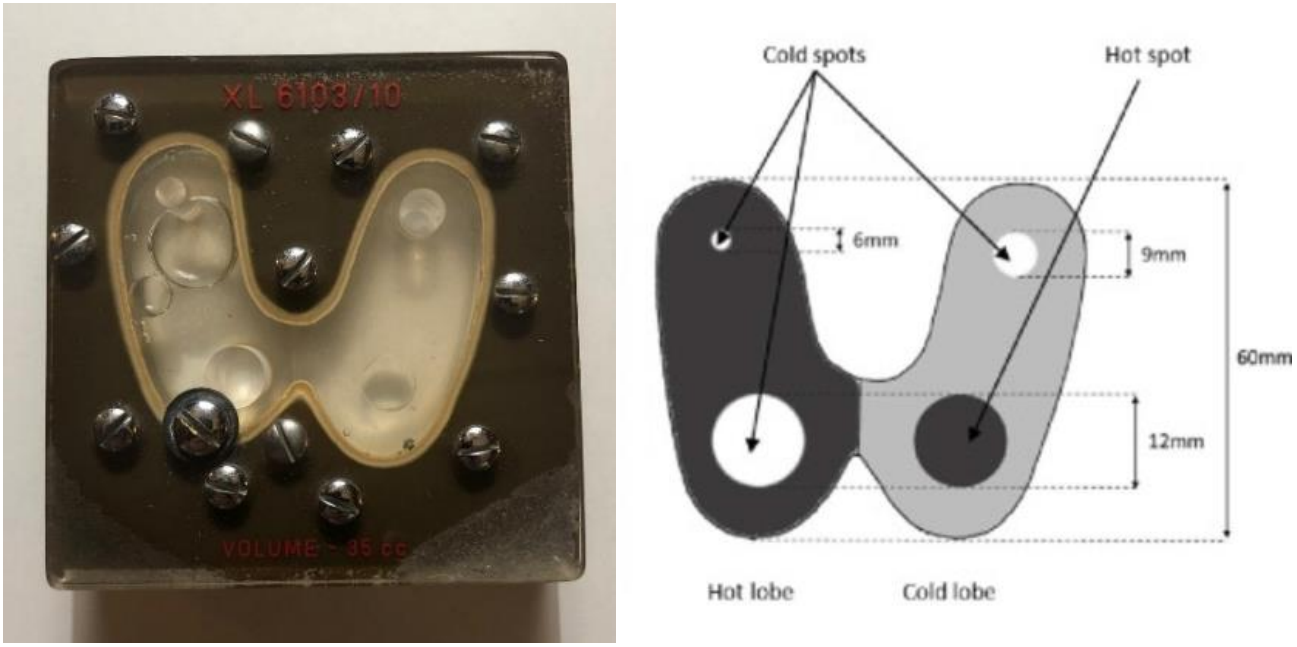

Figure 1 : Thyroid phantom

Figure 2 : Neck phantom with insert for “standard” vial

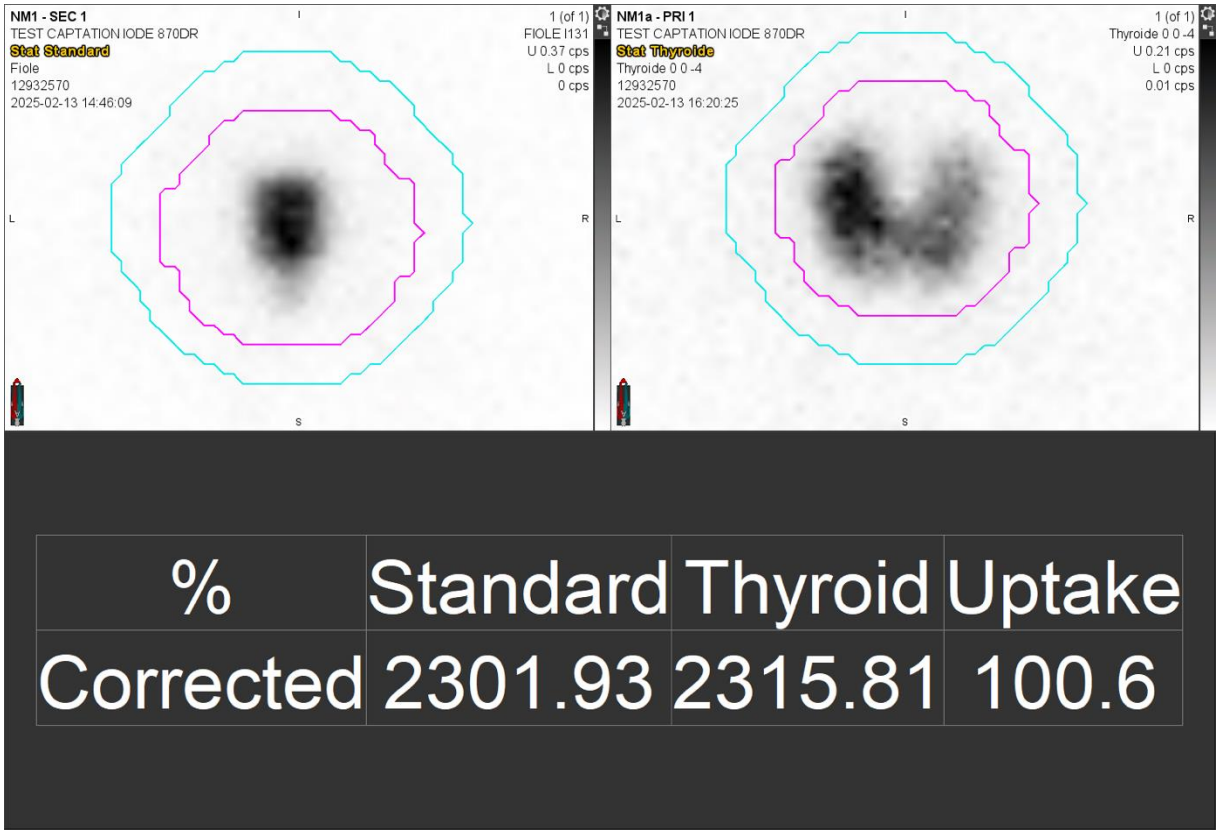

Figure 3 : MIM software workflow results

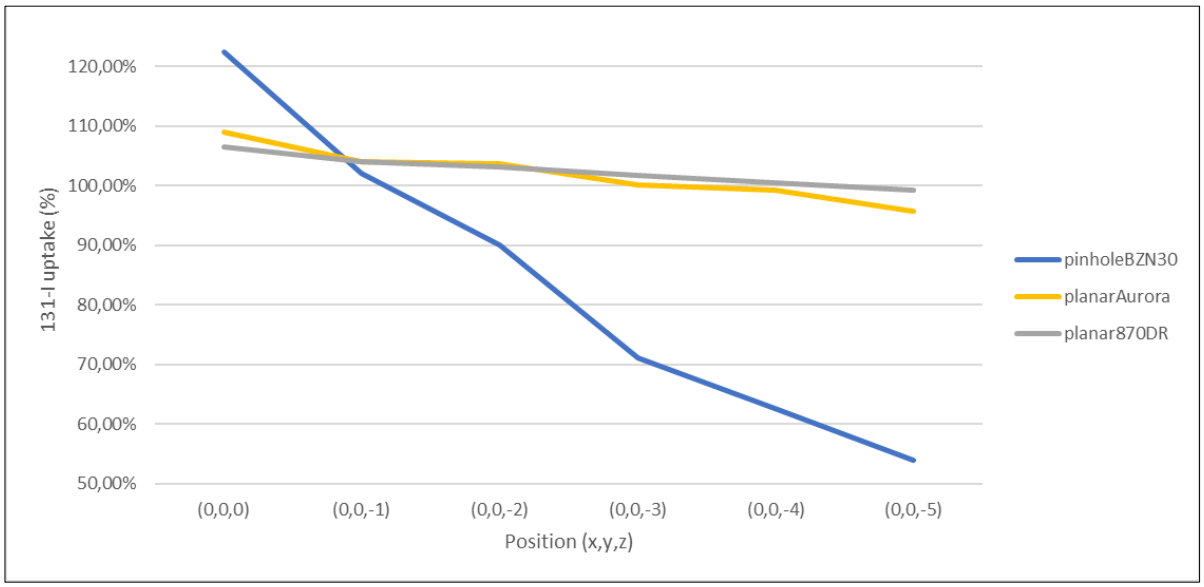

Figure 4 : Comparison of the 131-I thyroid uptake depending on the collimator type (pinhole versus parallel holes) and the crystal thickness, by position remoteness variation between source and detector

IMPLEMENTING A SAFE WORKFLOW FOR INTRA-OPERATIVE PET/CT IMAGING OF SURGICAL SPECIMEN

Femke Verschure,[1], Mathias Colle,[2], Brigette De Paepe,[2], Nico Dhont,[2], Britt Gevaert,[2], Veronique Piens,[2], Liesje Meiresonne,[2], Valérie Vergucht,[2], Karel Decaestecker,[2], Dieter Berwouts,[2], Jeroen Mertens,[2], Bieke Van Den Bossche,[2], Bieke Lambert,[2]

[1] Maria Middelares; Az Maria Middelares, [2] Maria Middelares; Az Maria Middelares, Gent, Belgium

Aims

We installed a mobile PET/CT-scanner in our hospital, designed to acquire high-resolution images of surgical specimens.
This new type of camera aims to assess the metabolic activity of tissue and especially its margins in the operating room.
In this presentation document, we addressed various safety issues when implementing intra-operative PET/CT imaging. We developed a workflow to achieve high quality intra-operative PET/CT images while maintaining ALARA principles.

Methods

Intravenous PET-tracer injection (F18-PSMA for prostate cancer patients; FDG for the remaining patients; 0.8-4MBq/kg) was done 60-90min before tumour resection.
After resection, the specimen was scanned in the operating room for 12min with the AURA10 PET/CT-camera (XEOS) and the specimen was sent for pathology.
We developed a work flow to minimize exposure to ionizing radiation.

In the first 20 procedures our workflow was tested:

We conducted dose rate measurements from injection till transfer to the recovery ward. For patients with a bladder catheter, measurements close to the urinary bag with and without lead shielding were carried out. Surgeons, nurses, and anaesthesiologists were additionally monitored by an electronic dosimeter during the entire procedure.

The patient had to remain in bed post-injection to limit close contact with other patients or personnel. In case of a short-lasting surgical procedure the patient was injected with the PET-tracer at the nuclear medicine department. The patient awaited surgery at the nuclear medicine department, in a controlled area, with dedicated lavatory facilities.

Potential contaminations of the surgical room, instruments and waste were monitored by a survey meter.

The specimens were fixed in formaldehyde for 24h before further processing. No additional radioprotective measures were taken concerning the specimen.

Image quality allowed us to lower the administered activity from 4MBq/kg to 0.8-1MBq/kg.

Results

Dose rates around the patient dropped by a factor >5 when measured at the side of the feet instead of trunk.

Normalized to an injected activity of 1MBq/kg, the estimated median absorbed doses per procedure were 15.6µSv(range 0,7-140,8) and 14,1µSv(0,5-46,2) for the surgeons and instrumenting nurses.

The diuresis was kept low during urological surgery, with dose rates of 14 µSv/h near the urine bag. We positioned the bag at the far side of the surgeon, with lead shielding. At the surface of the suction unit the dose rate was 3 µSv/h.

Measurements with a survey meter did not reveal contaminations of the room. There was no need to shield the surgical specimen itself.

Conclusions

We developed a safe workflow to implement intra-operative PET/CT in a general hospital.

RELATIONSHIP OF POINT-OF-CARE B-HYDROXYBUTYRATE MEASUREMENTS WITH MYOCARDIAL GLUCOSE UPTAKE : AN OBSERVATIONAL STUDY.

Soundès Bourouis,[1], Claire Derneden,[2], Qaid Ahmed Shagera,[3], Francois Jamar,[4], Olivier Gheysens,[5], Virginie Depoortere,[6]

[1] Cliniques Universitaires Saint-Luc; Cliniques Universitaires Saint-Luc; Médecine Nucléaire, [2] Cliniques Universitaires Saint-Luc, [3] Cliniques Univérsitaires Saint-Luc, Uclouvain; Nuclear Medicine, [4] Cliniques Universitaires Saint-Luc (Ucl); Clinique Universitaire Saint-Luc; Nuclear Medicine, [5] Clinique Universitaire Saint-Luc; Cliniques Universitaires Saint-Luc; Nuclear Medicine, [6] Cliniques Universitaires St-Luc

Aims

Myocardial 18F-fluorodeoxyglucose positron emission tomography with computerized tomography (18F-FDG PET/CT) has a well-established role in diagnosing and assessing various inflammatory and infectious cardiac diseases (e.g. sarcoidosis or endocarditis) by highlighting pathologic glucose uptake. A key limitation of 18F-FDG PET is the physiological myocardial glucose uptake, which necessitates an adequate patient preparation to achieve an excellent myocardial glucose suppression (MGS) for obtaining diagnostic images. Accordingly, many efforts were dedicated to achieve MGS by inducing a metabolic shift of the normal myocardial away from glucose. Current strategies vary across institutions worldwide, but consensus documents and guidelines recommend a high-fat and low or no carbohydrate diet for 24-48 hours combined with a prolonged period of fasting for > 12 hours before 18F-FDG administration (with or without intravenous unfractionated heparin 15 min prior to 18F-FDG injection) to optimize MGS. Nevertheless, inadequate suppression occurs in as many as 10-20% of cases, resulting in non-diagnostic or even false positive results. While thorough review of dietary logs is often performed and could theoretically serve as a substitute to assess adequate MGS, no strong relationship has been demonstrated between nutrient intake such as fat and carbohydrates and MGS. Recently, several studies showed a negative correlation between β-hydroxybutyrate (BHB) levels and myocardial glucose uptake. BHB is a ketone produced by the liver via metabolism of fatty acids as a source of energy during insulinopenic state. A major advantage of BHB compared to other substrate analyses, is the use of point-of-care instruments to instantaneously obtain the measurement, making it a clinically attractive and practical tool. The goal of this observational study was to evaluate the relationship between BHB measurements with a point-of-care device and MGS.

Methods

We included 102 patients undergoing 18F-FDG PET/CT for the evaluation of oncologic or inflammatory/infectious diseases and in whom point-of-care BHB level was checked. Patients for oncologic indications underwent a standard preparation with a >6 hour fasting period. A subgroup of 72 patients referred for potential cardiac infection/inflammation had been on a high-fat, low carbohydrate diet for 24-48 hours and a prolonged period of fasting (> 12 hours). No injection of unfractionated heparin was used. Blood glucose and BHB levels were measured from capillary blood immediately prior to FDG injection, using a point-of-care device (for BHB values; FreeStyle Precision Neo, Abbott). All patients underwent 18F-FDG PET/CT 60-90 minutes after injection. Cardiac 18F-FDG PET images were interpreted by two certified nuclear medicine physicians with a third reader to adjudicate discordances. A visual assessment of myocardial glucose uptake was performed using a 4-point grading scale: diffuse myocardial uptake (score 0), uptake at the basolateral wall or basal ring sign (score 1), myocardial uptake equal to left ventricular bloodpool (score 2) and myocardial uptake less than left ventricular bloodpool (score 3). A score 0 was considered as inadequate suppression, score 1 as partially inadequate suppression and score 2 and 3 as good suppression. Data are represented as median values with interquartile ranges. The ability of the BHB value

to predict myocardial suppression equal or less than left ventricular bloodpool was evaluated by receiver operating characteristics (ROC) curve analysis and the optimal cut-off value was determined by Youden index.

Result

Cardiac 18F-FDG PET scans were scored as follows : score 0 : 19, score 1 : 12, score 2 : 35 and score 3 : 36. Median (IQ range) BHB values were significantly lower for scores 0 and 1 compared to 2 and 3, i.e. 0.1 (0.1-0.7), 0.2 (0.1-0.4), 0.8 (0.4-1.2) and 0.8 (0.4-1.2) mmol/L, respectively (Figure 1). When combining scores 0/1 and 2/3, median (IQ range) BHB values were significantly lower for scores 0/1, 0.2 (0.1-0.4) *vs* 0.8 (0.4-1.2), respectively; *P*<0.01. In patients with dietary preparation, confirmed from patient self-reporting (n = 72), median (IQ range) (Figure 2) were significantly higher than in patients without specific preparation 0.7 (0.4-1.2) vs 0.2 (0.1-0.7); *P*<0.05. The median PET score was also higher (2 *vs* 1; P<0.005) in patients with a specific preparation. 76% of the patients with reported adequate dietary preparation had BHB values above the suggested cut-off value of 0.4 mmol/L (communication with M. Pelletier-Galarneau, University of Montreal) as compared with 30% in patients without specific preparation. In our study, based on ROC curve analysis, the AUC was 0.8 (95% CI : 0.7-0.9) and the optimal cut-off value for BHB level was ~0.45 mmol/L to predict good myocardial suppression with a sensitivity of 73% and a specificity of 77%. The correlation between BHB and glucose levels was very weak (R=-0.24).

Conclusions

Measurement of BHB levels before 18F-FDG PET/CT using point-of-care testing is feasible. From this observational study, we observed a significant inverse correlation between BHB values and visual assessment of myocardial uptake. Furthermore, a specific dietary preparation results in higher BHB levels. Integrating BHB measurements may optimize the management of patients referred for 18F-FDG PET in the context of cardiac inflammatory or infectious diseases.

Figure 1

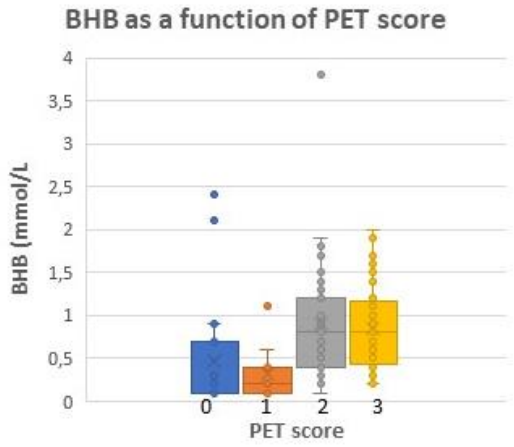

Figure 2

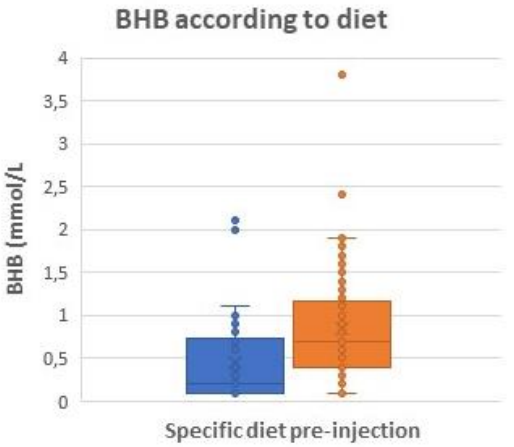

SPLIT RENAL FUNCTION IN LIVING KIDNEY DONORS DERIVED FROM 99MTC-DTPA VS 99MTC-DMSA: A PRELIMINARY EVALUATION

Nabila Laajimi,[1], Asma Bouzidi,[2], Soundès Bourouis,[3], Florian Dupont,[4], Nada Kanaan,[5], Renaud Lhommel,[3], Francois Jamar,[6], Olivier Gheysens,[7]

[1] Cliniques Universitaires Saint-Luc; Médecine Nucléaire, [2] Cliniqueq Universitaires Saint-Luc; Cliniques Universitaires Saint-Luc; Médecine Nucléaire, [3] Cliniques Universitaires Saint-Luc; Cliniques Universitaires Saint-Luc; Médecine Nucléaire, [4] Cliniques Universitaires Saint-Luc; Service de Médecine Nucléaire; Médecine Nucléaire, [5] Cliniques Universitaires Saint-Luc; Néphrologie, [6] Cliniques Universitaires Saint-Luc (Ucl); Clinique Universitaire Saint-Luc; Nuclear Medicine, [7] Clinique Universitaire Saint-Luc; Cliniques Universitaires Saint-Luc; Nuclear Medicine

Aims

The worldwide shortage of deceased kidney donors has led to a significant increase in living kidney donors. For living kidney donation, accurate assessment of pre-transplant renal function of the donor is indispensable for side-selection and to guarantee a sufficient long-term residual renal function. Radioisotopic methods play an important role to measure absolute glomerular filtration rate (GFR) and split renal function with ^{51}Cr-EDTA and ^{99m}Tc-DMSA considered as gold standard respectively. These techniques have been used routinely at our center to measure absolute and split GFR, with a great advantage that both examinations could be performed on one single day. Unfortunately, ^{51}Cr-EDTA is no longer commercially available. ^{99m}Tc-DTPA is a valuable alternative to measure absolute GFR using a single-injection two-sample method but can at the same time be used to obtain split renal function using a short 5-min dynamic acquisition protocol. This approach would have the advantage that both informations can be derived from one single examination, hereby avoiding that the patient needs another exam with ^{99m}Tc-DMSA on another day. The goal of this preliminary study was to evaluate whether absolute GFR and split renal function can be accurately measured from ^{99m}Tc-DTPA in comparison to ^{99m}Tc-DMSA as gold standard.

Methods

In 8 consecutive patients screened for living kidney donation, split renal function was measured using 3 different methods including the conventional geometric mean method for ^{99m}Tc-DMSA (DMSA, reference standard), posterior ^{99m}Tc-DTPA scintigraphy (DTPA PA) and the antero-posterior ^{99m}Tc-DTPA scintigraphy with the geometric mean method (DTPA GM) using the 120-180 sec post-injection window. Manual regions of interest were drawn around the kidneys and a semilunar background region was placed around the kidney for background correction. All image sets were independently analyzed by three experienced technologists. Results were represented as the absolute deviation of the left kidney from the equal split function (50/50) using Spearman correlation coefficient and Bland-Altman plots (mean ± 1.96SD).

Result

Correlation coefficients of the absolute differences between DMSA-DTPA PA, DMSA-DTPA GM and DTPA PA-DTPA GM were 0.37, 0.53 and 0.91, respectively (Fig 1). The differences between DMSA-DTPA PA and DMSA-DTPA GM were -3.52 ± 9.62 and -2.49 ± 6.92, respectively (Fig 2). Inter-observer variability was significantly lower for DMSA compared to DTPA. Based on split renal function derived from DMSA, 7/8 patients were eligible for donation (45-55% window) whereas only 4-5/8 or 2-3/8 were eligible based on DTPA GM and DTPA PA, respectively (Fig 3).

Conclusions

Our preliminary results clearly indicate that in the case of screening for living kidney donation, ^{99m}Tc-DTPA scintigraphy cannot reliably be interchanged with ^{99m}Tc-DMSA scintigraphy for split renal function. A combination of tests is needed to accurately obtain absolute GFR (^{99m}Tc-DTPA) and split renal function (^{99m}Tc-DMSA).

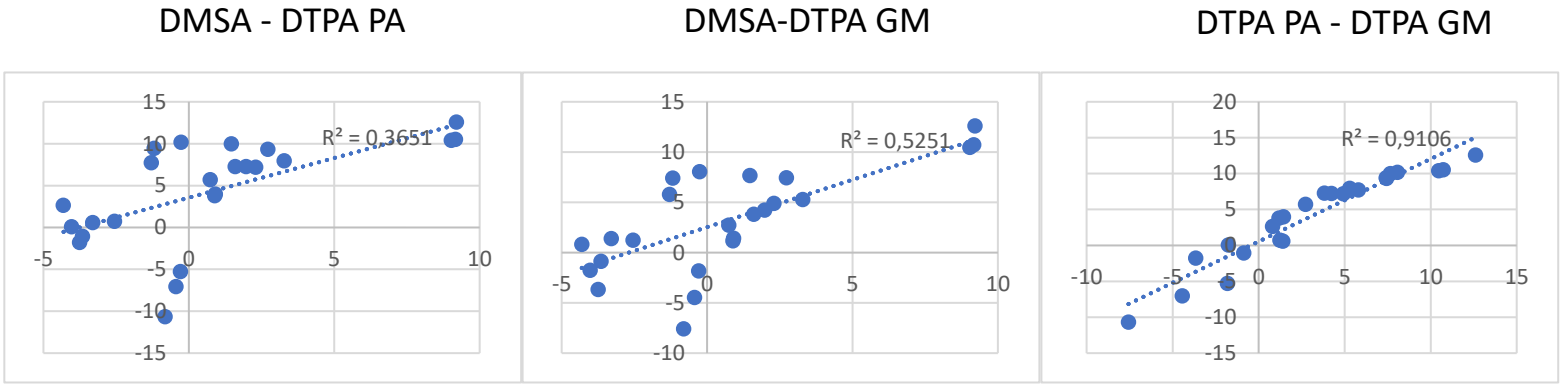

Figure 1

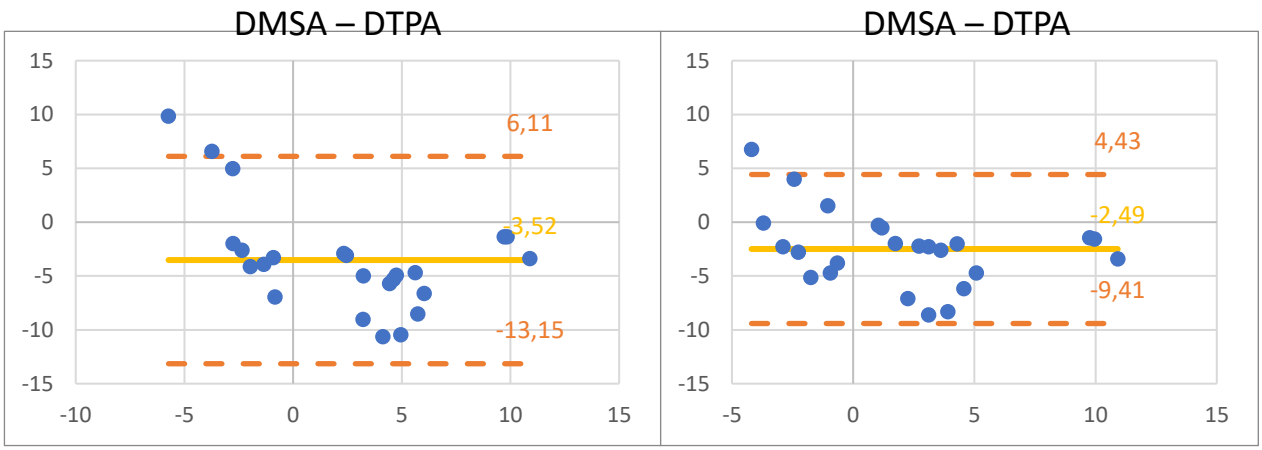

Figure 2

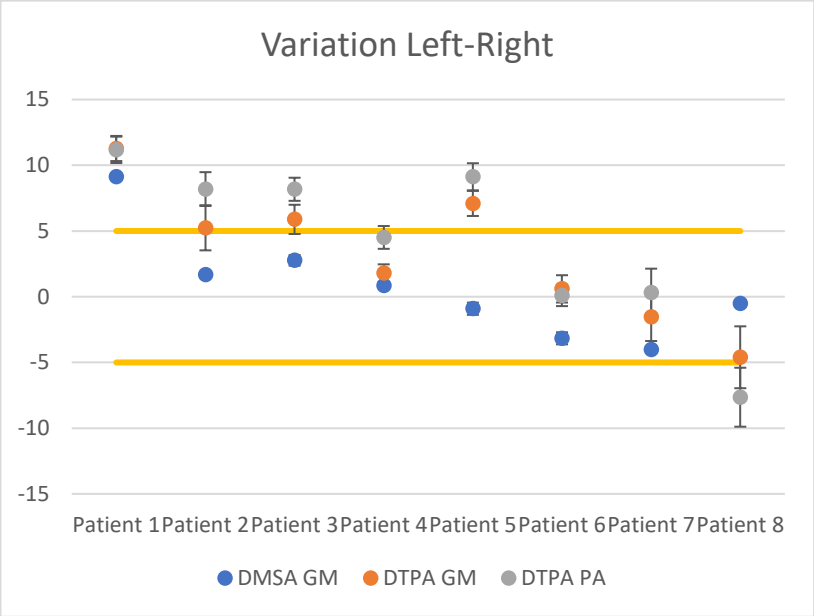
Variation Left-Right
15
10
5
0
-5
-10
-15
Patient 1
Patient 2
Patient 3
Patient 4
Patient 5
Patient 6
Patient 7
Patient 8
DMSA GM
DTPA GM
DTPA PA

Figure 3

LITERATURE REVIEW: FACTORS AFFECTING SENTINEL SCINTIGRAPHY

Mariana Kostura,[1]

[1] *Imelda Bonheiden*

Aims:

- Het onderzoeken van de factoren die de effectiviteit van sentinel scintigrafie beïnvloeden bij borstkankerpatiënten.
- Het beoordelen van hoe demografische, fysiologische en technische variabelen de detectie van sentinel lymfeklieren (SLN) beïnvloeden.
- Het evalueren van de impact van beeldvormingstechnieken en radiotracer doses op de nauwkeurigheid van SLN-detectie.

Methods:

- Literatuuronderzoek: Er werd een uitgebreide literatuurstudie uitgevoerd om verschillende studies te analyseren die zich richten op de factoren die de sentinel scintigrafie beïnvloeden.
- Analyse van verschillende variabelen: Factoren zoals body mass index (BMI), leeftijd, radiotracer doses, injectieplaatsen, en beeldvormingstechnieken (SPECT/CT vs. planar scintigraphy) werden onderzocht.
- Vergelijkende studies: Diverse onderzoeken werden vergeleken om de effectiviteit van verschillende injectiemethoden en beeldvormingstechnieken te evalueren, zoals SPECT/CT en planar scintigraphy, en hun effect op de SLN-detectie bij borstkanker.

Results:

- **BMI en Leeftijd**: Patiënten met een hogere BMI of ouder dan 60 jaar vertoonden een verhoogd risico op valse-negatieve resultaten, wat de effectiviteit van de SLN-detectie verminderde.
- **Doses van Radiotracers**: Verschillende studies gaven aan dat de gebruikte dosis van radiotracers invloed had op de detectiegevoeligheid. Een dosis van 5 tot 30 MBq werd vaak als voldoende beschouwd voor eenzelfde-dagoperatie.
- **Injectieplaats en Techniek**: Peritumorale injectie werd als de voorkeurstechniek beschouwd voor het detecteren van extra-axillaire SLN's, terwijl peri-areolaire injectie nuttig was voor niet-palpabele tumoren. Intradermale injectie bleek de meest consistente en nauwkeurige techniek voor axillaire SLN-mapping.
- **SPECT/CT vs. Planar Scintigrafie**: SPECT/CT had een hogere detectiegraad (91,1% vs. 86%) en identificeerde extra SLN's die planar scintigraphy miste. Het bood gedetailleerdere anatomische informatie en verbeterde de SLN-identificatie, vooral bij patiënten met obesitas.

Conclusions:

- **Demografische en fysiologische factoren** zoals BMI en leeftijd spelen een belangrijke rol in de effectiviteit van SLN-detectie. Patiënten met overgewicht en ouderen hebben een verhoogd risico op valse-negatieve resultaten.
- Er is geen uniforme consensus over de optimale dosis radiotracers, maar een dosis van 5 tot 30 MBq wordt vaak als voldoende beschouwd. Grotere injecties kunnen de lymfatische drainage verstoren.
- **Injectietechniek**: Peritumorale injectie blijft de voorkeursmethode voor SLN-detectie, vooral bij extra-axillaire knopen, terwijl intradermale injectie de meest consistente en nauwkeurige techniek voor axillaire SLN-mapping blijkt.

- **SPECT/CT**: Hoewel planar scintigraphy nuttig blijft, heeft SPECT/CT zich bewezen als een superieure beeldvormingstechniek voor SLN-detectie, vooral bij patiënten met een hoge BMI, afwijkende lymfatische drainage of bij gevallen die planar scintigraphy niet adequaat kan detecteren.
- Verdere **standaardisatie** van beeldvormingsprotocollen en radiotracer doseringen is noodzakelijk om de nauwkeurigheid van SLN-detectie verder te verbeteren en de uitkomsten voor patiënten te optimaliseren.

Poster Presentations

MEDICAL TRACK

BASELINE BONE MARROW SCINTIGRAPHY AS PREDICTIVE MARKER OF OVERALL SURVIVAL IN MCRPC PATIENTS TREATED WITH RADIUM-223 DICHLORIDE

Qaid Ahmed Shagera,[1], Olivier Gheysens,[2], Emilie Jonard,[3], Emmanuel Seront,[4], Bertrand Tombal,[5], Francois Jamar,[6]

[1] Cliniques Univérsitaires Saint-Luc, Uclouvain; Nuclear Medicine, [2] Clinique Universitaire Saint-Luc; Cliniques Universitaires Saint-Luc; Nuclear Medicine, [3] Cliniques Universitaires Saint-Luc; Cliniques Universitaires Saint-Luc; Nuclear Medicine, [4] Cliniques Univérsitaires Saint-Luc, Uclouvain; Department of Urology, [5] Cliniques Universitaires Saint-Luc; Cliniques Universitaires Saint-Luc; Department of Urology, [6] Cliniques Universitaires Saint-Luc (Ucl); Clinique Universitaire Saint-Luc; Nuclear Medicine

Aims
Prostate cancer is the most common malignancy among men globally. Radium-223 dichloride (Ra-223) has been incorporated into clinical guidelines as a therapeutic option for metastatic castration-resistant prostate cancer (mCRPC) with bone metastases. It is a bone-seeking calcium mimetic, high-energy alpha-emitter, selectively targeting bone metastases through enhanced bone turnover. Bone marrow scintigraphy (BMS), utilizing technetium-99m (Tc-99m)-labeled colloids, was introduced decades ago to assess bone marrow distribution and reserve. In oncology, it is hypothesized that the normal bone marrow distribution may be altered by the extent of skeletal metastatic infiltration, as well as other factors, such as prior radiotherapy or chemotherapy. To date, no studies have investigated the utility of BMS before Ra-223 treatment. We aimed to evaluate whether baseline BMS has a role in predicting overall survival (OS) in patients with mCRPC treated with Ra-223 dichloride.

Methods Among 82 patients treated with radium-223 (Ra-223) between 2014 and 2024, 28 underwent BMS on the same day as the first Ra-223 dose. Whole body planar imaging was conducted 30-60 minutes after injection of ~ 7.5 mCi of (Tc-99m)-labeled nanocolloids using a dual-head gamma camera. Visual image analysis was performed and defined as follows: a score of 0 indicated normal biodistribution, score 1 denoted mild expansion (discrete uptake outside regions of normal distribution), and score 2 represented moderate to extensive medullary expansion exemplified by uptake at the distal half of femoral and/or humeral diaphyses or more distally. Patients were subsequently dichotomized as those with scores of 0 or 1 versus those with 2. Clinical and laboratory factors were retrospectively analyzed. Data were reported as mean ± standard deviation (SD) for normally distributed variables and median (interquartile range, IQR) for non-normally distributed variables. A t-test comparing the mean was conducted to assess the relationship between BMS status and baseline hemoglobin levels. Cox proportional hazards regression and Kaplan-Meier survival analysis were performed to evaluate the relationship between BMS status and clinical variables and patient outcomes.

Results
A total of 130 doses of Ra-223 were administered, with a median of 6 cycles (IQR 3–6). Twenty-two patients had received at least one line of novel anti-androgen therapy, 14 at least one line of chemotherapy, and 15 at least two prior lines before Ra-223. Baseline BMS status was significantly associated with baseline hemoglobin levels: patients with normal BMS had a significantly higher mean hemoglobin (13.2 ± 1.2 g/dL) compared to those with bone marrow (BM) expansion (10.8 ± 1.7 g/dL, $p < 0.001$). The median number of Ra-223 cycles in patients with BM expansion was lower than in those with normal BMS (3 vs. 6, $p = 0.08$). Medullary expansion status was

significantly associated with the number of prior systemic therapies (p = 0.032) and salvage or metastatic targeted radiotherapy (p = 0.01). Median OS was 18 months, with 16 of 28 patients (57%) dead at the time of analysis. Among variables tested, BMS status, hemoglobin, number of prior systemic therapies, and number of Ra-223 cycles were significantly associated with OS (hazard ratios and p-values: 3.3, p = 0.02; 0.75, p = 0.042; 1.6, p = 0.019; 0.6, p = 0.002; respectively). Patients with normal BMS had a median OS of 33 months compared to 8 months in those with BM expansion (log-rank 5.5, p = 0.019).

Conclusions

To the best of our knowledge, this is the first study demonstrating the association between BMS status and baseline clinical factors in mCRPC patients treated with Ra-223. Patients with BM expansion received more prior treatments before Ra-223 and have worse outcomes compared to those with normal BMS. BMS status has the potential as a predictive imaging marker for OS in mCRPC patients treated with Ra-223.

AN EXPERIMENTAL PROTOCOL FOR THE CONSTRUCTION OF A HIGH-QUALITY MULTIMODAL BRAIN DATASET OF HEALTHY CONTROL SUBJECTS FOR A WIDE RANGE OF CLINICAL RESEARCH APPLICATIONS

Anaïs Gillet,[1], Dorian Palmeri,[2], Claire Bernard,[2], Glenn van der Lande,[3], Charlène Aubinet,[3], Paolo Cardone,[3], Pablo Núñez,[3], Naji Alnagger,[3], Jitka Annen,[3], Benedetta Cecconi,[3], Melanie Louras,[4], Michiel Meys,[3], Luaba Tshibanda,[5], Aurore Thibaut,[4], Nadia Withofs,[2], Roland Hustinx,[2], Arianna Sala,[3]

[1] University of Liège; Coma Science Group, Giga-Consciousness, Giga Institute; Coma Science Group, Giga-Consciousness, Giga Institute, University of Liège, [2] University Hospital of Liège; Division of Nuclear Medicine and Oncological Imaging, [3] University of Liège; Coma Science Group, Giga-Consciousness, Giga Institute, [4] University of Liège; Neurorecovery Lab, Giga-Consciousness, Giga Institute, [5] University Hospital of Liège; Department of Radiology

Aims

Advances in mechanical ventilation and medical care have improved the prognosis of brain-injured patients but have also increased the number of clinically complex cases with a disorder of consciousness (DoC). DoC after coma can affect individuals of all ages and include different conditions, including unresponsive wakefulness syndrome/vegetative state (UWS/VS) and minimally conscious state (MCS). UWS/VS patients are characterized by preserved arousal (eye opening and sleep-wake cycles) and presence of reflexive movements. However, purposeful movements and language abilities are absent. MCS patients present arousal (eye opening and sleep-wake cycles) and presence of reproducible non-reflex behaviors. While behavioral assessment remains the gold standard for the diagnosis of DoC, the use of advanced neuroimaging such as positron emission tomography (PET), magnetic resonance imaging (MRI) and electrophysiology techniques is recommended whenever possible, as they can reveal residual consciousness in behaviorally unresponsive patients, with strong implications for patients' prognosis and treatment.

An accurate analysis of patients' neuroimaging and electrophysiological assessments crucially relies on comparing them with appropriate normative data. While control databases serve as a critical reference in the diagnostic work-up, the field of DoC still faces a significant gap in this respect, due to the lack of multimodal normative datasets in healthy individuals. In line with this, we aim to develop a high-quality reference database through the acquisition of a multimodal neurophysiological database from a representative cohort of 62 healthy adults of all ages. Here, we present an experimental protocol that includes, among other elements, a dynamic fluorodeoxyglucose ([^{18}F]FDG) PET acquisition allowing for the non-invasive quantification of the cerebral metabolic rate of glucose (CMRglc), i.e. the gold standard for [^{18}F]FDG quantification. This kind of database was previously unavailable for the digital Siemens Biography Vision 600 PET/CT camera with 26cm axial field-of-view. The dynamic PET acquisition is carried out simultaneously with an electroencephalography (EEG) assessment. MRI data are also acquired, providing a comprehensive multimodal dataset.

Methods

This study recruits healthy participants, without history of neurological diseases, aged 18 to 79, ensuring that each age is represented; participants are stratified by age, with an equal number of males and females for each age decade. After a preliminary screening, including various questionnaires assessing different psychological and physiological functions, participants undergo final eligibility tests and additional behavioral assessments on the day of the acquisitions. To reduce the risk of drop-out, the acquisitions takes place in a single day at the CHU of Liège, including a 30-minute MRI scan with structural and functional sequences, a 12-minute eyes-closed EEG, and a 60-

minute dynamic [^{18}F]FDG-PET/EEG session. Pilot testing was undertaken to test the feasibility of a simultaneous dynamic [^{18}F]FDG-PET/EEG acquisition and to optimize the acquisition parameters.

[^{18}F]FDG-PET acquisitions are carried out with PET/CT Biograph Vision 600 scanner (Siemens Medical Solutions). The participants are positioned with both brain and common carotid arteries within the field of view, to allow for quantification based on an image-derived input function. The injected activity is 100 MBq, with a tolerance of ±10%, corresponding to an effective dose of 1.9 millisievert. A low-dose CT scan is acquired for attenuation correction, followed by a first 24-minute dynamic PET scan acquired simultaneously with an EEG recording, eyes open in darkness, followed by an additional low-dose CT scan and 36-minute dynamic PET acquisition without EEG (Figure 1). Throughout the acquisition, the subject's state of arousal is monitored via EEG, specifically by tracking the presence of eye blinks. If eye blinks persistently disappear, a brief auditory stimulation is delivered to encourage eye reopening. Dynamic images are reconstructed with iterative OSEM TOF reconstruction (4 iterations, 5 subsets, zoom 2, no filter, matrix 440x440). A static image of 10 minutes starting at 30 minutes post injection is also reconstructed, for consistency with the protocol used in clinical routine (OSEM TOF reconstruction with 12 iterations, 5 subsets, zoom 2, a gaussian post filter of 2 mm, matrix of 440x440).

After quality control, dynamic images are pre-processed using EMATA, an automatic toolbox for extracting and modelling arterial inputs for tracer kinetic analysis, and quantified using the CMRglc via Patlak's method. Static images are pre-processed and analyzed using SPM12, following a validated pipeline specific for DoC assessment (tinyurl.com/DOC-toolbox), including automated computation of standardized uptake value (SUV) and of statistical parametric maps of t-statistics of relative hypometabolism and relatively preserved metabolism.

Results

From the 17th of July 2023 to the 18th of March 2025, 52 participants were recruited for inclusion. However, two were excluded due to high scores on the Beck Depression Inventory (N=1, score>16) or the Beck's Anxiety Inventory (N=1, score>16), two others were excluded due to abnormal results in neuroimaging exams (N=1 MRI/PET, N=1 PET), and three more due to excessive movement during the PET scan. This resulted in a final dataset of 45 participants with usable PET images. Among them, six underwent a static PET scan instead of a dynamic one, either for unforeseen logistical circumstances (N=2) or because this type of acquisition was too cumbersome for older participants (N=4). Among included participants who had undergone the dynamic protocol (N=39), 21 were men and 18 were women, with ages ranging from 19 to 75 years (mean = 44.07, SD = 15.96), all with PET, MRI and EEG assessments within the normal range, based on visual inspection of PET SUV images by an expert rater (NW), of the FLAIR MRI sequence (by LT) and of the EEG trace (by MM, PN, BC). As of the 18th of March 2025, the database is 80.65% complete, and recruitment is expected to end in the summer of 2025.

Conclusion

By leveraging the power of a high-resolution digital PET/CT scanner and dynamic PET acquisitions, this study will generate a high-quality dataset of brain glucose metabolism in healthy volunteers of all ages, paving the way to robust instrumental assessment of neurological patients and discovery and validation of molecular biomarkers for clinical applications. The progress made in this multimodal control database so far demonstrates the feasibility of such a protocol. This reference dataset will provide high-quality multimodal data for the instrumental assessment of patients with a DoC and other neurological conditions, enabling applications in diagnosis, prognosis, and treatment evaluation

Figures

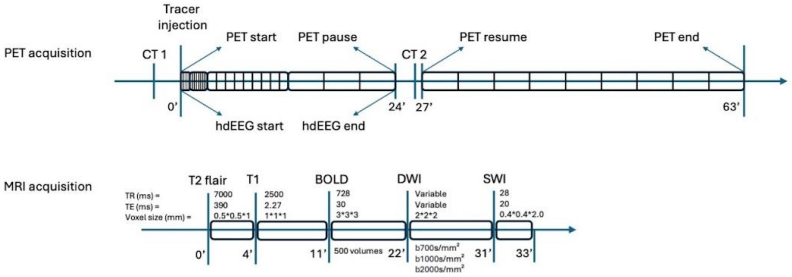

Figure 1. *Structure of the simultaneous PET/EEG acquisitions. Following a first low-dose CT scan, [18F]FDG tracer is injected. For the first 24 minutes, continuous PET imaging tracks the dynamic distribution of [^{18}F]FDG, while simultaneous EEG monitoring verify the subject's state of arousal, to minimize arousal-related variations of glucose consumption in the brain gray matter. This protocol allows us to obtain EEG data during the uptake phase of the tracer. The presence of eye blinks as monitored through/with EEG confirm wakefulness, and if absent for a prolonged period, a brief auditory stimulus is applied to re-establish alertness. At 12 minutes post-injection, an auditory stimulation is systematically administered. At the 24-minute mark, the EEG cap is carefully removed to minimize head displacement, followed by a second low-dose CT scan. PET imaging then resumes for an additional 36 minutes, completing the full 60-minute dynamic acquisition. The level of arousal is also assessed systematically based on self-report, before, during and after each stage (PET/EEG and last part of PET) using the Karolina Sleepiness Scale.*

RELATIONSHIP BETWEEN [18F]PSMA-1007 PET RESPONSE PARAMETERS AND BIOCHEMICAL RECURRENCE-FREE SURVIVAL IN HIGH-RISK PROSTATE CANCER PATIENTS RECEIVING NEOADJUVANT HORMONAL TREATMENT

Niloefar Ahmadi Bidakhvidi,[1], Alexander Giesen,[2], Gaëtan Devos,[2], Annouschka Laenen,[3], Marcella Baldewijns,[4], Michel Koole,[1], Christophe M. Deroose,[1], Wouter Everaerts,[5], Steven Joniau,[2], Karolien Goffin,[1]

[1] Uz/Ku Leuven; Nuclear Medicine and Molecular Imaging, Department of Imaging and Pathology, [2] Uz/Ku Leuven; Urology; Urogenital, Abdominal and Plastic Surgery, Department of Development and Regeneration, [3] Ku Leuven; Interuniversity Institute for Biostatistics and Statistical Bioinformatics, [4] Uz Leuven; Pathology, [5] Uz/Ku Leuven; Urology; Laboratory of Ion Channel Research, Department of Cellular and Molecular Medicine

Aims

To investigate the relationship between [18F]PSMA-1007 PET response parameters and biochemical recurrence-free survival (BCR-FS) in high-risk primary prostate cancer patients receiving neoadjuvant hormonal treatment.

Methods

This prospective randomized, double-blind, placebo-controlled phase II trial included 89 high-risk primary prostate cancer patients who received a pelvic [^{18}F]PSMA-1007 PET/MRI prior to and following neoadjuvant hormonal treatment. Patients were randomly assigned to neoadjuvant hormonal treatment with degarelix + apalutamide (n=45) or degarelix + matching placebo (n=44) for 3 months followed by radical prostatectomy and extended pelvic lymph node dissection. The following [^{18}F]PSMA-1007 parameters were determined on the pre- and posttreatment [^{18}F]PSMA-1007 PET: (i) semi-quantitative [^{18}F]PSMA-1007 PET parameters such as SUV_{max}, SUV_{mean}, PSMA-expressing volume and total lesion activity, and their absolute and relative differences; (ii) number of pelvic lymph node, distant and extraprostatic metastases determined on [^{18}F]PSMA-1007 PET; (iii) [^{18}F]PSMA-1007 PET-based response criteria (aPERCIST and RECIP 1.0); (iv) molecular imaging TNM-stage as determined by PROMISE version 2.

Results

Thirty-five percent of included patients developed BCR within a median follow-up time of 38 months. Multivariate regression analyses revealed that PSMA-expressing volume posttreatment, the number of distant metastases pretreatment and miN1+miN2 vs. miN0 pretreatment were significant predictors of BCR-FS with hazard ratios of 1.184 (95% CI 1.070-1.309, p=0.0010), 5.820 (95% CI 2.498-13.561, p<0.0001) and 4.024 (95% CI 1.740-9.307, p=0.0011), respectively.

Conclusions

Our results indicate that [^{18}F]PSMA-1007 PET can be a tool to monitor response to neoadjuvant hormonal treatment and that [^{18}F]PSMA-1007 PET can be used to aid in patient stratification for determining which patients would benefit from additional (neo)adjuvant treatment.

PERFORMANCE OF 18F-SYNVEST-1 VERSUS 18F-FDG IN COGNITIVE DECLINE: VISUAL READS AND QUANTIFICATION

Charles Carron,[1], Greet Vanderlinden,[1], Nikkita Khattar,[2], Louis Degryse,[1], Lennert Boeckxstaens,[3], Rik Vandenberghe,[4], Mathieu Vandenbulcke,[5], Koenraad Van Laere,[6]

[1] Ku Leuven; Uz Leuven; Nuclear Medicine, [2] Yale School of Medicine; Yale School of Medicine; Nuclear Medicine, [3] Uz Leuven; Uz Leuven; Ku Leuven, [4] Ku Leuven; Uz Leuven; Neurology, [5] Ku Leuven; Uz Leuven; Old-Age Psychiatry, [6] Uz/Ku Leuven; University Hospital Leuven; Department of Nuclear Medicine

Aims

^{18}F-FDG brain PET is routinely used in the clinical workup of patients with cognitive dysfunction. Synaptic vesicle glycoprotein 2A PET quantifies synaptic loss in various neurodegenerative disorders and is considered a purer marker of neurodegeneration as it is less influenced by acquisition context and neuroinflammation.

We investigated the diagnostic performance of ^{18}F-SynVesT-1 versus ^{18}F-FDG in a monocentric prospective study in patients referred to a tertiary memory clinic.

Methods

A pilot analysis was completed of 20 patients that underwent ^{18}F-FDG (30-45 minutes p.i.) and ^{18}F-SynVesT-1 (60-90 minutes p.i.) PET/MR within 3 months. Three nuclear medicine trained readers with variable experience (3-25 years) evaluated the randomized emission and Z-score images to assess the most likely diagnosis. The final diagnosis was obtained by clinical follow up. SUVR quantification (pons for ^{18}F-FDG and centrum semiovale for ^{18}F -SynVesT-1 as reference region) with PVC was used as comparator.

Results

After an average follow-up of 8 months, the final clinical diagnoses were 9 AD (1 with concomitant synucleinopathy), 1 FTD, 1 amnesia due to epilepsy and 9 without evidence of neurodegeneration (NoND). ^{18}F-FDG PET reads differentiated NoND from others with 82% accuracy (80-83%), with correspondence to the final diagnosis in 67% (65-70%). For ^{18}F-SynVesT-1 read accuracy was 72% (65-80%)), with corresponding final diagnosis in 53% (45-65%). Inter-observer agreement was better for ^{18}F-FDG than for ^{18}F-SynVesT-1 (Fleiss Kappa of 0.34 and 0.20). For the latter, the most experienced reader obtained most accurate results.

Comparing AD to NoND, frontal and parietal regions were described as most affected for both tracers albeit more pronounced for ^{18}F-FDG. Quantitative SUVR evaluation showed largest differences in the parietal, hippocampal and frontal cortices for ^{18}F-FDG (Cohen's d of 1.48; 1.32 and 1.26) compared to hippocampal, parietal and insular cortices for ^{18}F-SynVesT-1 (Cohen's d of 1.45; 1.41 and 1.38).

Conclusion

In this pilot analysis, ^{18}F-SynVesT-1 PET shows promise as a clinical tool for differentiating patients with cognitive decline of uncertain origin, demonstrating quantitively comparable deficits to ^{18}F-FDG PET. So far, reader experience determined initial read accuracy for ^{18}F-SynVesT-1. Fifty additional datasets are currently being evaluated with a broader final diagnostic spectrum, also allowing assessment of accumulating reader experience with ^{18}F-SynVesT-1 PET.

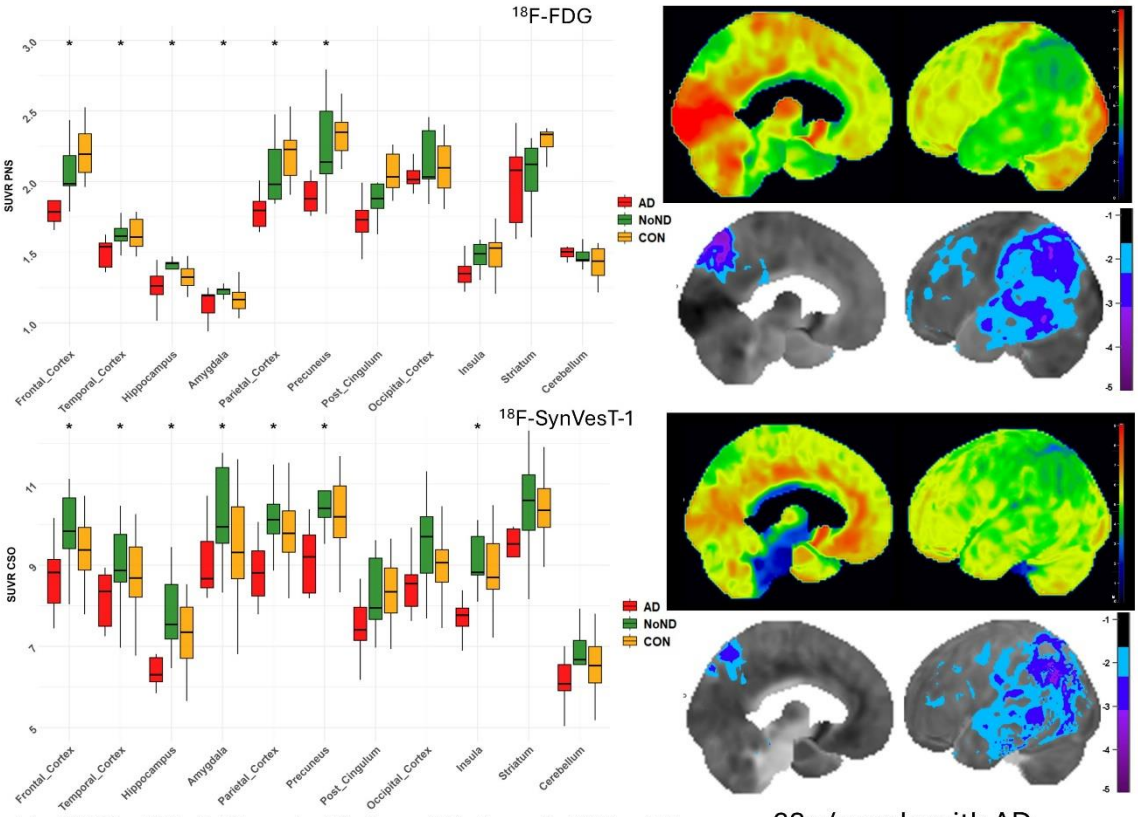

Box plots of ^{18}F-FDG and ^{18}F-SynVesT-1 comparing AD (n=9) versus ND (n=9) cases after PVC (* = p<0.05). Healthy controls: n=15 for ^{18}F-FDG and n=38 for ^{18}F-SynVesT-1.

63 y/o male with AD

BELGIAN DIAGNOSTIC REFERENCE LEVEL FOR PAEDIATRIC 18F-FDG PET/CT : FIRST VALUES FOR WHOLE BODY AND BRAIN SCANS

Théo Assoignon,[1], Michel Hesse,[2], Florian Dupont,[3], Francois Jamar,[4]

[1] Uclouvain, [2] Cliniques Universitaires Saint-Luc; Cliniques Universitaires Saint-Luc; Department of Nuclear Medicine, [3] Cliniques Universitaires Saint-Luc; Service de Médecine Nucléaire; Médecine Nucléaire, [4] Cliniques Universitaires Saint-Luc (Ucl); Clinique Universitaire Saint-Luc; Nuclear Medicine

Aims

PET/CT scanners allow the visualization of both the anatomy and the metabolism of the patient. As these technologies involve ionizing radiation, the ALARA principle must be followed, especially for children. One method to optimise the doses is the implementation of Diagnostic Reference Levels (DRLs). As of now, no DRLs are available in Belgium nor in Europe regarding PET/CT imaging of children. The purpose of this paper is to provide the first local DRLs for paediatric whole-body (WB) and brain ^{18}F-FDG PET/CT.

Methods

A retrospective study was carried out on all PET/CT scans performed in our centre on patients less than 18 years old between 2014 and 2018. Patients were grouped according to the ICRP135 classification: by body weight for whole-body examinations and by age for brain examinations.

Results

The calculated local DRLs are given in table 1 and 2 for paediatric WB and brain 18F-FDG PET/CT, respectively. Median weighted administered activities for whole-body PET are 4.4, 4.1 and 4.3 MBq/kg for the 15-<30 kg, 30-<50 kg and 50-<80 kg groups, respectively. For the brain PET, activies were 4.5 MBq/kg for the 1-<6 year group and 3.1 MBq/kg for the 6-<18 year group. The CTDIvol for the whole-body CT are 1.6, 2.2 and 3.1 mGy for the 15-<30 kg, 30-<50 kg and 50-<80 kg groups, respectively. The respective DLP's are 145.5, 230.9 and 342.6 mGy.cm. For the brain CT, the CTDIvol and DLP are 3.5 mGy and 75.8 mGy.cm for both 1-<6 year and 6-<18 year groups.

Conclusions

Based on measured dose metrics (DLP, CTDIvol and administered activities), we determined the first Belgian Diagnostic Reference Level values for paediatric whole-body and brain ^{18}F-FDG PET/CT examination, as the median of each metric, for both indications. It is recommended that the percentile 75 (P75) not be exceeded in clinical practice.

Of course, DRLs change over time and results need to be updated continuously, particularly when new technologies are implemented. This study should be complemented in the future by a larger multicentric study, to extend the values to the entire country.

Table 1: Median of the CT irradiation doses and radiopharmaceutical activities for paediatric WB exams. Values in parentheses are 95% Confidence Interval. Underlined values correspond to the P75.

Patient weight group (kg) (Nb. of patients)	Administered ^{18}F-FDG activity (MBq)	Weighted administered activity (MBq/kg)	$CTDI_{vol}$ (mGy)	DLP (mGy.cm)
15-<30 (24)	105.6 (92.72 - 115.96) **116.8**	4.4 (4.07 - 4.45) **4.5**	1.6 (1.5 - 2.1) **2.5**	145.5 (130.4 - 178.2) **211.9**
30-<50 (56)	163.0 (152.77 - 175.92) **189.4**	4.1 (3.95 - 4.18) **4.5**	2.2 (2.0 - 2.7) **3.1**	230.9 (204.5 – 268.0) **331.0**

50-<80 (65)	279.7 (251.41 - 291.56) **301.8**	4.3 (4.18 - 4.49) **4.7**	3.1 (2.8 - 3.5) **3.9**	342.6 (313.1 - 379.1) **464.8**

Table 2: Median of the CT irradiation doses and radiopharmaceutical activities for paediatric brain exams. Values in parentheses are 95% Confidence Interval. Underlined values correspond to the P75.

Patient age group (y) (Nb. of patients)	Administered ^{18}F-FDG activity (MBq)	Weighted administered activity (MBq/kg)	$CTDI_{vol}$ (mGy)	DLP (mGy.cm)
1-<6 (32)	79.4 (75.24 – 82.73) **83.6**	4.5 (4.24 - 4.84) **5.1**	3.5 (3.5 - 3.5) **3.5**	75.8 (75.8 - 75.8) **75.8**
6-<18 (66)	147.6 (134.92 – 156.12) **167.0**	3.1 (3.03 - 3.44) **4.0**	3.5 (3.5 - 3.5) **3.5**	75.8 (75.8 - 75.8) **76.2**

PROSTACT GLOBAL: A PHASE 3 STUDY OF LUTETIUM (LU177) ROSOPATAMAB TETRAXETAN PLUS STANDARD OF CARE VS STANDARD OF CARE ALONE IN PATIENTS WITH METASTATIC CASTRATION-RESISTANT PROSTATE CANCER

Karolien Goffin,[1], Scott Tagawa,[2], Neeraj Agarwal,[3], David Cade,[4], Oliver Sartor,[5]

[1] Uz Leuven; Uz Leuven; Nuclear Medicine, [2] Weill Cornell, [3] Huntsman Cancer Institute, University of Utah, [4] Telix Pharmaceuticals, [5] Mayo Clinic

Aims

Targeted radionuclide therapy (TRT) can localize treatment to specific tumor cells to reduce or eliminate damage to normal tissue for patients with prostate cancer (PC). Prostate-specific membrane antigen (PSMA) is an ideal therapeutic target as it is highly expressed by malignant PC cells. Compared to peptide-based, monoclonal antibody-based approaches have high binding specificity, rapid internalization, and long retention. Prior studies have demonstrated a favorable safety profile & efficacy of the radio-antibody drug conjugate (rADC) lutetium (Lu 177) rosopatamab tetraxetan (^{177}Lu-rosopatamab) using a fractionated 2 dose regimen. Thus, ^{177}Lu-rosopatamab is currently being investigated in a phase 3 study for treatment of patients with PSMA+ metastatic castration resistant PC (mCRPC) who have received prior treatment with one androgen receptor pathway inhibitor (ARPI).

Methods

This multinational, multicenter, prospective, randomized, open label phase 3 study has 2 parts: a dosimetry and safety lead-in (Part 1; n=30) & a randomized treatment expansion (Part 2; n=490). In Part 1, patients are divided into 3 groups (n=10 each) to receive 2 single intravenous injections of 76 mCi each, 14 days apart, of ^{177}Lu-rosopatamab with standard of care (SoC) combinations with one SoC drug (abiraterone, enzalutamide, or docetaxel) to characterize biodistribution & safety profiles of ^{177}Lu-rosopatamab + SoC combinations. SoC received is determined prior to treatment with ^{177}Lu-rosopatamab. In Part 2, patients will be enrolled 2:1 to receive SoC (determined pre-randomization) with or without 2 single injections of 76 mCi each of ^{177}Lu-rosopatamab, given 14 days apart.

Eligible patients must have PSMA-expressing mCRPC and have experienced disease progression on a minimum 12 weeks prior therapy on their 1st ARPI (abiraterone, apalutamide, darolutamide, or enzalutamide) in metastatic castration-sensitive PC, non-metastatic CRPC, or mCRPC settings. Patients may have received docetaxel in mCSPC setting provided last dose was ≥6 months prior to screening. Patients must have PSMA-positive disease on ^{68}Ga-PSMA-11 PET/CT imaging.

The primary endpoint is radiographic progression-free survival (rPFS). Key secondary endpoint is overall survival (OS). Additional secondary endpoints include 5-year OS, tumor objective response rate, time to symptomatic skeletal event, & health-related quality of life. An alpha control & 95% confidence intervals will be used; patients will be randomly assigned to receive ^{177}Lu-rosopatamab + SoC or SoC alone.

Results

This study is currently enrolling; no results are available at the time of abstract submission.

Conclusions

Combining the advantages of TRT along with proven patient selection capabilities of ^{68}Ga-PSMA-11 PET provides reasonable justification for further evaluation of ^{177}Lu-rosopatamab in a large-scale trial for the treatment of mCRPC.

This study is sponsored by Telix Pharmaceuticals. ClinicalTrials.gov ID: NCT06520345

COMPARISON OF HEAD MOVEMENTS IN BRAIN [18F]FDG-PET DYNAMIC AND STATIC ACQUISITIONS

Arthur Servais,[1], Anaïs Gillet,[2], Dorian Palmeri,[3], Claire Bernard,[4], Christophe Phillips,[5], Aurore Thibaut,[6], Roland Hustinx,[7], Nadia Withofs,[8], Arianna Sala,[6]

[1] Neurorecovery Lab, Giga-Consciousness, Giga Institute, University of Liège, [2] University of Liège; Coma Science Group, Giga-Consciousness, Giga Institute; Coma Science Group, Giga-Consciousness, Giga Institute, University of Liège, [3] Division of Nuclear Medicine and Oncological Imaging, University Hospital of Liège and Experimental Nuclear Medicine Lab, Giga Molecular & Computational Biology, University of Liège, [4] University of Liege; Chu Liege; Nuclear Medicine, [5] Neuroimaging Data Acquisition and Modeling Laboratory, Giga Crc Human Imaging, Giga Institute, University of Liège, Belgium, [6] Coma Science Group; Neurorecovery Lab, Giga-Consciousness, Giga Institute, University of Liège, [7] Centre Hospitalier Universitaire; Centre Hospitalier Universitaire de Liège; Service de Médecine Nucléaire, [8] Chu of Liege; Chu de Liège; Service de Médecine Nucléaire

Aims

The availability of PET/CT cameras with longer axial field-of-view (FOV) allows for non-invasive quantification of the cerebral metabolic rate of glucose (CMRglc), i.e. the gold standard in [^{18}F]FDG-PET imaging, by means of an image-derived input function. Still, this requires lengthy dynamic acquisitions of 60 minutes, which might be more difficult for patients to tolerate compared to standard static acquisitions that typically last 10 minutes. This might result in increased head movements and hence lower image quality compared to standard static images.

Our goal was to evaluate whether head movements during a 60-minute dynamic acquisition were comparable to those observed in a static protocol, and hence if the quality of the images obtained in a dynamic vs. static protocol was analogous. We performed this evaluation on healthy volunteers using data obtained from a prospective study (approved by the Institutional Ethics Committee, reference number B70720097332) whose aim was to establish a brain [^{18}F]FDG-PET/CT reference database of healthy controls for neurological applications.

Methods

We enrolled ten cognitively healthy volunteers. Informed consent was obtained from all participants. Five participants underwent dynamic acquisitions, split into two consecutive runs of 24 and 36 minutes, to allow for an initial simultaneous electroencephalographic acquisition as part of an experimental protocol (**Fig. 1**). Five participants underwent a single 10-minute static acquisition. In both settings, head movements were constrained by lateral inserts and front and chin stripes.

Acquisitions were performed on a PET/CT Siemens Vision 600 (FWHM=3.7mm, axial FOV=26cm). Injected activity of [^{18}F]FDG was 100+/-10%MBq.

Dynamic images were reconstructed using 3D-OSEM including TOF, 4 iterations and 5 subsets. Static images were reconstructed using 3D-OSEM including TOF, PSF, 12 iterations and 5 subsets with Gaussian filter whose FWHM=2mm. For both image series, attenuation and scatter correction is applied.

To estimate head movements, data were additionally reconstructed in 1-minute frames, without attenuation correction, to avoid possibly faulty reconstruction due to bias in attenuation correction (in case of important movements) (**Fig. 2**).

Movement estimation was performed with SPM12 *realign* function, in MATLAB R2020a, separately for each run of the dynamic protocol and for the static run. We used "register to the mean" two-step procedure, recommended for PET data, where a first realignment to a reference frame is followed by a second registration to the mean of all frames. As reference, we selected the last frame of run 1 and the first frame of run 2 and of the static run, respectively, because of their higher signal-to-noise ratio (SNR). The first three frames of run 1 were excluded because of different tracer distribution post-injection (limited to the carotids) and hence low SNR within the head.

For each participant, we computed six movement parameters within each run, i.e. translations along the x, y and z axes and rotations as pitch, roll and yaw.

We used Wilcoxon-Mann-Whitney test to assess whether head movements differed between dynamic and static acquisitions. We compared overall dynamic acquisitions against static acquisitions. The latter was further compared against frames corresponding to the post-injection timing of a static acquisition (but obtained during dynamic protocol), referenced below as "static_dyn". We also compared head movements between first and second run within dynamic acquisition.

To do so, we used summary indices of (i) head translations, by computing Euclidean distance of the sum vector, and of (ii) head rotations, by using an adaptation of Euclidean distance as in Wilke, 2011 (doi:10.1016/j.neuroimage.2011.10.043), referenced below as "Euclidean_rotations"

Results

Five participants underwent a dynamic acquisition (five males; median age, range: 33, 28-68 years) and five participants underwent a static acquisition (four males; median age, range: 71, 39-74 years).

(i) Regarding head translations during the overall dynamic acquisition, median Euclidean distance was 0.4mm, with an interquartile range (IQR) of 0.36mm (run 1: 0.4mm [IQR: 0.33mm]; run 2: 0.39mm [IQR: 0.44mm]. During the static acquisition, median Euclidean distance was of 0.38mm with an IQR of 0.22mm; In static_dyn, median Euclidean distance was of 0.36mm with an IQR of 0.32mm. Using Wilcoxon-Mann-Whitney test, we found no significant differences in head translation movements between static images and the overall dynamic protocol (U = 5437, p = 0.192). Likewise, translation movements between static and static_dyn images were not significantly different (U = 923, p = 0.470). No difference was found between run 1 and run 2 of the dynamic protocol (U = 8658, p = 0.885).

(ii) Using Wilcoxon-Mann-Whitney test, we found no significant differences in head rotation movements between static images and the overall dynamic protocol (U = 5912, p = 0.632). Likewise, rotation movements between static and static_dyn images were not significantly different (U = 939, p = 0.553). No difference was found between run 1 and run 2 of the dynamic protocol (U = 8693, p = 0.928). Median value and interquartile range of Euclidean_rotations are not reported, since this index provides an absolute displacement estimate for points at a specific distance from the rotation centre but not for the whole volume.

Conclusions

Our preliminary results showed that there was no significant difference in terms of head movements between dynamic and static acquisitions. These findings, referring to a sample of ten subjects, will be replicated in a larger cohort (analyses are planned in 57 participants). It should also be noted that our findings are valid for our specific

acquisition protocol (**Fig. 1**) but might not necessarily apply to standard "continuous" dynamic acquisitions. Likewise, generalizability of our findings to different clinical populations is to be tested; in some clinical conditions, where patients' compliance could be altered (e.g. dementia, disorder of consciousness), a more advanced apparatus for head immobilization might be required to achieve results similar to those reported in the current study.

Figures

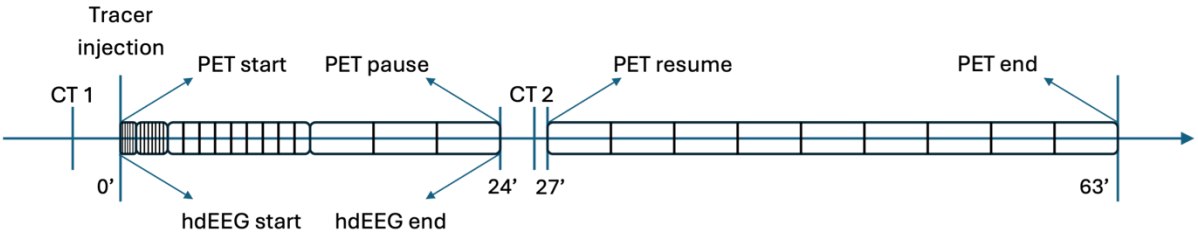

Fig 1: **Overview of the acquisition protocol:** the protocol consisted of two runs: a first run, with electroencephalography, which started at T0 from tracer injection and lasted 24 minutes, followed by a +/- 3 minutes break to remove the electroencephalography cap, and a second run that lasted 36 minutes. At the beginning of each run, a low-dose CT was performed for attenuation correction. The rectangles represent the frame duration, i.e., for run 1: six frames of ten seconds, eight frames of 15 seconds, nine frames of 60 seconds, three frames of 240 seconds; for run 2: nine frames of 240 seconds. Abbreviations: hdEEG, high-density electroencephalography.

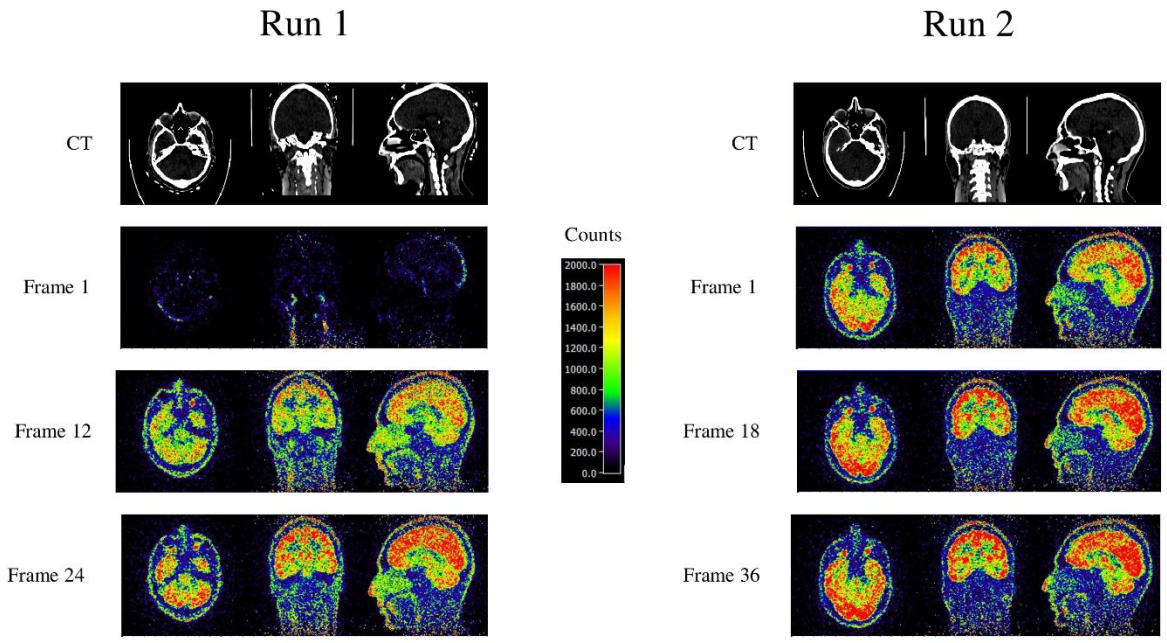

Fig 2: Representative frames from a dynamic acquisition. The figure shows the non-attenuation corrected frames from a test subject, following the three standard planes of reference (from left to right: transversal, coronal and sagittal), at various moments of the acquisition. Notice the white dots around the skull in the CT volume from run 1, representing the high-density electroencephalography cap, that was removed in run 2. The brain renders were created using Vinci64 v 5.06.

FEASIBILITY OF PERFORMING CFR PROTOCOLS USING NOVEL SPECT-CT STARGUIDE

Alban Gjukaj,[1], Younes Abadi,[2], Nicolas Dumarey,[2], Sophie Boeckmans,[3], Katia Dibartolomeo,[2], Patrick Flamen,[2], Carlos Artigas,[2]

[1] Ulb; Hôpital Universitaire de Bruxelles; Nuclear Medicine, [2] Hôpital Universitaire de Bruxelles, [3] Hub, Hôpital Erasme-Ulb

Aims

Ischemia and myocardial infarction with non-obstructive coronary artery disease (INOCA/MINOCA) are frequent coronary syndromes that are often underdiagnosed due to the absence of significant epicardial stenosis on coronary angiography. These conditions are primarily associated with coronary microvascular disease (CMD), justifying the use of advanced functional biomarkers such as coronary flow reserve (CFR) to detect patients with CMD[1, 2]. CFR assesses the ability of coronary blood flow to increase in response to vasodilatory stress. It reflects the entire coronary vascular status. Cardiac PET is the gold standard for CFR assessment, using radiotracers such as [^{13}N]-ammonia, [^{15}O]-water, and Rubidium-82. These PET-tracers enable quantitative evaluation of myocardial blood flow. In PET studies, a CFR value < 2 is generally accepted as abnormal, indicating possible microvascular dysfunction (including microvascular spasm, epicardial coronary spasm, coronary microvascular dysfunction, and myocardial bridging) and serves as an independent predictor of major cardiovascular events. [3] However, cardiac PET is expensive and not widely available. The development of cardiac-dedicated CZT cameras has enabled the evaluation of myocardial blood flow (MBF) and CFR using SPECT (Single Photon Emission Computed Tomography), with CFR values comparable to those obtained with PET. [4, 5, 6, 7, 8]

The more recently arrived high-resolution 3D ring SPECT-CT CZT gamma cameras, such as the Starguide (GE Healthcare) have urged the need for the validation of CFR measurement in these next generation systems.

Until now, only two cases have been published performing quantitative myocardial blood flow measurements using a StarGuide CZT gammacamera. [9, 10].

The Starguide camera has a more closed and/or a deeper gantry in contrast to the conventional CZT SPECT camera systems, making access to the patient during dynamic acquisitions less evident. Since a dynamic myocardial bloodflow SPECT acquisition needs a pharmacological stress and a perfusion tracer administration with the patient already positioned in the camera gantry, the feasibility of dynamic MIBI SPECT acquisition with this camera for CFR measurement in rest and after pharmacological needed to be addressed.

Case Report

An eighty-two-year-old man complaining of dyspnea and exertional fatigue was referred for coronary artery disease screening. The patient had several cardiovascular risk factors: type 2 diabetes, hypertension, dyslipidemia, and obesity.

Rest ECG showed no significant abnormalities. Echocardiography demonstrated a dilated left ventricle, a left ventricular ejection fraction (LVEF) of 35%, septal and apical wall motion abnormalities, and hypokinesia in the inferior wall.

A 2-day myocardial perfusion SPECT was performed at rest and after regadenoson stress with 555 MBq 99mTc-MIBI. A dynamic SPECT acquisition was performed for MBF and CFR calculation.

For the rest exam, the dynamic bloodflow SPECT was initiated immediately after a bolus injection of 99mTc-MIBI with a saline flush. For the stress exam, the patient received an intravenous injection of 400 µg regadenoson over 10 seconds with saline flushing, followed by the 99mTc-MIBI administration 10 seconds later. The total time of the dynamic acquisitions was 9 minutes. After a five-minute rest period, a routine gated myocardial perfusion SPECT-

CT acquisition was performed. The results of the gated myocardial perfusion imaging revealed a reversible perfusion defect in the apical and inferior wall, compatible with regadenoson-induced ischemia. CFR values were calculated with the use of the 4DM software (Invia). The CFR values obtained from dynamic 3D SPECT were 1.37 in the left anterior descending coronary artery territory, 2.01 in the left circumflex coronary artery territory, and 1.81 in the right coronary artery territory, resulting in a global coronary flow reserve of 1.63. These values are low compared to current standards used for PET.

Conclusions

The StarGuide™ CZT SPECT-CT system promises major advancements in nuclear cardiology, with 3D dynamic SPECT acquisitions allowing CFR calculations. With this case we demonstrated the feasibility of cardiac dynamic SPECT on this next generation camera system. Its future integration into a standardized study protocol with reproducible measurements and the determination of the limit values of normal and decreased CFR will require validation with prospective trials.

References

1. AlShaikh S, Rohm CL, Sutton NR, Burgess SN, Alasnag M. INOCA: Ischemia in non-obstructive coronary arteries. Am Heart J Plus. 2024 Apr 16;42:100391. doi: 10.1016/j.ahjo.2024.100391. PMID: 38680648; PMCID: PMC11043816.

2. Bailly M, Thibault F, Courtehoux M, Metrard G, Angoulvant D, Ribeiro MJ. Myocardial flow reserve measurement during CZT-SPECT perfusion imaging for coronary artery disease screening: correlation with clinical findings and invasive coronary angiography—The CFR-OR Study. Front Med (Lausanne). 2021 Jun 4;8:691893. doi: 10.3389/fmed.2021.691893. PMID: 34150820; PMCID: PMC8212953.

3. Herzog BA, Husmann L, Valenta I, Gaemperli O, Siegrist PT, Tay FM, et al. Long-term prognostic value of ^13N-ammonia myocardial perfusion positron emission tomography added value of coronary flow reserve. J Am Coll Cardiol. 2009;54:150-6

4. Valenta I, Dilsizian V, Quercioli A, Ruddy TD, Schindler TH. Quantitative PET/CT measures of myocardial flow reserve and atherosclerosis for cardiac risk assessment and predicting adverse patient outcomes. Curr Cardiol Rep. 2013;15:344. doi: 10.1007/s11886-012-0344-0.

5. Nkoulou R, Fuchs TA, Pazhenkottil AP, Kuest SM, Ghadri JR, Stehli J, et al. Absolute myocardial blood flow and flow reserve assessed by gated SPECT with cadmium-zinc-telluride detectors using ^99mTc-tetrofosmin: head-to-head comparison with ^13N-Ammonia PET. J Nucl Med. 2016;57:1887–92. doi: 10.2967/jnumed.115.165498.

6. Agostini D, Roule V, Nganoa C, Roth N, Baavour R, Parienti JJ, et al. First validation of myocardial flow reserve assessed by dynamic ^99mTc-sestamibi CZT-SPECT camera: head-to-head comparison with ^15O-water PET and fractional flow reserve in patients with suspected coronary artery disease—The WATERDAY study. Eur J Nucl Med Mol Imaging. 2018;45:1079–90. doi: 10.1007/s00259-018-3958-7.

7. Acampa W, Zampella E, Assante R, Genova A, De Simini G, Mannarino T, et al. Quantification of myocardial perfusion reserve by CZT-SPECT: a head-to-head comparison with ^82Rubidium PET imaging. J Nucl Cardiol. 2020. doi: 10.1007/s12350-020-02129-w. [Epub ahead of print].

8. Giubbini R, Bertoli M, Durmo R, Bonacina M, Peli A, Faggiano I, et al. Comparison between ^13N-NH3 PET and ^99mTc-tetrofosmin CZT SPECT in the evaluation of absolute myocardial blood flow and flow reserve. J Nucl Cardiol. 2019. doi:
10.1007/s12350-019-01939-x. [Epub ahead of print].

9. Bailly M, Callaud A, Metrard G. Dynamic cardiac SPECT with flow measurement using 3D-ring CZT: when SPECT is inspired by PET. Eur J Nucl Med Mol Imaging. 2023 May;50(6):1837–9. doi: 10.1007/s00259-022-06106-y. PMID: 36622405.

10. Carsuzaa T, Thibault F, Bailly M. Gated tomographic radionuclide angiography using 3D-ring CZT StarGuide SPECT/CT head-to-head comparison with a cardiac-dedicated CZT camera: first clinical use and validation. Clin Nucl Med. 2022 Jul 1;47(7):e515–e517. doi:
10.1097/RLU.0000000000004153. Epub 2022 Mar 31. PMID: 35353756.

Physics and Engineering Track

EVALUATING MOTION PATTERNS FOR UPRIGHT PATIENT POSITIONING IN THE WALK-THROUGH PET: A CLINICAL STUDY

Rabia Aziz,[1], Nadia Withofs,[2], Florence Muller,[1], Jens Maebe,[1], Boris Vervenne,[1], Christian Vanhove,[1], Stefaan Vandenberghe,[1]

[1] Ghent University; Department of Electronics and Information Systems, [2] Chu of Liege; Department of Medical Physics

Aims:

The Walk-Through PET (WT-PET) scanner introduces a flat-panel design, inspired by airport security scanners, where patients stand upright between two flat detector panels [1]. These panels, measuring 106 cm in height, 71 cm in width, and spaced 50 cm apart, cover the head and torso to the upper thigh as represented by *Figure 1a*. Using monolithic LYSO detectors with depth-of-interaction (DOI) technology, the predicted spatial resolution is around 2 mm. The DOI allows closer panel positioning, reducing the number of detectors and cutting costs by 50% compared to cylindrical PET scanners with similar sensitivity and axial field-of-view (AFOV) [2,3]. Beyond cost efficiency, the WT-PET scanner streamlines patient positioning and throughput. Patients can easily step into the scanner and position themselves using an ergonomically designed headrest and hand supports for stability. The high sensitivity enables a 30-second scan time, reducing total throughput time per patient to 2–4 minutes. However, upright positioning in the WT-PET scanner may lead to increased patient motion compared to the supine position in cylindrical PET scanners. Studies using infrared-based tracking of healthy volunteers suggest that upright imaging is more prone to motion artifacts [4], but patient motion in clinical settings remains unexplored. The 30-second scan time of WT-PET also presents an opportunity to incorporate breath-hold techniques to minimize breathing motion. Nevertheless, its feasibility, tolerability, and effectiveness in patients require further evaluation. This study aims to characterize patient motion in a clinical setting, focusing on rigid head, shoulders, chest, and abdomen motion during both normal breathing and breath-hold conditions.

Methods:

The study included thirty (n = 30) patients who were scheduled for a PET/CT scan at CHU Liège on October 2, 2024. All participants provided written informed consent following ethical guidelines (CHU-Liège Ethics Committee reference 2022-229; EudraCT B7072022000034). For each participant, five passive infrared markers were placed at key anatomical points: on the head, shoulders, chest, and abdomen. Additionally, adjustable headrests and hand supports were utilized inside the WT-PET mockup to ensure optimal patient comfort and to minimize involuntary motion. These ergonomic adjustments were tailored to each patient's height and overall comfort. Two video recordings of 30 seconds were made for each participant—one during normal breathing and another during breath-holding. The videos were captured using the Orbbec Femto Mega depth camera, which operates at 30 frames per second. However, not all patients were able to maintain a full 30-second breath-hold due to differences in respiratory capacity. Breath-hold duration and timing were defined as follows:

(1) Full breath-hold participants held their breath for the entire 30-second scan duration (t = 0s to 30s).

(2) Moderate breath-hold participants maintained breath-hold for 20–29 seconds, but the exact start time could vary.

(3) Short breath-hold participants held their breath for less than 20 seconds during the scan. For all participants, the scan duration remained fixed at 30 seconds, with breath-hold initiation assumed to be at t = 0s, unless otherwise specified.

From each recorded video, the RGB, infrared and depth channels were extracted. The infrared channel was processed using a series of image processing techniques including thresholding to isolate the markers from the background, blob detection to track the markers in each frame, depth extraction to determine the spatial position of the markers, and transformation of the 2D data into 3D coordinates (*Figure 2b)*. Two metrics were used to quantify the degree of motion across the 30 participants: Average Absolute Deviation (AAD) and Euclidean Distance (ED), reported as mean ± standard deviation.

Both metrics were calculated for each marker under both normal breathing and breath-holding conditions. In addition to measuring motion, the study explored potential relationships between motion and age.

Results:
The results indicated a prominent reduction in external breathing motion during breath-holding, particularly in the chest and abdomen regions. For the abdomen, the mean Euclidean Distance (ED) significantly decreased from 2.31 ± 1.32 mm to 1.76 ± 0.81 mm ($p < 0.05$), and the chest showed a similar reduction with ED decreasing from 2.08 ± 1.66 mm during normal breathing to 1.68 ± 0.99 mm during breath-holding.

In contrast, shoulder motion exhibited a slight reduction during breath-holding, but this change was not statistically significant. The mean ED for the right shoulder decreased from 1.26 ± 1.12 mm during normal breathing to 1.16 ± 0.69 mm during breath-holding, and the left shoulder showed a similar trend. Head motion, on the other hand, remained largely unaffected between normal breathing and breath-holding conditions. The mean ED for the head was 1.51 ± 2.32 mm during normal breathing and 1.58 ± 1.89 mm during breath-holding. These results are summarized in *Table 1.*

Furthermore, the scatter plots represented in *Figure 2* compare motion during normal breathing (y-axis) and breath-hold (x-axis) across different anatomical regions: head, left shoulder, right shoulder, chest, and abdomen. Each point represents a single patient, categorized into full breath-hold (30s, blue circles), moderate breath-hold (20–30s, green squares), and short breath-hold (10–20s, red triangles). The dashed diagonal line (y = x) serves as a reference—points above this line indicate reduced motion during breath-hold. Most points for the abdomen and chest lie above the diagonal, indicating motion is consistently reduced during breath-hold. Patients in the full and moderate breath-hold groups (blue and green) show greater and more consistent motion reduction compared to those in the short breath-hold group (red triangles). In contrast to the chest and abdomen, motion reduction is less consistent for the head and shoulders. Some patients still exhibit reduced motion (points above the diagonal), but several points remain near or below the line, indicating that breath-holding does not always stabilize these regions. This could be due to postural adjustments, muscle fatigue, or compensatory movements during breath-hold. Optimizing patient positioning, especially for the head and shoulders, could further reduce motion.

Statistical analysis identified a significant correlation between patient age and head motion during normal breathing. Older patients exhibited slightly more head motion, although the effect size was small.

Conclusions:
This study demonstrates that ergonomic adjustments, such as headrests and hand supports, help minimize rigid motion in the WT-PET mock-up scanner. Previous work has shown that these adjustments can achieve motion reduction comparable to standard cylindrical PET scanners [4]. While residual motion remained present, particularly in the head and shoulders, breath-holding prominently reduced motion in the chest and abdomen regions by up to 20% and 24%, respectively. However, the 30-second breath-hold duration was unfeasible for over 50% of participants, indicating that shorter breath-hold durations may be more appropriate in clinical practice.

Keywords: Motion tracking, Walk-through PET, Infrared-based localization, Upright imaging, Breath-holding

References

[1] S. Vandenberghe *et al.*, "Walk-through flat panel total-body PET: a patient-centered design for high throughput imaging at lower cost using DOI-capable high-resolution monolithic detectors," *Eur J Nucl Med Mol Imaging*, vol. 50, no. 12, pp. 3558–3571, Oct. 2023, doi: 10.1007/s00259-023-06341-x.

[2] Maya Abi Akl, O. Bouhali, Y. Toufique, J. Karp, and S. Vandenberghe, "Monte Carlo sensitivity study of a long axial FOV PET scanner with patient adaptive rings," in *2019 IEEE Nuclear Science Symposium and Medical Imaging Conference (NSS/MIC)*, 2019, pp. 1–3. doi: 10.1109/NSS/MIC42101.2019.9059834.

[3] M. Dadgar, J. Maebe, M. Abi Akl, B. Vervenne, and S. Vandenberghe, "A simulation study of the system characteristics for a long axial FOV PET design based on monolithic BGO flat panels compared with a pixelated LSO cylindrical design," *EJNMMI Phys*, vol. 10, no. 1, p. 75, 2023, doi: 10.1186/s40658-023-00593-0.

[4] R. Aziz, J. Maebe, F. M. Muller, Y. D'Asseler, and S. Vandenberghe, "Quantitative analysis of patient motion in walk-through PET scanner and standard axial field of view pet scanner using infrared-based tracking," *EJNMMI Phys*, vol. 11, no. 1, p. 99, Nov. 2024, doi: 10.1186/s40658-024-00704-5.

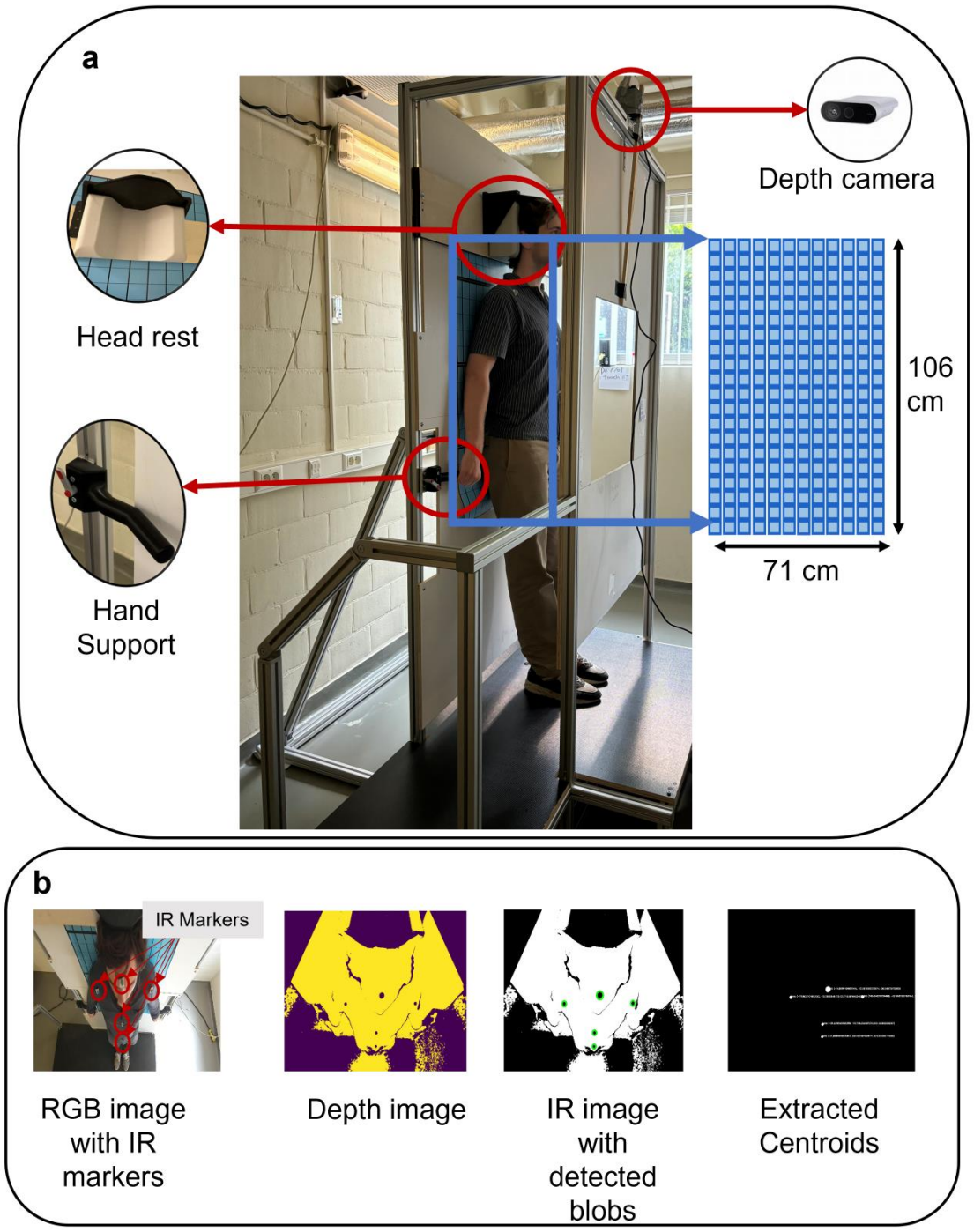

Figure 13 (a) Walk-Through PET mock-up scanner featuring patient positioning with an integrated headrest, hand supports, and a depth camera. (b) Image processing pipeline illustrating extracted RGB image, depth image, infrared (IR) image with detected blobs, and extracted centroids.

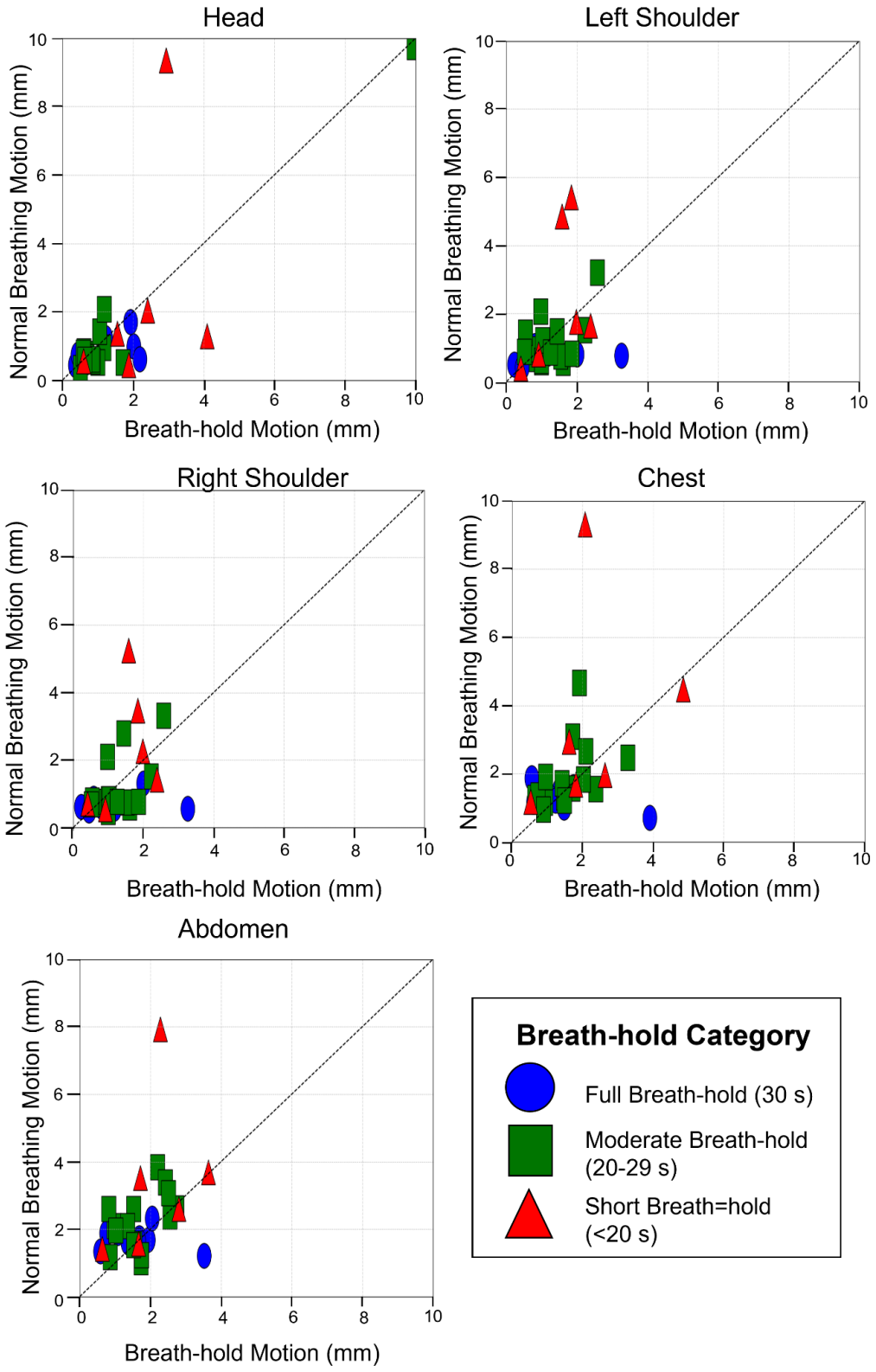
Head
Left Shoulder
Right Shoulder
Chest
Abdomen
Normal Breathing Motion (mm)
Breath-hold Motion (mm)
0
2
4
6
8
10
Breath-hold Category
Full Breath-hold (30 s)
Moderate Breath-hold (20-29 s)
Short Breath=hold (<20 s)

Figure 14 Comparison of motion during normal breathing and breath-hold across all anatomical markers for each patient. Each scatter plot represents motion measurements for the head, left shoulder, right shoulder, chest and abdomen during normal breathing (y-axis) and breath-hold (x-axis). Each point represents a single patient, categorized into three breath-hold duration categories: full breath-hold (30s, blue circles), moderate breath-hold (20-29s, green squares), and short breath-hold (10-20s, red triangles). The dashed diagonal line (y=x) serves as a reference: points above this line indicate reduced motion during breath-hold compared to normal breathing.

*Table 3 Average Euclidean Distance (ED) and Standard Deviation (SD) across all participants for all marker positions during normal breathing and breath-hold conditions. Average distance is reported as mean ± SD expressed in mm, and significant differences are indicated by * ($p<0.05$).*

Breathing Condition	Head ED ± SD (mm)	Left Shoulder ED ± SD (mm)	Right Shoulder ED ± SD (mm)	Chest ED ± SD (mm)	Abdomen ED ± SD (mm)
Normal Breathing	1.51 ± 2.32	1.31 ± 1.19	1.26 ± 1.12	2.08 ± 1.66	2.31 ± 1.32
Breath-hold	1.58 ± 1.89	1.28 ± 0.74	1.16 ± 0.69	1.68 ± 0.99	1.76 ± 0.81 *

GENERALIZING DEEP LEARNING DENOISING FOR NOVEL PET RADIOTRACERS TO IMPROVE IMAGE QUALITY

Simon Dekeyser,[1], Evelien Van Genugten,[2], Tomas Brants,[1], Sezgin Ustmert,[3], Alex Maes,[4], Erik Aarntzen,[5], Stefaan Vandenberghe,[6], Maarten Larmuseau,[7], Roland Hustinx,[8]

[1] Nuclivision, [2] Radboud Umc, [3] Az Groeninge, [4] Az Groeninge; Az Groeninge; Nuclear Medicine, [5] Radboud University Nijmegen Medical Centre; Radboud University Nijmegen Medical Centre; Nuclear Medicine, [6] Universiteit Gent; Medisip Elis-Ibitech, [7] Ugent, [8] Centre Hospitalier Universitaire; Centre Hospitalier Universitaire de Liège; Service de Médecine Nucléaire

Aims
While [18F]FDG has long been the reliable workhorse of nuclear imaging, there is an increasing need for more sensitive and specific radiotracers to improve diagnosis and treatment planning. An interesting avenue is the use of Zr-89 labelled monoclonal antibodies, as the longer half-time of Zr-89 matches the slow pharmacokinetics of these antibodies. However, such less established tracers typically suffer from high costs and varying image quality, impeding broader adaptation. The use of deep-learning based denoising algorithms could help remediate these challenges, but generally require many scans for training, which are not commonly available for new tracers. This study aimed to evaluate the generalizability of deep learning-based denoising algorithms, trained on conventional, short-lived radiotracers, to less common tracer types and radioisotopes that were not encountered during model training.

Methods
First, a deep-learning model with a Unet architecture was trained on matching low-count and standard-count PET scans from two Belgian hospitals (AZ Groeninge and CHU Liège). During training, only matching pairs of two commonly available tracers were seen by the model, [68Ga]Ga-PSMA and [18F]FDG . The model was then validated on 89Zr-labelled durvalumab PET scans from Radboud UMC and a phantom filled with 89Zr that was acquired at different acquisition times, ranging from 60s to 1200s, by downsampling the list-mode data. Image quality was assessed using the coefficient of variation in relevant regions and through visual inspection comparing the original scans with their enhanced counterparts.

Results
The deep learning model could significantly improve image quality of the [89Zr]Zr-DFO-durvalumab scans, strongly reducing the variation in SUV for several organs across different patients. The algorithm also removed some unrealistically high SUVmax that were observed in certain tissues and overall resulted in a visually more appealing scan. Additional validation on the IEC NEMA phantom, confirmed that the matching enhanced images had a lower variance in SUV, both in the spheres and in the background. At the same time, the recovery coefficient for the SUVmean and SUVmax improved in all spheres, for the 10 and 20 minute scans.

Conclusions
In silico denoising by our deep-learning-based model seems to at least partially generalize to 89Zr-labelled radiotracers as shown by this study on [89Zr]Zr-DFO-durvalumab. Strategies for post-hoc enhancement of PET-scans may help to harmonize scan quality, which facilitates pooled analyses of multi-center studies using less commonly used radiotracers.

DETERMINATION OF MOLECULAR IMAGING VOLUME USING PET/CT: VALIDATION USING 3D PRINTING TECHNOLOGY

Matthijs Sevenois,[1], Wies Deckers,[1], Georg Schramm,[2], Michel Koole,[2], Wies Claeys,[2], Karolien Goffin,[1], Christophe Deroose,[1], Kristof Baete,[1]

[1] Uz Leuven; Uz Leuven; Nuclear Medicine, [2] Kuleuven; Uz Leuven; Department of Imaging and Pathology

Aims

Recent studies have shown the potential of dosimetry as a predictive biomarker in nuclear medicine therapy [1], [2], [3]. However, the dosimetry workflow used to obtain the absorbed dose to tissue depends on many elements [4], each requiring optimization and for which uncertainties must be taken into account [5]. A particular challenge in the study of lesion dosimetry, is the quantification of activity and the determination of the volume of these small structures [6], for which over the years several methods have been proposed [2], [3], [7], [8], [9].

Meanwhile, 3D printing technology has become a powerful technique that is capable of making complex shapes with a high precision. This method has recently been used to assess partial volume effects associated with the uptake quantification in different organs in emission tomography [10], [11]. Hence, 3D printing could be used as a "validation tool" for the different methodologies in determining the volume of lesion-like structures based on PET data. Our aim was to assess the bias and the accuracy of different available segmentation techniques on the volume quantification of 3D printed lesions of several sizes by means of PET as a potential input for dosimetry calculations.

Methods

First, a large lesion (volume 43.25 mL) was derived from a PET image (Biograph Vision.X, Siemens Healthineers, Erlangen, Germany) using MIM v7.3.4 (Cleveland, OH) from a metastatic prostate cancer patient eligible for ^{177}Lu-PRLT, after which it was loaded into 3-matic v17.0 software (Materialise, Leuven, Belgium), where it was smoothed and subsequently downscaled to 4.64 mL and 0.97 mL filling volume. Printing was facilitated by additive manufacturing (Bambu Lab X1C, Shenzhen, China) using ABS filament. Measured volumes were determined by water filling.

Three lesions were mounted in a NEMA IEC Body phantom and combined with the 3 largest spheres (37mm, 28mm and 22mm diameter). The background and hot spheres were filled with [^{18}F]FDG encompassing two ratios: 1:10 and 1:5 with a hot sphere activity concentration of about 22 kBq/mL at the start of PET acquisition. Three minute acquisitions (matrix size 440, pixel size 1.65 mm) and reconstructions (PSF+TOF 4i5s, 7mm gauss post-smooth) were performed on the Biograph Vision.X PET/CT (Siemens, Erlangen, Germany). Next, the effective molecular imaging volume was determined using various tools: the PET Edge®, PET Edge®+ tool (MIM), 42% threshold of the signal above background and an iterative boundary-reproducing threshold (BRT) [9]. For the latter, the average FWHM of the reconstructed spatial resolution was also determined using Python (pynemaiqpet, v0.5.4), as it is a required input into the algorithm.

Results

After leak testing, the 3D printed lesions were inserted in the NEMA phantom (Figure 1).

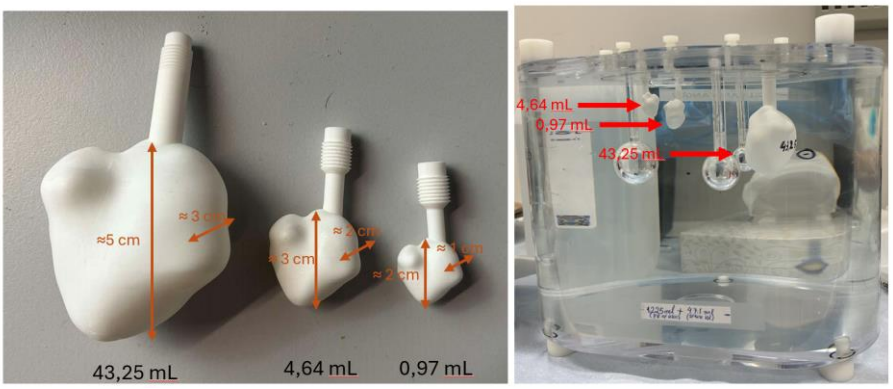

Figure 15: 3D printed lesions submerged in a NEMA phantom

Next, the FWHM of the spheres was determined to be about 8mm FWHM on average (Figure 2), as this is necessary for the BRT method.

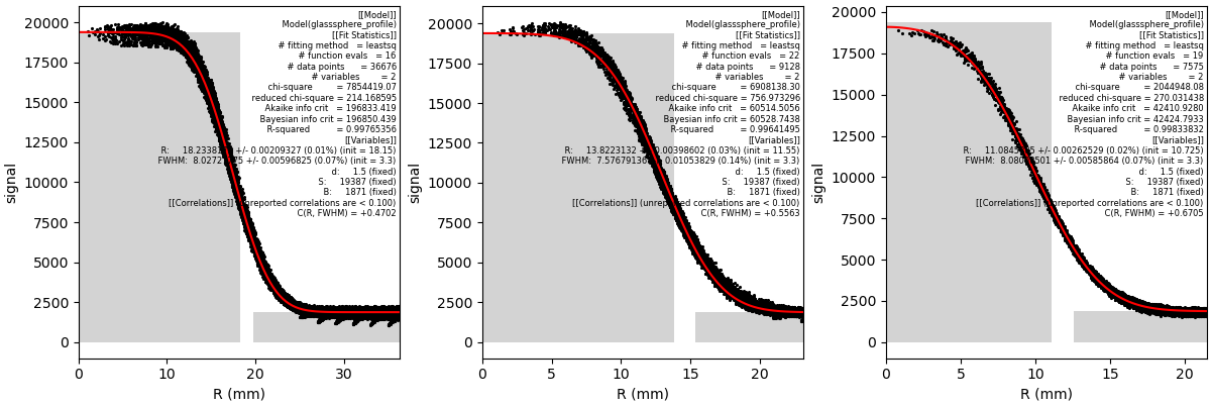

Figure 16: determination of the FWHM (mm) for the three largest spheres (37mm, 28 mm and 22 mm diameter).

Relative bias from the measured volume, when using the PET Edge®+ tool from MIM are < 9% for the largest lesion (Figure 3.a), while < 16% for the medium size lesion (Figure 3.b) and outperforms PET Edge® which exhibits relative errors up to 30 and 20% respectively. The (B-S).0.42+B method is a good predictor for larger volumes, but underestimations are noted for smaller structures. The BRT method provides estimates < 3% (Figure 3.a), <13% (Figure 3.b) with consistent bias. An example of the iteration of the thresholding is illustrated in Figure 4.

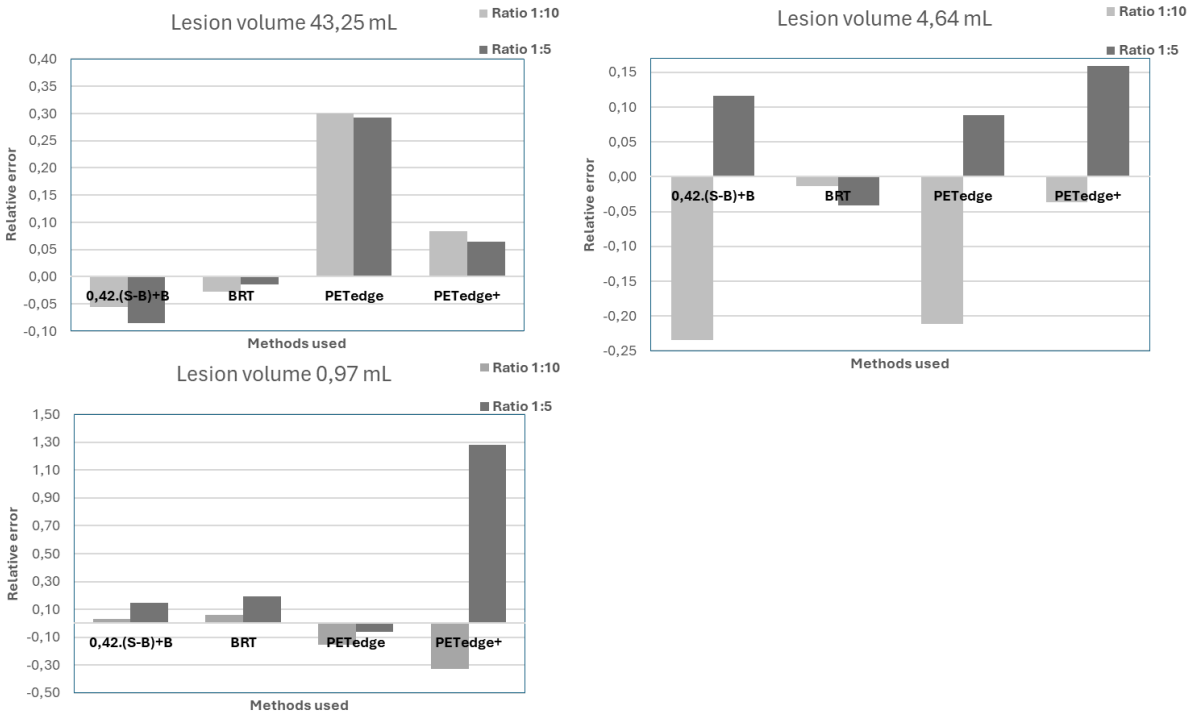

Figure 17: determined relative error for each segmentation technique for 43.25 ml (a), 4.64 ml (b) and 0.97 mL (c) volume.

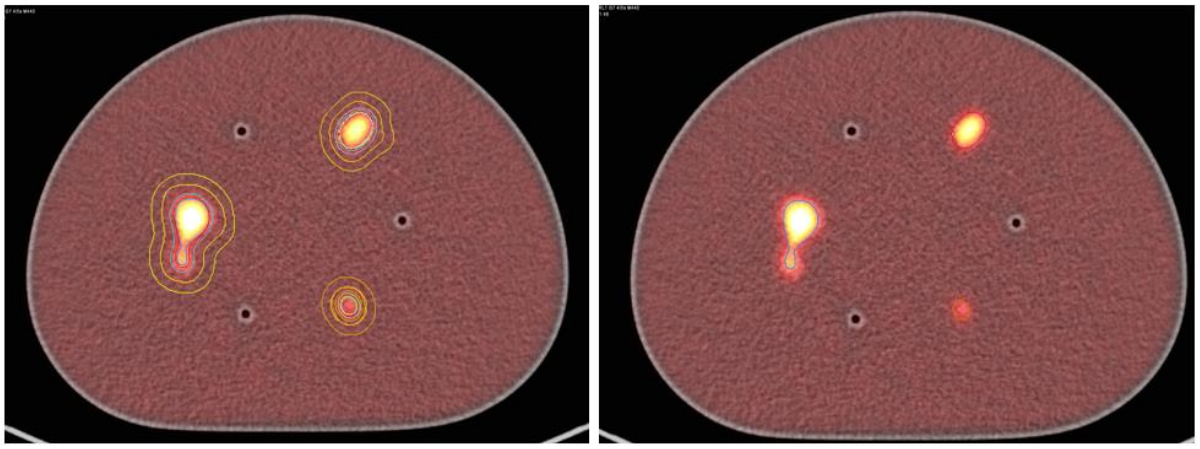

Figure 18: illustration of the BRT method on PET/CT (left), in which the threshold contouring based on the PET image is iterated until convergence, in other words the final volume (right). The CT is added for better visualization.

Discussion

The 42% threshold of the signal above background shows smaller relative errors on larger structures and a larger dependency on hot spheres to background concentration. PET Edge®+ outperforms PET Edge® accompanied by the advantage that PET Edge®+ can potentially reduce the variations induced from different operators as the volume-of-interest is created with less manual interventions. Notably as well, is the overestimation of the lesion

volume of 43.25 mL with 30% using PET Edge®, whereas PET Edge®+ reduces till <8% overestimation. The BRT method shows consistent bias for 43.25 and 4.64 mL and has a maximum overestimation of 20% for the 1 mL lesion and moreover a reduced spread when comparing for 1:10 and 1:5 contrast settings. This method however required pre-knowledge of the FWHM (mm) of the reconstructed spatial resolution.

Conclusion

Several image processing methodologies were validated on their ability to determine the lesion volume based on PET data. 3D printing technology was crucial in this analysis. The results indicate that it is important, even for larger lesions, to assess the potential bias on the lesion volume determination. The current results indicate that the BRT shows overall good results and would be the preferred methodology for the task of molecular imaging volume determination. Given the current results, PET/CT (for example for prostate cancer using [^{18}F]PSMA) could potentially be used for the determination of molecular imaging tumour volume and as input for dosimetry calculations.

Future work should include testing of the influence of different reconstruction parameters and heterogeneity on the robustness of the BRT method.

[1] K. Hebert *et al.*, "Absorbed dose–response relationship in patients with gastroenteropancreatic neuroendocrine tumors treated with [177Lu] Lu-DOTATATE: one step closer to personalized medicine," *Journal of Nuclear Medicine*, vol. 65, no. 6, pp. 923–930, 2024.

[2] C. F. Warfvinge *et al.*, "Relationship between absorbed dose and response in neuroendocrine tumors treated with [177Lu] Lu-DOTATATE," *Journal of Nuclear Medicine*, vol. 65, no. 7, pp. 1070–1075, 2024.

[3] M. Mileva *et al.*, "Prediction of 177Lu-DOTATATE PRRT outcome using multimodality imaging in patients with gastroenteropancreatic neuroendocrine tumors: results from a prospective phase II LUMEN study," *Journal of Nuclear Medicine*, vol. 65, no. 2, pp. 236–244, 2024.

[4] M. Bardiès and J. I. Gear, "Scientific developments in imaging and dosimetry for molecular radiotherapy," *Clin Oncol*, vol. 33, no. 2, pp. 117–124, 2021.

[5] J. I. Gear *et al.*, "EANM practical guidance on uncertainty analysis for molecular radiotherapy absorbed dose calculations," *Eur J Nucl Med Mol Imaging*, vol. 45, pp. 2456–2474, 2018.

[6] L. Carnegie-Peake, J. Taprogge, I. Murray, G. D. Flux, and J. Gear, "Quantification and dosimetry of small volumes including associated uncertainty estimation," *EJNMMI Phys*, vol. 9, no. 1, p. 86, 2022.

[7] J. Gustafsson, A. Sundlöv, and K. Sjögreen Gleisner, "SPECT image segmentation for estimation of tumour volume and activity concentration in 177Lu-DOTATATE radionuclide therapy," *EJNMMI Res*, vol. 7, no. 1, Dec. 2017, doi: 10.1186/s13550-017-0262-7.

[8] F. Hofheinz, S. Dittrich, C. Pötzsch, and J. Van Den Hoff, "Effects of cold sphere walls in PET phantom measurements on the volume reproducing threshold," *Phys Med Biol*, vol. 55, no. 4, pp. 1099–1113, 2010, doi: 10.1088/0031-9155/55/4/013.

[9] W. Jentzen, "An improved iterative thresholding method to delineate PET volumes using the delineation-averaged signal instead of the enclosed maximum signal," *J Nucl Med Technol*, vol. 43, no. 1, pp. 28–35, 2015, doi: 10.2967/jnmt.114.152678.

[10] J. I. Gear *et al.*, "Abdo-Man: a 3D-printed anthropomorphic phantom for validating quantitative SIRT," *EJNMMI Phys*, vol. 3, no. 1, Dec. 2016, doi: 10.1186/s40658-016-0151-6.

[11] J. Tran-Gia, S. Schlögl, and M. Lassmann, "Design and fabrication of kidney phantoms for internal radiation dosimetry using 3D printing technology," *Journal of Nuclear Medicine*, vol. 57, no. 12, pp. 1998–2005, 2016.